DOUBLE CHOOZ NEUTRINO DETECTOR: NEUTRON DETECTION SYSTEMATIC ERRORS AND DETECTOR SEASONAL STABILITY

by

PI-JUNG CHANG

B. Sc., Soochow University, Taiwan, 2002
M. Sc., National Taiwan Normal University, Taiwan, 2005

———————————

AN ABSTRACT OF A DISSERTATION

submitted in partial fulfillment of the
requirements for the degree

DOCTOR OF PHILOSOPHY

Department of Physics
College of Arts and Sciences

KANSAS STATE UNIVERSITY
Manhattan, Kansas
2013

Abstract

In March 2012, the Double Chooz reactor neutrino experiment published its most precise result so far: $\sin^2 2\theta_{13} = 0.109 \pm 0.030(\text{stat.}) \pm 0.025(\text{syst.})$. The statistical significance is 99.8% away from the no-oscillation hypothesis. The systematic uncertainties from background and detection efficiency are smaller than the first publication of the Double Chooz experiment. The neutron detection efficiency, one of the biggest contributions in detection systematic uncertainties, is a primary topic of this dissertation. The neutron detection efficiency is the product of three factors: the Gd-capture fraction, the efficiency of time difference between prompt and delayed signals, and the efficiency of energy containment. ^{252}Cf is used to determine the three factors in this study. The neutron detection efficiency from the ^{252}Cf result is confirmed by the electron antineutrino data and Monte Carlo simulations. The systematic uncertainty from the neutron detection efficiency is 0.91% used in the $\sin^2 2\theta_{13}$ analysis. The seasonal variation in detector performance and the seasonal variations of the muon intensity are described in detail as well. The detector stability is confirmed by observation of two phenomena: 1) the $\overline{\nu_e}$ rate, which is seen to be uncorrelated with the liquid scintillator temperature, and 2) the daily muon rate, which has the expected correspondence with the effective atmospheric temperature. The correlation between the muon rate and effective atmospheric temperature is further analyzed in this thesis to determine the ratio of kaon to pion in the local atmosphere. An upper limit on instability of the neutron detection efficiency is established in the final chapter. The systematic error, 0.13%, from the relative instability is the deviation of the calibration runs. This thesis concludes with the potential systematic errors of neutron detection efficiency and estimation of how these potential systematic errors affect the result of $\sin^2 2\theta_{13}$.

DOUBLE CHOOZ NEUTRINO DETECTOR: NEUTRON DETECTION SYSTEMATIC ERRORS AND DETECTOR SEASONAL STABILITY

by

PI-JUNG CHANG

B. Sc., Soochow University, Taiwan, 2002
M. Sc., National Taiwan Normal University, Taiwan, 2005

A DISSERTATION

submitted in partial fulfillment of the
requirements for the degree

DOCTOR OF PHILOSOPHY

Department of Physics
College of Arts and Sciences

KANSAS STATE UNIVERSITY
Manhattan, Kansas
2013

Approved by:

Major Professor
Dr. Glenn Horton-Smith

Copyright

Pi-Jung Chang

2013

Abstract

In March 2012, the Double Chooz reactor neutrino experiment published its most precise result so far: $\sin^2 2\theta_{13} = 0.109 \pm 0.030(\text{stat.}) \pm 0.025(\text{syst.})$. The statistical significance is 99.8% away from the no-oscillation hypothesis. The systematic uncertainties from background and detection efficiency are smaller than the first publication of the Double Chooz experiment. The neutron detection efficiency, one of the biggest contributions in detection systematic uncertainties, is a primary topic of this dissertation. The neutron detection efficiency is the product of three factors: the Gd-capture fraction, the efficiency of time difference between prompt and delayed signals, and the efficiency of energy containment. ^{252}Cf is used to determine the three factors in this study. The neutron detection efficiency from the ^{252}Cf result is confirmed by the electron antineutrino data and Monte Carlo simulations. The systematic uncertainty from the neutron detection efficiency is 0.91% used in the $\sin^2 2\theta_{13}$ analysis. The seasonal variation in detector performance and the seasonal variations of the muon intensity are described in detail as well. The detector stability is confirmed by observation of two phenomena: 1) the $\overline{\nu_e}$ rate, which is seen to be uncorrelated with the liquid scintillator temperature, and 2) the daily muon rate, which has the expected correspondence with the effective atmospheric temperature. The correlation between the muon rate and effective atmospheric temperature is further analyzed in this thesis to determine the ratio of kaon to pion in the local atmosphere. An upper limit on instability of the neutron detection efficiency is established in the final chapter. The systematic error, 0.13%, from the relative instability is the deviation of the calibration runs. This thesis concludes with the potential systematic errors of neutron detection efficiency and estimation of how these potential systematic errors affect the result of $\sin^2 2\theta_{13}$.

Table of Contents

List of Figures

List of Tables

Acknowledgments

First, I would like to express my indebtedness to my major professor, Glenn Horton-Smith, for helping, for guiding, and for tolerating me throughout six years. His suggestions always inspire me to solve the research problem in the right direction.

Second, I would like to thank Dr. Zelimir Djurcic from Argonne National Laboratory for his professional suggestions and guidance of the neutron detection efficiency study and also thank Dr. Lindley Winslow for her assistance in the Double Chooz physical environment monitoring system and the beginning of my analysis.

Third, I would like to thank Hao-Ming Chen, P.E., LEED AP. Without his support and encouragement, I cannot survive in the United States and even finish my thesis on time. Finally, I am grateful to my coworker, Deepak Shrestha and the colleagues in the Double Chooz collaboration who helped me when I was in France and the United States.

Pi-Jung Chang
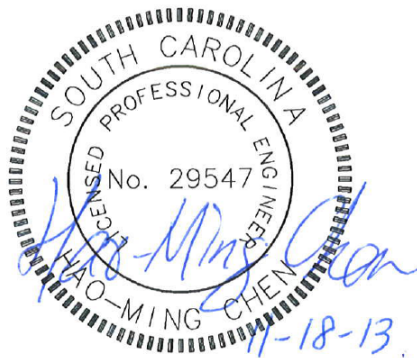
Chapter 1

Introduction

The neutrino was postulated as a new spin, 1/2, neutral particle by Wolfgang Pauli in 1930 in order to explain the continuous energy distribution of beta decay. The neutrino was observed directly after 26 years. In 1953-59, the electron antineutrinos from the nuclear reactor were discovered with the inverse beta decays (IBD) by Reines and Cowan.[6,7] Abundant righthanded antineutrinos from ^{60}Co nuclear beta decays explained the parity violation observed by Wu et al. in 1957.[8] Shortly afterward, another experiment proved the distinction between the electron neutrino and electron antineutrino with a liquid CCl$_4$ detector containing 4000 liters.[9] Neutrino astrophysics has become a new field by this pioneering study.[10] The neutrino helicity measurement can be done by analyzing the polarization of the photon from the following orbital electron capture, and this experiment was first set up by Goldhaber et al.[11] Then, the muon neutrinos were demonstrated by the pion decays.[12] On the other hand, the existence of gauge bosons, W and Z, was predicted in the Glashow-Weinberg-Salam Model (GWS). The Z-boson birth is associated with weak neutral currents (NC) in nature. The discovery was done by the bubble chamber experiment, which was searching for purely leptonic NC events from $\overline{\nu_\mu}$ + e $\rightarrow$ $\overline{\nu_\mu}$ + e. The weak gauge bosons were finally discovered in 1983 with the UA1 and UA2 experiments. The third generation neutrino, tau neutrino, was expected under the Standard Model. The DONUT collaboration provided direct evidence to prove the existence of the tau neutrino in 2000 by distinguishing its interaction from the interactions of electron neutrino and muon neutrino.[13]

Many experiments proved that the neutrino was electrically neutral from charge conservation, and even massless or many orders lighter than other charged leptons in the weak interaction reaction. The Standard Electroweak Model assumes that neutrino mass is equal to zero and obeys the conservation helicity (The neutrinos from beta decays are all left-handed.). However, neutrino mass does not need to be zero in any physical requirement.[14] An assumption that neutrino is not massless has became a main issue in many fundamental physical fields.[14] The first assumption of neutrino with mass was from B. Pontecorvo in 1957.[15] In Pontecorvo's hypothesis, there are two Majorana neutrinos, which are superpositions in the weak interaction field. Therefore, the neutrino oscillation model is brought forth naturally from his assumption. In 1969, Gribov and Pontecorvo showed that the solar neutrinos, ν_e, could transfer to another flavor, ν_μ, in the propagation from the Sun to the Earth.[16] In their hypothesis, there are only four neutrino states: two of the neutrino states are left-handed, and the other neutrino states are right-handed, and only the left-handed neutrinos have the mass.[16] In the beginning, people thought that the neutrino mixing only consisted of two Dirac neutrinos. Soon, Majorana neutrino was included into the mixing scheme. The oscillation model mixing Dirac and Majorana neutrinos was brought forth by Barger, Langacker, and Leveille.[17] The See-Saw Mechanism provided another direction that there could be a very heavy neutrino to conserve the lepton number. The heavy neutrino could be another explanation that why so few antimatters exist in our universe.

Recently, there are many kinds of neutrino experiments: for instance, the neutrino mixing angles, the Δm_{ij}^2, and the double beta decay. In Maki-Nakagawa-Sakata (MNS) matrix[18], we can use at least three eigenstates to explain the present neutrino flavors (only use three states in this thesis), and the three sectors can be observed by atmospheric, reactor, accelerator, and solar neutrino experiments. Recently, the precision measurements of the non-vanishing angle, θ_{13}, investigation has became a major study. According to the CHOOZ reactor experiment, we only have known that the mixing angle value of $\sin^2 2\theta_{13}$ is smaller than 0.1.[19] The value of $\sin^2 2\theta_{13}$ also constrains the phase δ term of the T or CP violation in the

MNS matrix. If the $\sin^2 2\theta_{13}$ is smaller than 0.01, the next generation experiments of the CP-violation effect will be very hard to measure the CP-violation phase. In order to determine $\sin^2 2\theta_{13}$, Minakata et al. have proposed that $\overline{\nu_e}$ survival experiments from the nuclear reactors could be the most efficient way to measure $\sin^2 2\theta_{13}$.[20] IBD is the main reaction to detect the neutrino oscillation research in the reactor neutrino experiment because of the larger cross-section and the signature of time delayed signals. The flux of $\overline{\nu_e}$ is inverse with the cross section of the IBD as a function of $\overline{\nu_e}$ energy. The comparison among the energy spectrum, the cross section, and the flux of neutrinos is shown in Figure 1.1. The $\overline{\nu_e}$ interaction spectrum and the cross section of IBD are inverse with the $\overline{\nu_e}$ flux in the Double Chooz reactor simulations. Since the neutrino energy from the reactors is only in the few-
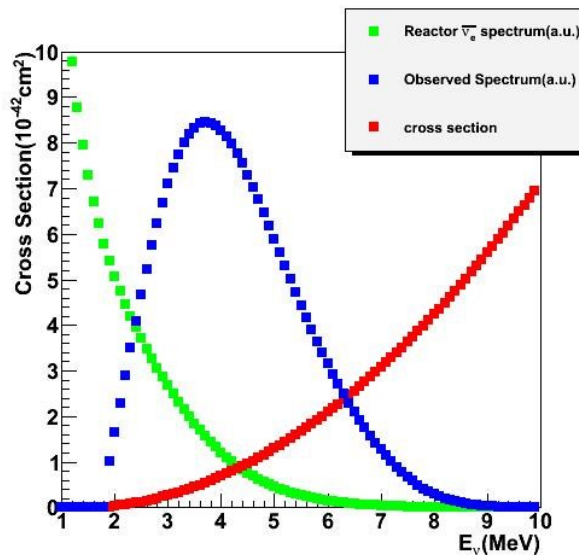
Figure 1.1: $\overline{\nu_e}$ interaction, cross section of inverse beta decay, and $\overline{\nu_e}$ flux spectrum from the Double Chooz reactor simulation. This plot is calculated from DCRxtrTools, one of the Double Chooz software packages.[21]

MeV range, the experiment is limited to the observation of $\overline{\nu_e}$ survival.[22] The low energy of $\overline{\nu_e}$ prevents the production of muons or taus by $\overline{\nu_e}$ oscillating into $\overline{\nu_\mu}$ and $\overline{\nu_\tau}$.[22] Therefore, the background is relatively smaller than the neutrino source from the accelerator. In the past decade, multi-detector neutrino experiments have achieved the sensitivity of $\overline{\nu_e}$ survival down to $\sin^2 2\theta_{13} = 0.01$.[23–25] The near detector offsets the systematic errors from the far

detector to reach a better sensitivity, and the $\overline{\nu_e}$ survival experiment does not depend on any CP-violation phase and the matter effect.[26]

Several new reactor neutrino experiments have been built and have taken data since 2011. The Double Chooz experiment, one of these new experiments, has taken data since April of 2011. The far detector is located at the original Chooz experiment site, and the near detector at 400 meters away from the two reactors is in the process of installation. The first Double Chooz publication using only the data of far detector in 101 data-taking days was published in Physical Review Letters in 2012.[1] This result is the first announcement of the precise measurement of the mixing angle θ_{13} from the new reactor neutrino experiments. The unique rate-shape analysis of the $\overline{\nu_e}$ prompt spectrum has considered the shape information in the Double Chooz $\sin^2 2\theta_{13}$ result, and a precise model of the two-reactor thermal power has reduced the biggest systematic uncertainty of the experiment.[1] The second publication used data collected in 334 data-taking days, and the uncertainties of detection efficiency and background have been reduced.[1] The newest result achieves statistical significance 99.8% away from the no-oscillation hypothesis due to the correction of the systematic uncertainties and the statistical error.

This thesis is divided into four sections. Chapter 2 to 4 describe the basic principle of the neutrino mixing theory and the structure of Double Chooz experiment. Chapter 5 represents the neutron detection efficiency. Chapter 6 discusses the seasonal stability of the detector. Finally, Chapter 7 shows the data analysis of the $\sin^2 2\theta_{13}$ result, and additional uncertainty, the relative instability systematic uncertainty of the neutron detection efficiency, is included into the $\sin^2 2\theta_{13}$ result.

Chapter 2

Neutrino Mixing

2.1   Weak Interaction

The weak interaction can be described by the Standard Model very well. The Standard Electroweak Theory in the Standard Model is described by a leptonic Lagrangian density:[27]

$$L^L = L_0 + L_I. \tag{2.1}$$

L^L is invariant under the $SU(2) \times U(1)$[27] gauge transformations. L_0 is a free-lepton Lagrangian. The weak interaction between the coupling of quarks and leptons and the gauge vector bosons (Z and W) is shown by L_I.[28] L_I provides the interaction of the weak charged-current and the neutral-current, which can be written:[27]

$$L_I^{CC} = \frac{-g}{2\sqrt{2}}[J^{\mu^+}W_\mu + J^\mu W_\mu]. \tag{2.2}$$

$$L_I^{NC} = \frac{-g}{cos\theta_w}[J_3^\mu(x) - \frac{sin^2\theta_w S^\mu}{e}]Z_\mu \tag{2.3}$$

g is a coupling constant, and the angle θ_w is known as the Weinberg angle or the weak mixing angle. J^μ and $J^{\mu+}$ are leptonic currents. The third current, J_3^μ, is a weak isospin current, and it couples with a electromagnetic current, S^μ. The neutrino flavors, e, μ, and τ, are determined by the charged currents, J^μ. The gauge fields, W, expands $W^\pm$ vector bosons. Z_μ is a real vector field as a electrically neutral vector boson Z^0.[27] The charged

currents can be represented by Eq. 2.4.[27]

$$J^\mu = \overline{\psi_l}\gamma^\mu(1-\gamma_5)\psi_{\nu l}$$
$$J^{\mu+} = \overline{\psi_{\nu l}}\gamma^\mu(1-\gamma_5)\psi_l.$$

(2.4)

l is a charged lepton field. We can rewrite the lepton fields with the flavor neutrinos: ν_e, ν_μ, and ν_τ.

The number of light neutrino flavor is determined by the invisible width of Z boson.[28–30] In 1989, the measurement of the visible width of Z in the Large Electron-Position at CERN showed that the number of flavors of light neutrino is equal to 3.[28] Non-vanishing neutrino mass can be created by the coupling of lepton and Higgs fields through the Yukawa interaction. The neutrino mass can be derived from the Dirac mass (see Chapter 2.2) term and the Yukawa coupling between Higgs and lepton as all other fermions.[31] Dirac neutrino mass is similar as the mass of lepton and quark of Yukawa coupling as following[32]

$$L_{Yuk} = -c_\nu\overline{\nu_R}H\nu_L + h.c = m_D\overline{\nu_R}\nu_L.$$

(2.5)

C_ν is a Yukawa coupling constant, H is a doublet of complex field, and m_D is the Dirac neutrino mass. The left-handed and right-handed fields, ν_L and ν_R, are included into the Dirac neutrino mass term. If the neutrino eigenstate is its own antineutrino eigenstate, the equation can be written: $\nu_l = (\nu_l)^C$. A right-handed Majorana mass term can be build with a right-handed field, ν_R, and its charge-conjugate ,$(\nu_R)^C$ [1] as following[32]

$$L_{Yuk} = -c_\nu\overline{\nu_R}H\nu_R + h.c = m_R\overline{\nu_R}\nu_R.$$

(2.7)

Majorana mass term mixes neutrino and antineutrino, $\nu_l = (\nu_l)^C$; therefore, the conservation of lepton number in each leptonic family is violated. ($L(\nu_l) = -L(\overline{\nu_l})$) The Standard Model is required to introduce new model for Higgs Boson, which can violate $B - L$ (L: lepton

---

[1] Particle $f(x,t)$ and antiparticle $\overline{f}(x,t)$ are connected by the operator, charge conjugation C:[31]

$$C|f(x,t)\rangle = \eta_c|\overline{f}(x,t)\rangle.$$
$$C^\dagger = C^{-1} = C^T = -C$$

(2.6)

number, and B: Baryon number) and include the Majorana neutrino mass in the Yukawa coupling.[31]

The Yukawa coupling including the charged lepton masses and neutrino masses is defined as:

$$L_{mass} = \overline{l_R} \cdot \mathbf{m}_E \cdot l_L + \frac{1}{2}\overline{\nu_L} \cdot \mathbf{m}_\nu \cdot \nu_L \tag{2.8}$$

We can define the mass eigenstates, ν_i ($i = 1, 2, 3$), following the mass terms, m_i to describe ν_l in Eq. 2.8. The weak eigenstates, ν_l ($l = e, \mu, \tau$), can consist of the linear superpositions for the mass eigenstates in Eq. 2.9[22].

$$|\nu_l\rangle = \sum_i U_{l,i}|\nu_i\rangle. \tag{2.9}$$

U is an unitary mixing matrix from the Hermitian coupling matrix. The U matrix and the mass terms, m_i, in Eq. 2.9 can be obtained in the unitary gauge of the L^{Yuk} , and the neutrino mixing is brought forth naturally. In terms of Dirac neutrinos, the conservation of the individual lepton(e, μ and τ) number can be violated, but the total lepton number ($L_e + L_\mu + L_\tau$) is conservative. If the conservation of total lepton number is violated, the neutrino is a Majorana particle.

2.2 Dirac Mass Term

Dirac mass is generated by the Higgs mechanism (see Chapter 2.1). From the Dirac field, the Euler-Lagrange equation can be represented in Eq. 2.10.[31]

$$L = m_D\overline{\psi}\psi = m_D(\overline{\psi_R}\psi_L + \overline{\psi_L}\psi_R)$$
$$\overline{\psi_R}\psi_L = (\overline{\psi_L}\psi_R)^+. \tag{2.10}$$

Applying Eq. 2.10 to the neutrino mass, a neutrino mass consists of both left- and right-handed Dirac neutrinos.[31]

$$L = \sum_{i=1}^{3} m_i (\overline{\nu_{iR}} \nu_{iL} + \overline{\nu_{iL}} \nu_{iR})$$

$$|\nu_{lL}\rangle = \sum_i U_{l,i} |\nu_{iL}\rangle \tag{2.11}$$

$$|\nu_{lR}\rangle = \sum_i U_{l,i} |\nu_{iR}\rangle \, (l = e, \mu, \tau).$$

In the Standard Model, the $SU(2) \times U(1)$ gauge invariance only requires existence of the left-handed neutrino, which is defined the massless neutrino only (without L^{Yuk} coupling). From Eq. 2.12, three flavor-weak eigenstates are linear superpositions of the mass eigenstates, ν_i. However, only left-handed neutrinos are required in the standard weak interaction; the right-handed neutrinos are sterile. The unitary mixing matrix, U, called Cabibbo-Kobayashi-Maskawa matrix (CKM mass matrix) is shown by 3 mixing angles and 6 phase terms.

$$\begin{pmatrix} c_{12}c_{13} & s_{12}c_{13} & s_{13}e^{i\delta_{13}} \\ -s_{12}c_{23} - c_{12}s_{23}s_{13}e^{i\delta_{13}} & c_{12}c_{23} - s_{12}s_{23}s_{13}e^{i\delta_{13}} & s_{23}c_{13} \\ s_{12}s_{23} - c_{12}c_{23}s_{13}e^{i\delta_{13}} & -c_{12}s_{23} - s_{12}c_{23}s_{13}e^{i\delta_{13}} & c_{23}c_{13} \end{pmatrix} \tag{2.12}$$

The parameters in Eq. 2.12 are defined: $c_{ij} \equiv cos\theta_{ij}$, and $s_{ij} \equiv sin\theta_{ij}$, and δ_{13} is the CP-violation phase. From Eq. 2.12, δ_{13} is associated with s_{13} so the value of s_{13} will dominate the possibility of the measurement of CP-violation phase, δ_{13}.

2.3   Dirac Majorana Mass Term

We include the sterile neutrino into the mass term (Dirac right-handed fields). Due to a general treatment, the charge conjugation fields can be included in the Lagrangian, and it produces a mass term called Majorana mass.

$$L \frac{1}{2} m_M \overline{\psi} \psi^c + h.c... \tag{2.13}$$

The charge conjugated field ψ^c is defined by[31]

$$\psi \to \psi^c \equiv C\psi C^{-1} = \eta_c C \overline{\psi}^T. \tag{2.14}$$

The left-handed flavor fields, ν_{lL}, and the right-handed sterile fields, ν_{sR}, can make a new combination mass, which is called Dirac-Majorana mass term.[28] The Lagrangians from Dirac and Majorana terms are:

$$L^D = \Sigma_{sl}\overline{\nu_{sR}}M^D_{sl}\nu_{lL} + h.c...$$

$$L^M = \frac{1}{2}\sum_{ll'}\overline{(\nu_{lL})^c}M^L_{ll'}\nu_{l'L} + \frac{1}{2}\sum_{ss'}\overline{\nu_{sR}}M^R_{ss'}(\nu_{s'R})^c + h.c...$$

(2.15)

In Eq. 2.15, M^D, M^R, and M^L are the complex matrices, and s and l are the indications of neutrino flavors for the right-handed sterile fields and the left-handed flavor fields. The total Lagrangian L^{D+M} can be given:[31]

$$L^{D+M} = \frac{1}{2}(\sum_{sl}\overline{\nu_{sR}}M^D_{sl}\nu_{lL} + \sum_{sl}\overline{(\nu_{lL})^c}(M^D)^T_{sl}(\nu_{sR})^c +$$

$$\Sigma_{ll'}\overline{(\nu_{lL})^c}M^L_{ll'}\nu_{l'L} + \Sigma_{ss'}\overline{\nu_{sR}}M^R_{ss'}(\nu_{s'R})) + h.c...$$

$$= \begin{pmatrix} \overline{(\nu_L)^c} & \overline{\nu_R} \end{pmatrix}\begin{pmatrix} M^L & (M^D)^T \\ M^D & M^R \end{pmatrix}\begin{pmatrix} \nu_L \\ (\nu_R)^c \end{pmatrix} + h.c...$$

(2.16)

n_L defined as $(\nu_L, (\nu_R)^c)$ is called the left-haded vector. Eq. 2.16 can be written:[28]

$$L^{D+M} = \frac{1}{2}\overline{(n_L)^c}M^{D+M}n_L + h.c...;$$

$$n_L \equiv \begin{pmatrix} \nu_L \\ (\nu_R)^c \end{pmatrix};$$

$$M^{D+M} = \begin{pmatrix} M^L & (M^D)^T \\ M^D & M^R \end{pmatrix}$$

(2.17)

In Eq. 2.17, the left-handed vector can be transfer to neutrino three flavors, $\nu_{eL}, \nu_{\mu L}$, and $\nu_{\tau L}$. M is with a unitary matrix, U.[33,34]

2.4   See-Saw Mechanism

Now we consider a one-generation case of the Dirac-Majorana mass, the Lagrangian equation follows:

$$L^{D+M} = \frac{1}{2}\begin{pmatrix} \overline{(\nu_L)^c} & \overline{\nu_R} \end{pmatrix}\begin{pmatrix} m_L & m_D \\ m_D & m_R \end{pmatrix}\begin{pmatrix} \nu_L \\ (\nu_R)^c \end{pmatrix} + h.c...$$

(2.18)

We can diagonalize M and get the eigenstates, U_i, and the eigenvalues, λ_i:

$$\begin{pmatrix} m_L - \lambda & m_D \\ m_D & m_R - \lambda \end{pmatrix} \begin{pmatrix} U_1 \\ U_2 \end{pmatrix} = 0$$

$$\lambda_{1,2} = \frac{m_L + m_R \mp \sqrt{(m_L - m_R)^2 + 4(m_D)^2}}{2}. \tag{2.19}$$

The eigenstates of M can be easily defined as $U_1 = (A\sin\theta,\ A\cos\theta)$, and $U_2 = (B\cos\theta, -B\sin\theta)$, and the mixing angle θ is given:

$$\tan 2\theta = \frac{2m_D}{m_R - m_L}. \tag{2.20}$$

$(\nu_L, (\nu_R)^c)$ is given:

$$\begin{pmatrix} A\sin\theta & B\cos\theta \\ A\cos\theta & -B\sin\theta \end{pmatrix} \begin{pmatrix} \nu_{1L} \\ \nu_{2L} \end{pmatrix} = \begin{pmatrix} \nu_L \\ (\nu_R)^c \end{pmatrix}. \tag{2.21}$$

The eigenvalue λ_k can be a positive or negative value, and this sign is a CP parity of Majorana field.[28,31]

If we assume $m_L = 0$, m_D is close to the mass of the charged lepton, $m_R >> m_D$. The mass matrix, M, is given the other type:[35,36]

$$M \times U = \begin{pmatrix} -\lambda & m_D \\ m_D & m_R - \lambda \end{pmatrix} \begin{pmatrix} U_1 \\ U_2 \end{pmatrix} = 0$$

$$\lambda_{1,2} = \frac{m_R \mp \sqrt{(m_R)^2 + 4(m_D)^2}}{2}$$

$$U = \begin{pmatrix} 2A m_D & 2B m_D \\ A m_R + A\sqrt{(m_R)^2 + 4(m_D)^2} & B m_R - B\sqrt{(m_R)^2 + 4(m_D)^2} \end{pmatrix} \tag{2.22}$$

$$\lambda_1 \sim \frac{m_D^2}{m_R} << m_D;\ \lambda_2 \sim m_R$$

$$U \sim C \begin{pmatrix} m_D & m_R \\ m_R & m_D \end{pmatrix}.$$

Therefore, we can build a new diagonalized matrix with a very heavy mass of neutrino, $\lambda_2 = \lambda_{heavy}$, and a very light mass of neutrino, $\lambda_1 = \lambda_{light}$.

$$(U^+)^T M U = \begin{pmatrix} -\lambda_{light} & 0 \\ 0 & \lambda_{heavy} \end{pmatrix}. \tag{2.23}$$

Eq. 2.22 and 2.23 can be considered the see-saw mechanism for one generation. Considering

three flavors of neutrinos, we can get the three very light neutrinos, m_k ($k = 1, 2, 3$), and three heavy neutrinos, M_k. If we assume $M^L = 0$, the mass matrix shown in Eq. 2.17 can be rewritten:[28]

$$M^{D+M} = \begin{pmatrix} 0 & (M^D)^T \\ M^D & M^R \end{pmatrix}.$$ (2.24)

M^R has much bigger eigenvalues than the values of M^D in Eq. 2.22.[28] After approximating the orders of M_D and M_R, we can diagonalize the Eq. 2.24 and get two mass matrices for heavy mass and light masses.[28,37,38]

$$M_{heavy} \simeq M^R$$
$$M_{light} \simeq -(M^D)^T (M^R)^{-1} M^D.$$ (2.25)

If M^R is equal to $\mathcal{M}I$ (I is an identity matrix), the light neutrino masses can be described by the *quadratic see-saw*:[28]

$$m_1 : m_2 : m_3 = m_{D1}^2 : m_{D2}^2 : m_{D3}^2$$
$$m_k \simeq \frac{(m_{Dk})^2}{\mathcal{M}}.$$ (2.26)

m_D is the mass of charge lepton or quark mass.[28,31] If M^R is equal to $\frac{\mathcal{M}}{\mathcal{M}^D} M^D$ ($|M^D| = \mathcal{M}^D$), the ratio of the light neutrino mass is scaled by the mass, m_{Dk}:[28]

$$m_1 : m_2 : m_3 = m_{D1} : m_{D2} : m_{D3}$$
$$m_k \simeq \frac{\mathcal{M}_D m_{Dk}}{\mathcal{M}}.$$ (2.27)

The neutrino mass hierarchy of three light Majorana neutrino masses has the following form:[28]

$$m_1 << m_2 << m_3.$$ (2.28)

Chapter 3

Neutrino Oscillation

3.1   Oscillation Probability

The weak eigenstates, Eq. 2.9, can establish the phenomenon that a neutrino can transform from one flavor to another flavor. We can consider an eigenstate of mass m_i from Eq. 2.9, and let it propagate a certain distance, L.[22] The equation is

$$
|\nu_i(t)\rangle \simeq e^{-i(Et - p_i L)}|\nu_i(0)\rangle \simeq e^{-i(E(t-L) + m_i^2 L/2E)}|\nu_i(0)\rangle
$$
$$
p_i = \sqrt{E^2 - m_i^2} \simeq E - \frac{m_i^2}{2E^2}. \tag{3.1}
$$

In the laboratory coordinates, the momentum and the energy of a neutrino are much larger than its mass. In the $\nu_\alpha \to \nu_\beta$ transitions, we can assume: L $\simeq$ t. The mass eigenstates may be written:

$$
|\nu_i(L)\rangle \simeq e^{-i(m_i^2 L/2E)}|\nu_i(0)\rangle. \tag{3.2}
$$

The Eq. 3.2 can be substituted into Eq. 3.1, and the resulting equation is:[22]

$$
|\nu_l(L)\rangle \simeq \sum_i U_{l,i} e^{-i(m_i^2/2E)L} U_{l',i}^* |\nu_{l'}\rangle. \tag{3.3}
$$

The probability of the neutrino oscillation in the vacuum could be represented in Eq. 3.4.[39]

$$
\begin{aligned}
P(\nu_l \to \nu_{l'}) =& |\sum_i U_{l,i} U_{l',i}^* e^{-i(m_i^2/2E)L}|^2 \\
=& \sum_i |U_{l,i} U_{l'i}^*| - \sum_i \sum_j U_{li} U_{l'i}^* U_{lj}^* U_{l'j} e^{\frac{i(m_i^2 - m_j^2)L}{2E}} \\
=& \delta_{l,l'} - 4 \sum_{i>j} \mathcal{R}(U_{li} U_{l'i}^* U_{lj}^* U_{l'j}) \sin^2(\Delta m_{ij}^2 \frac{L}{4E}) + \\
& 2 \sum_{i>j} \mathcal{J}(U_{li} U_{l'i}^* U_{lj}^* U_{l'j}) \sin(\Delta m_{ij}^2 \frac{L}{2E})
\end{aligned}
\tag{3.4}
$$

$$
\begin{aligned}
P(\overline{\nu_l} \to \overline{\nu_{l'}}) =& \delta_{l,l'} - 4 \sum_{i>j} \mathcal{R}(U_{li} U_{l'i}^* U_{lj}^* U_{l'j}) \sin^2(\Delta m_{ij}^2 \frac{L}{4E}) \\
& - 2 \sum_{i>j} \mathcal{J}(U_{li} U_{l'i}^* U_{lj}^* U_{l'j}) \sin(\Delta m_{ij}^2 \frac{L}{2E}).
\end{aligned}
\tag{3.5}
$$

In Eq. 3.4 and 3.6, Δm_{ij}^2 is equal to $m_i^2 - m_j^2$. The first two terms of the neutrino and anti-neutrino probabilities, $\delta_{l,l'} - 4\mathcal{R} \sum_{i>j} U_{li} U_{l'i}^* U_{lj}^* U_{l'j} \sin^2(\Delta m_{ij}^2 \frac{L}{4E})$, are the same; however, a complex unitary matrix, U, causes $P(\overline{\nu_l} \to \overline{\nu_{l'}}) \neq P(\nu_l \to \nu_{l'})$, the CP violation. For $l \neq l'$, Eq. 3.4 can be given:

$$
\begin{aligned}
P(\nu_l \to \nu_{l'}) =& \sum_j |\sum_i U_{l,i} U_{l',i}^* e^{-i(m_i^2/2E)L} e^{-i(m_j^2/2E)L}|^2 \\
=& |U_{l3} U_{l'3}^* (e^{2i\Delta_{31}} - 1) + U_{l2} U_{l'2}^* (e^{2i\Delta_{21}} - 1)|^2 + |U_{l3} U_{l'3}^* (e^{2i\Delta_{32}} - 1) + \\
& U_{l1} U_{l'1}^* (e^{2i\Delta_{21}} - 1)|^2 + |U_{l1} U_{l'1}^* (e^{2i\Delta_{31}} - 1) + U_{l2} U_{l'2}^* (e^{2i\Delta_{32}} - 1)|^2 \\
=& 4(\sum_j |U_{lj} U_{l'j}^*|^2 \sum_{i>j} \sin^2 \Delta_{ij} + 2 \sum_{i>j, k \neq i,j} |U_{li} U_{l'i}^* U_{lj}^* U_{l'j}| \sin\Delta_{ik} \sin\Delta_{jk} \cos(\Delta_{ij} - \delta_{ij})).
\end{aligned}
\tag{3.6}
$$

Δ_{ij} is equal to $(m_i^2 - m_j^2)L/4E$. We assume: $\delta_{ij} \equiv Arg(U_{li} U_{l'i}^* U_{lj}^* U_{l'j})$. δ_{ij} is the CP-violation phase depending on the neutrino or anti-neutrino transitions. The CP-violation phase is not considered in a special case of $P(\overline{\nu_e} \to \overline{\nu_e})$:

$$
\begin{aligned}
P(\overline{\nu_e} \to \overline{\nu_e}) = P(\nu_e \to \nu_e) =& 1 - 4(\cos^4\theta_{13} \sin^2\theta_{12} \cos^2\theta_{12} \sin\frac{\Delta_{21}L}{4E} + \\
& \sin^2\theta_{13} \cos^2\theta_{12} \cos^2\theta_{13} \sin\frac{\Delta_{31}L}{4E} + \sin^2\theta_{13} \sin^2\theta_{12} \cos^2\theta_{13} \sin\frac{\Delta_{32}L}{4E}).
\end{aligned}
\tag{3.7}
$$

3.2 Oscillation in the Two-Neutrino Model

A large scale of the $\Delta m^2_{31} = \Delta_{31}$ dominates the mass hierarchy, and the neutrino mass spectrum is divided into two hierarchies, the normal hierarchy and the inverted hierarchy. The normal and inverted hierarchies are represented schematically in Fig. 3.1. The approximation of $P(\nu_l \to \nu_{l'})$ at the limit $|\Delta m^2_{21}| << |\Delta m^2_{31}|$ is given in Eq 3.8.[39]
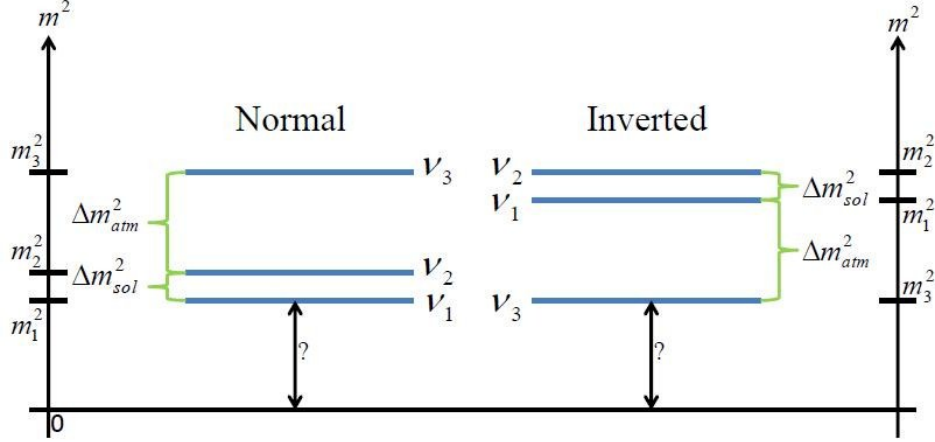
Figure 3.1: The mass schematic of normal and inverted hierarchies. Δm_{atm} is defined as Δm_{32} in the normal hierarchy, and Δm_{atm} is defined as Δm_{31} in the inverted hierarchy. Δm_{sol} is defined as Δm_{21}.

$$P(\nu_l \to \nu_{l'}) \simeq 4 \sum_j |U_{lj}U_{l'j}^*|^2 \sin^2\frac{\Delta m^2 L}{4E}(l \neq l')$$

$$P(\nu_l \to \nu_l) \simeq 1 - 4 \sum_{i \neq j} |U_{li}U_{li}^*U_{lj}^*U_{lj}|\sin^2\Delta m^2\frac{L}{4E} \qquad (3.8)$$

$$= 1 - 4 \sum_j |U_{lj}|^2(1 - \sum_j |U_{lj}|^2)\sin^2\frac{\Delta m^2 L}{4E}.$$

The normal hierarchy (or inverted hierarchy) is applied to Eq. 3.8, only considering Δm^2_{13} and θ_{13}, and the survival probability of the $\overline{\nu_e}$ and ν_e are:[22]

$$P(\overline{\nu_e} \to \overline{\nu_e}) = P(\nu_e \to \nu_e) \simeq 1 - \sin^2 2\theta_{13}\sin^2\frac{\Delta m^2_{13}L}{4E}. \qquad (3.9)$$
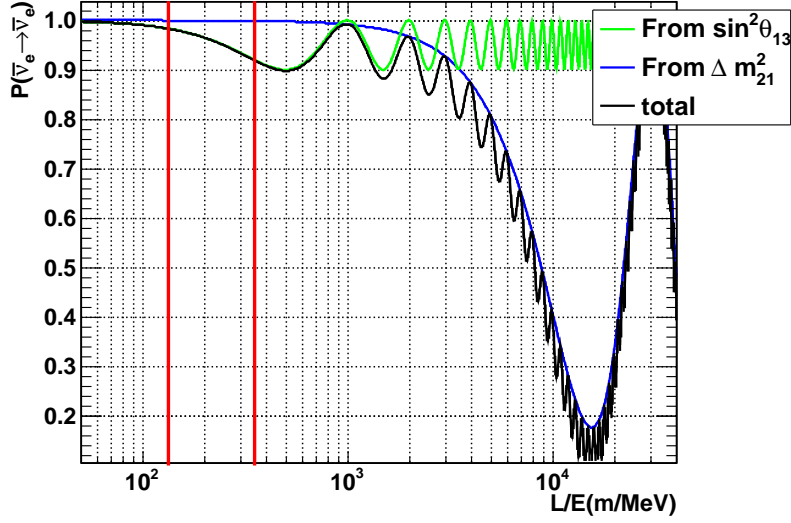
Figure 3.2: $P(\overline{\nu_e} \to \overline{\nu_e})$, the survival probability of Eq. 3.7 as a function of neutrino energy. The green curve is contributed from $\sin^2 theta_{13}$. The blue curve is contributed from Δm^2_{12}. The two red lines indicate the Double Chooz far and near detector locations.

Considering only two flavors and two mass eigenstates, the mixing matrix, U, can be written as:[22]

$$U = \begin{pmatrix} \cos\theta & \sin\theta \\ -\sin\theta & \cos\theta \end{pmatrix}. \tag{3.10}$$

According to Eq. 3.10, the probabilities of neutrino transitions are:

$$
\begin{aligned}
P(\nu_l \to \nu_l) &= |\cos^2\theta + \sin^2\theta e^{-i\frac{\Delta m^2 L}{2E}}|^2 = 1 - \sin^2 2\theta \sin^2 \frac{\Delta m^2 L}{4E}. \\
P(\nu_l \to \nu_{l'}) &= |\cos\theta\sin\theta - \sin\theta\cos\theta e^{-i\frac{\Delta m^2 L}{2E}}|^2 = \sin^2 2\theta \sin^2 \frac{\Delta m^2 L}{4E}.
\end{aligned}
\tag{3.11}
$$

From Eq. 3.11, the probabilities from the two-flavor neutrino transition are the same as the three-flavor neutrino transition in the hierarchy limit, $|\Delta m^2_{21}| << |\Delta m^2_{31}|$. The sensitivity of Δm^2 can be easily determined by the oscillation length:[22].

$$
\begin{aligned}
L_{osc} &= \frac{4\pi E}{\Delta m^2} \\
L_{osc}(km) &= \frac{\pi E(\text{GeV})}{1.27\Delta m^2(\text{eV}^2)}.
\end{aligned}
\tag{3.12}
$$

Figure 3.2 shows the $\overline{\nu_e}$ survival probabilities as the functions of neutrino energy. The black curve contributed from all fractions in Eq. 3.7, approximates Eq 3.11, the two-flavor

15

neutrino transition. The oscillation characteristics of the neutrino flavor is observed from the oscillation length, Eq. 3.12. The larger value of $\frac{E}{L}$ the detector has, the larger value of Δm^2 the detector can probe. A measurement must be located at the distance, $L \gtrsim L_{osc}$, or one cannot observe the neutrino oscillation phenomena.

A mass spliting, Δm^2_{atm}, first was observed by a deficit of atmospheric neutrinos from the Super-Kamiokande (SK) Collaboration in 1998 as shown in Fig. 3.3. The atmospheric neutrinos, mostly muon neutrinos and muon antineutrinos, transfer to another flavor neutrino showing a clear deficit in the neutrino probability. The Super-Kamiokande experiment discriminated the particle categories with the patterns of the events from their water Cherenkov detector. Particularly, single-ring events can be identified as being produced by the Chrenkov light from a single charge lepton. The particle, which is e-like or μ-like, can be determined by the pattern of rings. Usually, a ring from a e-like event would be more fuzzy than from a μ-like event because of the Coulomb scattering in the water and the electron shower. In the hypothesis, the disappearing ν_μ transfers into the ν_τ, and Δm^2 is around 10^{-3} eV^2 [40]. The atmospheric neutrino energy is around $1 \sim 10$ GeV from the SK-I zenith-angle measurement.[40] From the oscillation parameter analysis, the results are $1.5 \times 10^{-3} < |\Delta m^2_{atm}| < 3.4 \times 10^{-3}$ eV^2 and $\sin^2 2\theta_{atm} > 0.92$.[40] The data cannot prove that ν_μ transferred into ν_τ in the 10,000 km journey. However, a high L/E resolution analysis excluded other guesses like that neutrinos could decay into other particles. According to the SK-I results from the L/E analysis, $1.9 \times 10^{-3} < |\Delta m^2_{atm}| < 3 \times 10^{-3} eV^2$ and $\sin^2 2\theta_A > 0.90$ are showed in Figure 3.3.[41]

The Δm^2_{atm} range has been further studied by the accelerator long-baseline experiments, $L_{osc} \sim$ several kilometers and $E \sim 1$ GeV. The first long-baseline neutrino experiment is called K2K (KEK to Kamioka). SuperKamiokande is the far detector, which is 250 km away from the near detector. A neutrino beam is produced by a 12 GeV-proton beam from KEK-PS, and the neutrino average energy is around 1.3 GeV. In two-neutrino oscillation case, K2K gave the range, $1.9 \times 10^{-3} < |\Delta m^2_{atm}| < 3.5 \times 10^{-3}$ eV^2, at the 90% C.L when $\sin^2 2\theta_A$ is equal
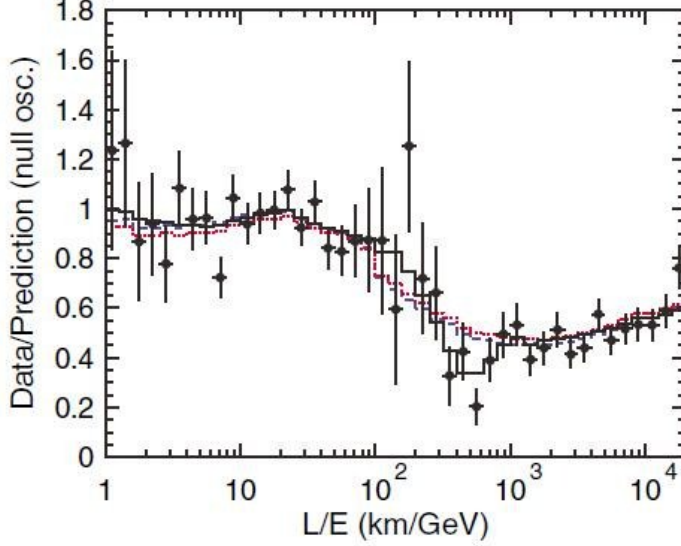
Figure 3.3: The $\nu_\mu \to \nu_\tau$ result of the SK-I L/E analysis. The ratio of the data to the Monte Carlo expectation without neutrino oscillation indicates black points, and solid curve is the best fit of the neutrino oscillation, $\nu_\mu \to \nu_\tau$. The error bars are the statistical error. This plot is taken from the study of the Super-Kamiokande Collaboration.[41]

to 1.0.[42] The second long-baseline neutrino oscillation experiment is MINOS. Its far detector is a 5.4 kton iron-scintillator away from the near detector, a 0.98 kton iron-scintillator. Its neutrino beam is from the Fermilab Main Injector. The newest $\Delta m_{atm}^2 = (2.32^{+0.12}_{-0.08}) \times 10^{-3} \text{eV}^2$ has been provided from the MIONS experiment.[43] The Δm^2 vs. mixing angle, $\tan^2\theta$, region is represented in Figure 3.4 following various neutrino oscillation experiments.

Solar neutrinos are from the fusion reactions of CNO cycle and pp chain. The total reaction can be written:

$$4p + 2e^- \to^4 He + 2\nu_e + 26.73 \text{ MeV} - E_\nu. \tag{3.13}$$

The average energy, E_ν, taken from neutrinos is about 0.6 MeV. The solar neutron, ν_e, is estimated by the flux on the basis of the standard solar model (SSM). Most SSM calculations are from John Bahcall and his collaborators. The BS05(OP) model is presented in Figure 3.5.[45] However, a deficit of the neutrino flux from the SSM prediction was an

17
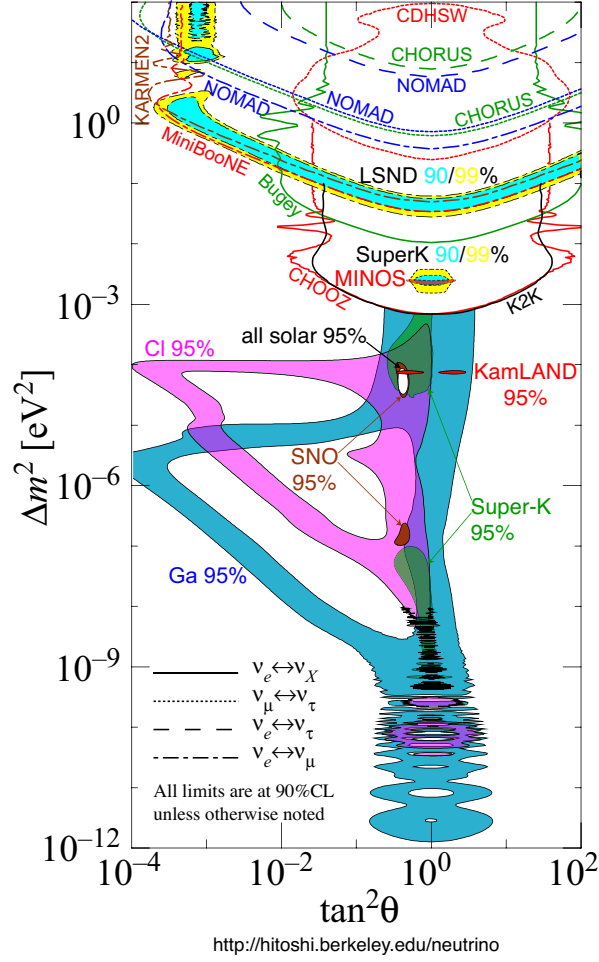
Figure 3.4: The regions of Δm^2 and $\tan^2\theta$ distributions from various experiments. This plot is taken from H. Murayama at the Department of Physics, University of California.[44]

unsolved problem before the neutrino flavour translation assumption. The translation of $\nu_e \to \nu_{\mu,\tau}$ can be represented by the flux of non-ν_e, $\phi(\nu_\mu, \nu_\tau)$. The solar problem has been solved by the SNO experiment collecting the neutrino flux from ^8B decay. The SNO experiment applies three reactions (the rates of neutral current (NC), charged current (CC) and elastic scattering (ES)) to find the summation of ^8B flux. Three reactions are:

$$\nu_x + d \to p + n + \nu_x (NC),$$

$$\nu_e + d \to p + p + e^- (CC), \quad\quad (3.14)$$

$$\nu_x + e^- \to \nu_x + e^- (ES).$$

A significant difference between the fluxes of NC and CC reactions is an obvious evidence to
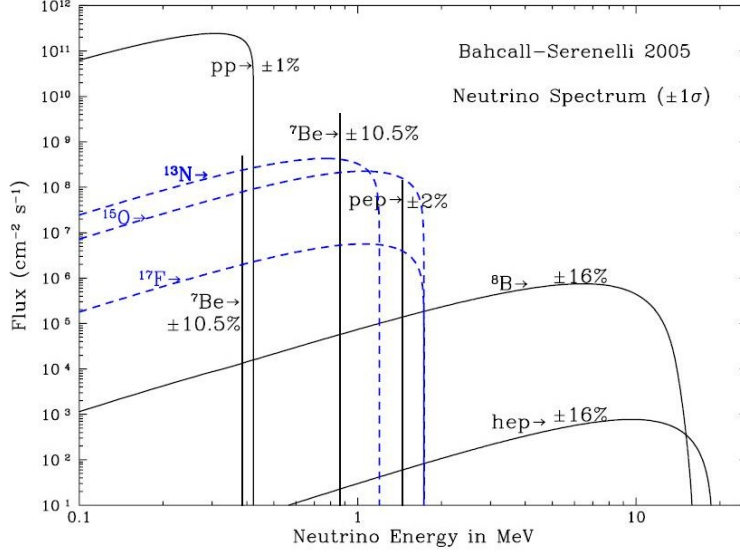
Figure 3.5: The predicted solar neutrino spectra from the model ,BS05(OP). This plot is from http://www.sns.ias.edu/ jnb/. The spectra are calculated by the mode, BS05(OP)[45]. The unit of the neutrino flux is $cm^{-2}s^{-1}MeV^{-1}$ of the solid line spectra.

prove the neutrino flavor transition. By comparing the NC and CC rates, SNO determines the survival probability as a function of neutrino energy. The mixing parameters as measured by SNO are $\Delta m_{21}^2 = 5.6_{-1.4}^{1.9} \times 10^{-5}eV^2$ and $\tan^2\theta_{12} = 0.427_{-0.029}^{+0.033}$ in the two flavor neutrino oscillation.[46] Furthermore, the reactor neutrino experiment, KamLAND, gave the result, $\Delta m_{21}^2 = 7.58_{-0.13}^{+0.14}(\text{stat.})_{-0.15}^{+0.15}(\text{syst.}) \times 10^{-5}$ eV^2 and $\tan^2\theta_{12} = 0.56_{-0.07}^{0.10}(\text{stat.})_{-0.06}^{0.10}(\text{syst.})$ by measuring the $\overline{\nu_e}$ survival probability of the reactor neutrino over the long base line, 180 km.[47] This experiment observes $\overline{\nu_e}$ with IBD:

$$\overline{\nu_e} + p \rightarrow e^+ + n \qquad (3.15)$$

KamLAND's result is the first evidence that the $\overline{\nu_e}$ survival probability has a periodic feature as a function of oscillation length (Eq. 3.12). In first KamLAND result, the average ratio of the number of observed neutrino events to the expected number without oscillation is Eq. 3.16.[40,48]

$$\frac{N_{obs} - B_{BG}}{N_{NoOsc}} = 0.611 \pm 0.085(\text{stat.}) \pm 0.041(\text{syst.}). \qquad (3.16)$$

Figure 3.6 shows the periodic feature of the $\overline{\nu_e}$ survival probability from the KamLAND

result in 2008.
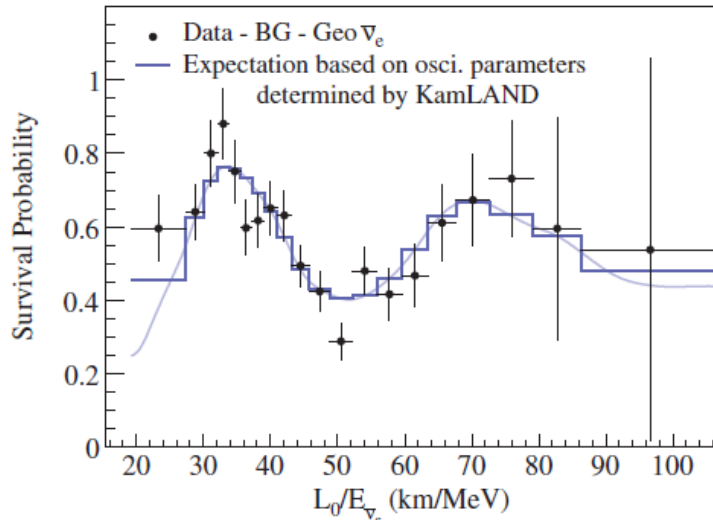
Figure 3.6: The ratio of the data events (subtracted background and geoneutrino) to the no oscillation predicted spectrum as a function of the $\frac{L_0}{E_{\overline{\nu}_e}}$ from the KamLANDLE experiment. This plot is taken from the KamLAND result[47]. The L_0, the base line, is 180 km. The blue curve is the best-fit of the $\overline{\nu}_e$ survival probability.

According to the two-neutrino oscillation analysis from SNO Collaboration's newest update (using its Phase I and Phase II), the results are: 1) $\Delta m_{sol} = 7.59^{+0.20}_{-0.21} \times 10^{-5} eV^2$ and $\tan^2\theta_{sol} = 0.457^{0.040}_{-0.029}$ from the global solar analysis+KamLAND.[40], and 2) $\Delta m_{sol} = 5.89^{+2.13}_{-2.16} \times 10^{-5} eV^2$ and $\tan^2\theta_{sol} = 0.457^{0.038}_{-0.041}$ from the global solar analysis.[49] Two neutrino oscillation analyses from the global solar neutrino+KamLAND and the global solar neutrino are represented in Fig 3.7.(without joining Phase I and Phase II)[50]

Δm^2_{atm} is sensitive at the range $L \sim 1$ km, $\langle E \rangle \sim 3$ MeV in the reactor $\overline{\nu}_e$ disappearance experiment. At this condition, the experiment can ignore the contribution from Δm_{sol}. The first experiment of this kind was the Chooz experiment at the Chooz nuclear power plant in France. The $\overline{\nu}_e$ were detected by the IBD, and neutrons from IBD were captured by gadolinium (Gd) in the liquid scintillator. The result did not show out a clear evidence to prove the $\overline{\nu}_e$ disappearance at 90% CL. The result from the CHOOZ experiment is $\sin^2 2\theta_{13} < 0.10$.[51] The K2K experiment, an accelerator neutrino oscillation experiment,

20
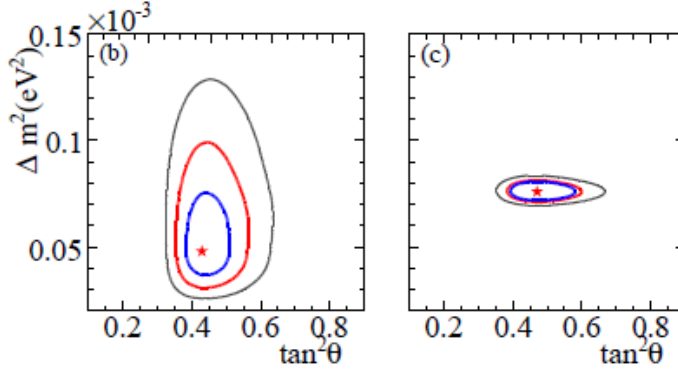
Figure 3.7: The range of the Δm^2 vs. $\tan^2\theta$ distribution at 68%, 95%, and 99.73% CL ranges. The best-fit result of the global solar neutrino data is the left-hand side plot, and the best-fit result of the global solar + KamLAND data is the right-hand side plot. Two plots are taken from the SNO updated result.[50]

applied $\nu_\mu \to \nu_e$ to search for θ_{13}; however, it did not indicate any evidence. The result from the K2K experiment is $\sin^2 2\theta_{13} < 0.26$ at $\Delta m^2 = 2.8 \times 10^{-3} \text{eV}^2$ 90% CL.[52] In the accelerator neutrino oscillation experiments, the measurement of $\sin^2 2\theta_{13}$ varies with the Δm^2_{32}, and the deviation of θ_{23} provides a larger uncertainty to future experiments.[40] Therefore, the accelerator neutrino oscillation experiment is not a good candidate to search for $\sin^2 2\theta_{13}$ in the future.

After the previous experiments, multi-detector systems for reactor disappearance experiments were developed. Basically, the base line is still ~ 1 km, but a near detector is added into to the system. The systematic uncertainties are reduced due to the additional near detector. There are three new experiments, Double Chooz, RENO, and Daya Bay, which are based on the idea. We will discuss more details about the Double Chooz experiment in the next chapter.

21

Chapter 4

Double Chooz Detector Experiment

The Double Chooz detector system is a four-layer concentric cylindrical detector with a calibration system. The innermost acrylic vessel is filled with the 10.3 m^3 ν-target liquid. The ν-target liquid scintillator (NT) is consisted of the mixture of ortho-phenylxylylethane and (o-PXR)/n-dodecane, PPO (2,5-diphenyloxazole), bis-MSB (4-bis-(2-methylstyryl)benzene), and Gd (1 g/liter).[1] The NT is surrounded by the gamma catcher (GC), which is a 55 cm thick liquid scintillator layer without Gd.[5] The NT and GC are in 8 mm and 12 mm thick acrylic vessels respectively. The third layer is the buffer, which is filled with 105 cm thick mineral oil. The fourth layer is the inner veto tank, a 50 cm thick liquid scintillator.[1] The main cylindrical detector is coved by an outer veto system (OV), a plastic scintillator assembly. (Figure 4.1[5])

Electron antineutrinos produced by two reactors are detected by IBD, $\overline{\nu_e} + p \rightarrow e^+ + n$, in the detector. The positron from the IBD is called a prompt signal seen immediately. The neutron signal from IBD is called a delayed signal captured by the Gd in the NT, and the mean time between prompt and delayed signals is about 30 μs.[5] The outside GC can detect the escaping gamma rays from the NT. The buffer, one of the major improvements from the Chooz experiment, reduces the radioactive background from the photomultiplier tubes (PMTs) and the rock surrounding our laboratory. It is also a support for 390 10-inch PMTs, which collect the light inside the inner volume. The inner detector (ID) consists of three parts, the NT, the GC and the buffer tank. The inner veto (IV), containing 78 8-inch

upper OV

glove box (GB)

outer veto (OV)

inner veto (IV)

buffer (B)

stainless steel vessel
holding 392 PMTs

gamma catcher (GC)

acrylic vessels

v-target (NT)

steel shielding
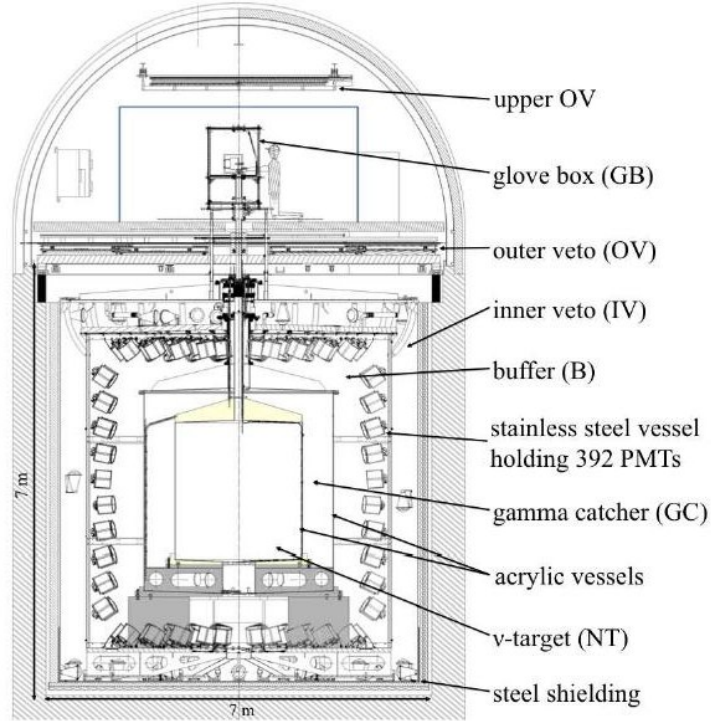
Figure 4.1: The cross section of the Double Chooz detector schematic diagram.[5]

PMTs, can tag cosmic muons and spallation neutrons from the outside of the detector. In order to suppress the background gamma rays, a 15-cm demagnetized steel layer surrounds the whole detector.[5]

4.1   Reactor Description

The electron antineutrinos are from reactor cores B1 and B2 located at the Électricité de France (EDF) Centrale Nucléaire de Chooz. The $\overline{\nu_e}$ flux produced by fissioning the four main isotopes, ^{235}U, ^{239}Pu, ^{238}U and ^{241}Pu, in the nuclear reactors accounts for more than 99.7% of the total flux. Two reactor cores are N4 type pressurized water reactor (PWR) cores.[5] The instantaneous thermal power can be measured by the heat flow from the water headed by the fissions. The primary source of uncertainty in the reactor power measurement is from the water flow. The nominal full thermal power for one reactor is 4250 MW$_{\text{th}}$, and

23

the uncertainty is 0.5% (1σ C.L.).[5]

Two reactor simulation codes, MURE[53,54] and DRAGON[55], are applied to evaluate the fission rates and associated errors. The systematic uncertainty based on the comparison between MURE and DRAGON is smaller than 0.2%.[5] Although the simulations can describe that the $\overline{\nu_e}$ spectrum agrees with the experimental result; the high uncertainty, 3%, is too large and limits the sensitivity of the $\sin^2 2\theta_{13}$ result. We introduce the Bugey4's rate measurement to reduce the large uncertainty because of the uncertainty, 1.4%, of Bugey4 measurement.[56] The strategy is that each fission of the reactor normalizing the cross section is related to the Bugey4's result producing an additional corrective term. Eq. 4.1[5] shows the normalized cross section described by Bugey4's result and the additional corrective term:

$$\langle \sigma_f \rangle_R = \langle \sigma_f \rangle^{Bugey} + \sum_k (\alpha_k^R - \alpha_k^{Bugey}) \langle \sigma_f \rangle_k. \tag{4.1}$$

In Eq. 4.1, σ_f is the cross section per fission, R indicates each reactor, and α_k is the fractional fission rate[57] of each isotope. The corrective term in Eq. 4.1 is equal to $\alpha_k^R - \alpha_k^{Bugey}$. The $\overline{\nu_e}$ no-oscillation expected number from the reactor is[5]

$$N_i^{exp} = \frac{\epsilon N_p P_{th}^R}{4L_{R^2} \langle E_f \rangle_R} \times \left(\frac{\langle \sigma_f \rangle_R \Sigma_k \alpha_k^R \langle \sigma_f \rangle_k^i}{\Sigma_k \alpha_k^R \langle \sigma_f \rangle_k} \right). \tag{4.2}$$

In Eq. 4.2, N_p is the number of protons in the NT, ϵ is the detection efficiency, L_R is the distance between each reactor to the detector, and P_{th}^R is the thermal power of the reactor. Since the electron neutrinos from reactors are at the low energy range, we can assume that the protons are static in the detector, and the neutron recoil can be neglected. The total energy can be described in Eq. 4.3 for the IBD.

$$E_{\overline{\nu}} + M_p = E_e^0 + M_n. \tag{4.3}$$

The threshold energy of the IBD is[22]

$$E^{thr} = \frac{(M_n + m_e)^2 - M_p^2}{2M_p} = 1.806 \text{MeV} \tag{4.4}$$

The differential cross section and the total cross section are shown in Eq. 4.5.[58]

$$
\left(\frac{d\sigma}{d\cos\theta}\right)^0 = \frac{\sigma_0}{2}[(f^2 + 3g^2) + (f^2 - g^2)v_e^0\cos\theta]E_e^0 p_e^0
$$

$$
\sigma_{total}^0 = \sigma_0(f^2 + 3g^2)E_e^0 p_e^0 = \frac{0.0952 E_e^0 p_e^0}{1\text{MeV}^2} \times 10^{-42}\text{cm}^2. \tag{4.5}
$$

In Eq. 4.5, E_e^0 is equal to $E_\nu - M_n + M_p$, p_e is equal to $\sqrt{E^2 - m_e^2}$, and v_e is equal to $\frac{p_e}{E_e}$. The f is a vector constant equal to 1, and g is an axial-vector constant equal to 1.26. The positron energy can be described in Eq. 4.6. We can use the simplified cross section from Eq. 4.5 to derive the positron spectrum. We assume that the angle between an antineutrino and a positron is equal to 0. The approximate positron energy can be derived from an antineutron energy shown in Eq. 4.6.[22]

$$
E_\nu \simeq (E_e + \Delta)(1 + \frac{E_e}{M_p}) + \frac{\Delta^2 - m_e^2}{M_p}
$$

$$
E_e = \frac{-M_n + \sqrt{M_n^2 - 4M_p(-E_\nu + \Delta + (\Delta^2 - m_e^2)/M_p)}}{2} \tag{4.6}
$$

Therefore, Eq. 4.6 can be substituted into E_e in Eq. 4.5, and finally the IBD cross section is shown in Eq. 4.7.[58]

$$
\sigma_{IBD}(E_{\bar{\nu}}) = E_e p_e \times 0.961 \times 10^{-42}\text{cm}^2\text{MeV}^{-2} \tag{4.7}
$$

4.2   Detector Description

The detector model is reconstructed by a Geant4[59,60] simulation including the photocathode optical surface model and geometry, the scintillation process, and the thermal neutron model.[5] The scintillation process is based on the components of the scintillator. In the NT, the scintillator solvent consists of 20% ortho-phenlyxylyethane (o-PXE) and 80% n-dodecane.[5] The hydrogen fraction is 13.6% in the NT. The Gd concentration is about 1 g/liter, 0.123 %, in the NT.[5] The PPO (2,5-dipheny loxazole)[5] is a primary flour, and the bis-MSB (4-bis-(2-methylstyryl)benzene)[5] is a wavelength length shifter for PMTs in the NT and IV. The GC liquid is added the third solvent, a medicinal white oil, to guarantee that

the GC's optical properties are consistent with the NT's optical properties.[1] The buffer liquid consists of 53% medicinal white oil and 47% n-alkane mixture. The IV contains a liquid scintillator, a mixture of linear alkyl benzene (LAB) and nalkanes, with PPO and bis-MSB. The detector structure is reconstructed by the Geant4 reference physics list, `QGSP BERT HP`. The optical process includes the spectra, the re-emission quenching, and the Birk's law.[61] The PMT optical model takes into account the absorption and index parameters in the thin and semitransparent surface. The shield metal and other material supporting the PMT are all included in the simulation. The PMT configuration is represented in Figure 4.2.[62] The PMT geometry model is based on the measurements of the detector after construction. The
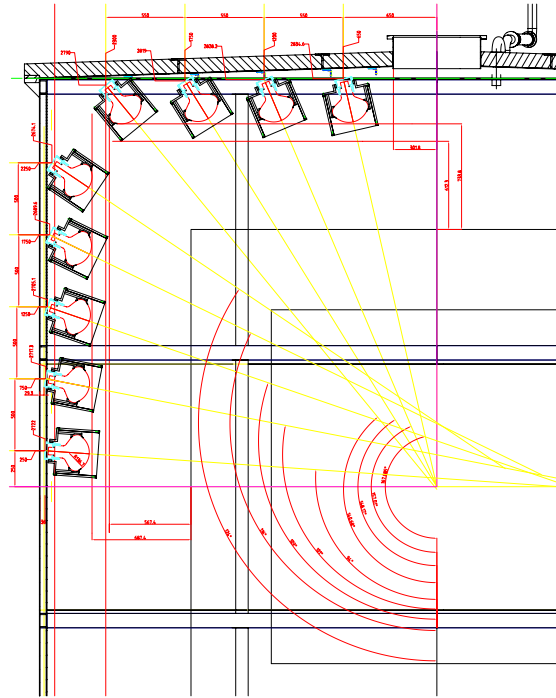
Figure 4.2: Double Chooz PMTs' configuration in the buffer for the PMT geometry model. This configuration is taken from D. Shrestha and G. Horton-Smith, "The Good Enough PMT Pointing studying", neutrino.phys.ksu.edu, 2007.[62]

neutron thermalization process in the model is calculated by the molecular elastic scattering in the Double Chooz liquid taking into account below 4 eV.[5]

Optical parameters in the Monte Carlo simulation were determined by bench experiments. The extracted liquid from each volume were tested by the benchmeasurements.[5,63] A Compton backscatter peak method was used to determine the relative light yield as a function of electron energy for the NT and the GC.[5,63,64] The Compton scattering also includes the Cerenkov light study.[65] The absolute light yield in the Monte Carlo simulation has been tuned by the radioactive source deployment in the NT and the GC.[65] My collaborators used a Cary Eclipse fluorometer[66] to measure the scintillator emission spectrum. In order to avoid the Cerenkov light effect, the quench bench measurements were applied with alpha and electron sources at the different energy to determine the quench effect and the Birk's parameters.[67]

4.3   Visible Energy Calibration

After we have the precise optical parameters, the visible energy (E_{vis}) measured from the calorimetry needs to be calibrated by four terms shown in Eq. 4.8. The calorimetry estimates the E_{vis} deposited per trigger. The visible energy can be described by the calibrated total number of photoelectrons (PE):[5,68]

$$E_{vis} = PE^m(\rho, z, t) \times f_u^m(\rho, z) \times f_s^m(t) \times f_{MeV}^m.$$
$$PE = \sum_i pe_i = \sum_i q_i/gain_i(q_i). \tag{4.8}$$

In Eq. 4.8, t is time, and i is each good channel of PMTs. According to the concentric cylindrical detector, we define the coordinates, ρ and z. We define m to indicate data or Monte Carlo simulation. The correction terms include a spatial uniformity (f_u^m), a time stability (f_s^m), and a PE/MeV calibration, (f_{MeV}^m). In Eq. 4.8, E_{vis} relies on these four calibration terms, and thus data and Monte Carlo energy scales agree with each other. In the Double Chooz experiment, we only choose good channels to reconstruct the raw charge (q_i) in Eq. 4.8. The good channels were judged by the waveform information from a fast online analysis system. The waveform baseline bias can cause a nonlinear effect shown in

the 1 PE equation, Eq. 4.8. The function, $gain_i(q_i)$, corrects the non-linearity of the single-PE charge, and it is generated upon each power cycle as well.[5,68] A nonlinear effect for one channel as a function of raw charge is represented in Figure 4.3. The second term, $f_u^m(\rho, z)$,
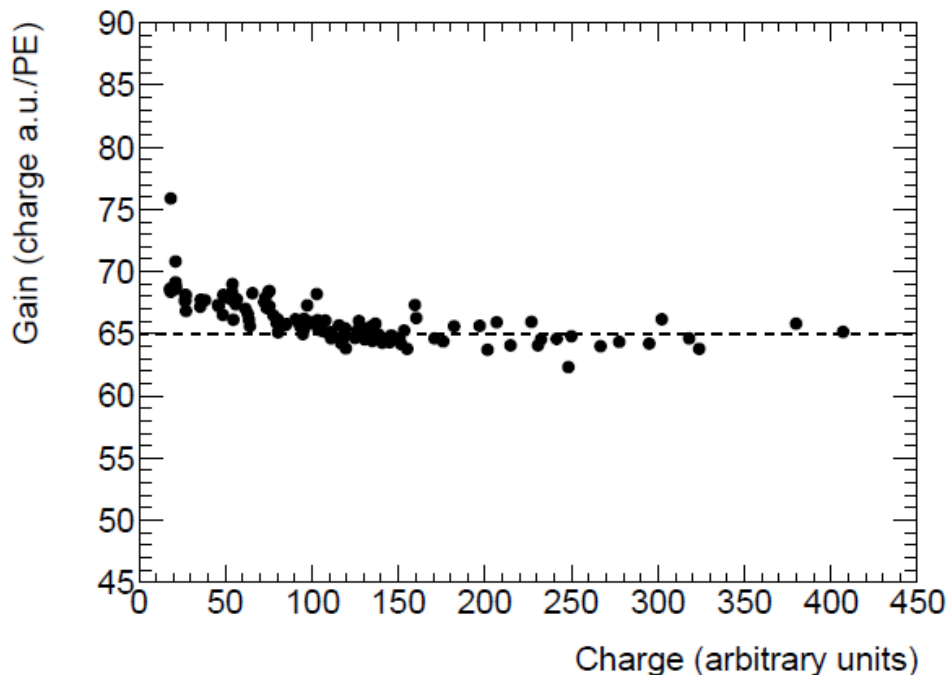
Figure 4.3: A linear PE calibration as function of raw charge and a nonlinear effect near the lower raw charge are shown in this plot. The nonlinear range leads the energy scale linear corrected to within 2 %. This plot is from the publication of Double Chooz Collaboration.[5]

is the positional dependence of the PE distribution in the NT and the GC. We describe the corrective term as a function of ρ and z directions by the spallation neutrons and the antineutrons at H-capture 2.223 MeV filling the NT and the GC. This correction depends on the NT center $(\rho = 0, z = 0)$ to describe the PE function: $PE_c^m = PE^m(\rho, z) \times f_u^m(\rho, z)$. The correlative terms is determined individually from the data and the Monte Carlo situations for two dimensional maps. The largest deviation for the data in the NT is up to 5 % in the calibration map.

The energy scale deviates with the elapsed time due to variations in the channel's readout

gain and the scintillator optical properties. This phenomenon can be calibrated by the energy of spallation neutrons capture events on Gd as shown in Figure 4.4. Some PMT
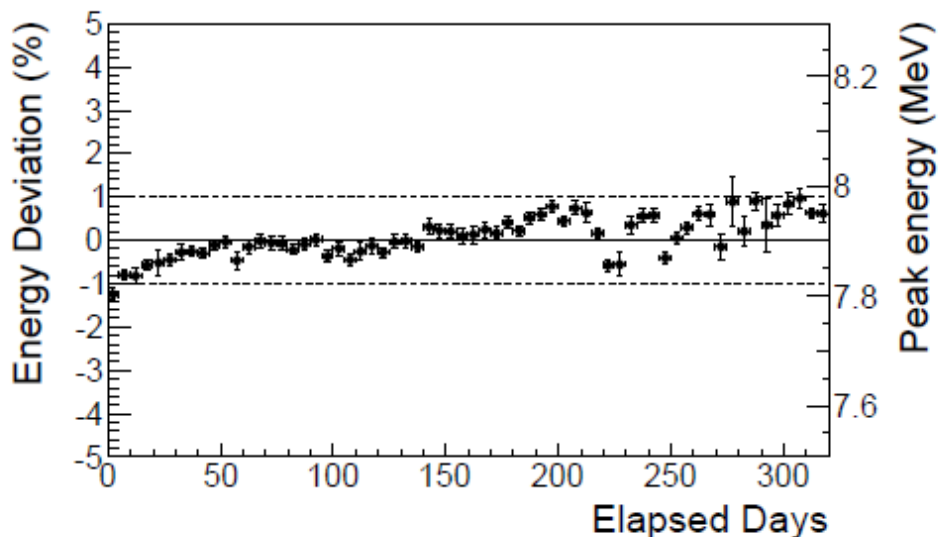
Figure 4.4: The deviation of the Gd-capture peak position as a function of elapsed day. This plot shows the deviation of the Gd-capture energy position before the energy scale calibration. The peak position has increased as a +2.2% with the elapsed days. The plot is from the publication of the Double Chooz Collaboration.[5]

channels are excluded from the calorimetry sum due to their anomalous charge integrations (identified by the fast-online analysis). Each excluded channel can decrease the average detector response by 0.3 %.[68] This correction does not apply on the Monte Carlo simulation because the Monte Carlo simulation does not change with time.[5,68] The $PE(t)$ converted function can be described as $PE_c^m(\rho, z)$, $PE_{ct_0} = PE_c^m(t) \times f_s^m(t)$.[5] The reference time, t_0: August 4 2011, is the time of the first ^{252}Cf deployment.[68] The reference time is for the stability calibration since the detector response changes with time.[68] After the calibration, the plot of the H-capture energy deviation is represented in Figure 4.5. The total uncertainty of the energy scale is 1.13 %.[5] The energy scale calibration does not include the energy larger

29
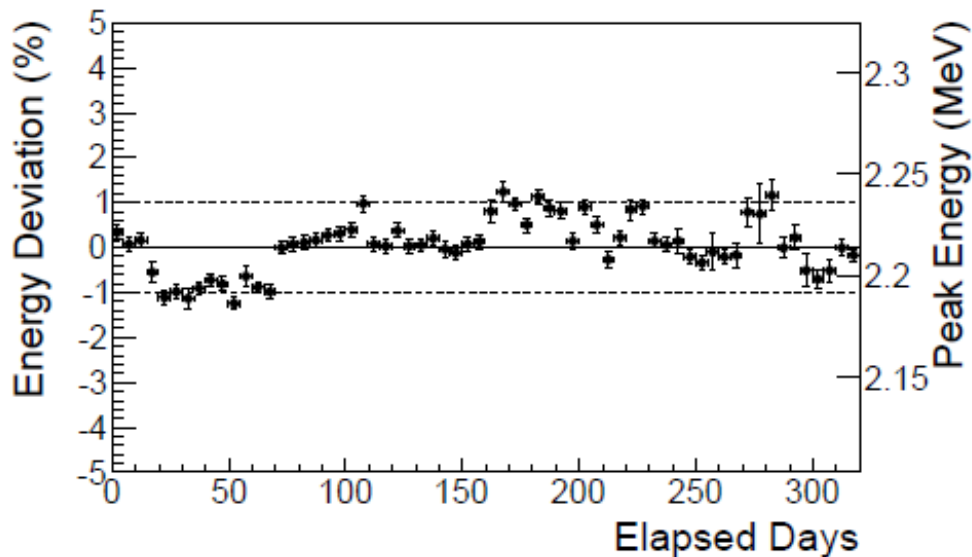
Figure 4.5: The deviation of the H-capture energy position as a function of elapsed day. This plot shows the deviation of the H-capture energy after the energy scale calibration. The systematic uncertainty of the energy calibration, 0.61 % can be estimated by this plot. The plot is from the publication of the Double Chooz Collaboration.[5]

than 12 MeV. In the Chapter 5, the data and the Monte Carlo spectra do not agree with each other in the high energy range because the calibration of the energy reconstruction does not reach to the Gd-capture energy.

4.4   Electronics and Data Acquisition

The diagram of the Double Chooz readout and data acquisition (DAQ) system is shown in Figure 4.6. This system includes the PMT signal reading done by the flash-ADC electronics: the trigger system[69], the High Voltage (HV) splitter, the HV supply, the Front-End electronic (FEE), and the flash-ADC digitizing electronics (ν-FADC)[70,71] in the ID and the IV.[5] Each PMT has $\sim$ 1.3 kV phase cathode bias, and the signal is about 5 mV per PE.[26]
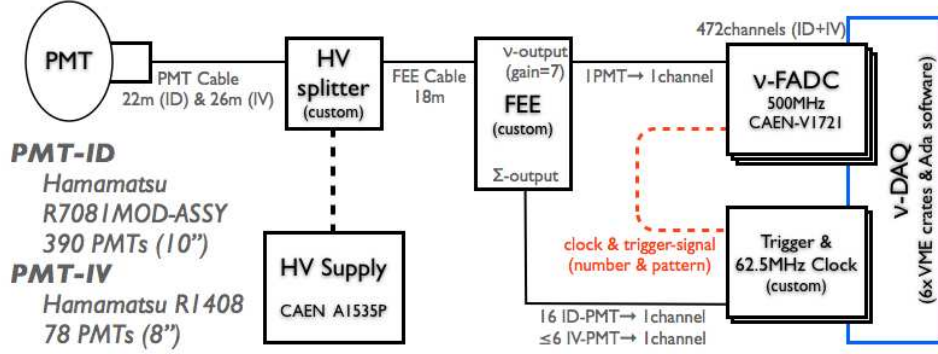
Figure 4.6: The diagram of the Double Chooz readout and data acquisition system. The plot is from the publication of the Double Chooz Collaboration.[5,48]

The signals from PMTs are amplified and shaped by the FEE system. The sum signals from FEE are proportional to charge; these signals are delivered into the trigger system.[69] We acquire waveforms over a time period of 256 ns in the experiment.[69] The FADC can record larger than 90% emitted light from the scintillator in this period of time.[5,69] The threshold of neutrino-like event is set around 350 keV in the ID.[69,72] The trigger efficiency is equal to 100 % when the analysis threshold is above 0.7 MeV (see Figure 4.7).[72]
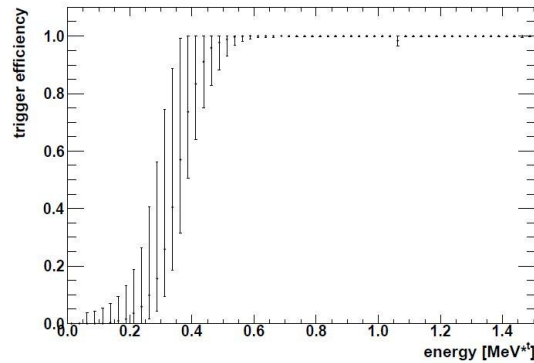
Figure 4.7: The trigger efficiency as a function of E_{vis} of the visible energy threshold. This plot is taken from M. Ishitsuka et. al, "Trigger Efficiency Task Force Report", Double Chooz Document 3261.[73]

The baseline of the FADC shifts with the occurrences of the power-cycling in the laboratory. This variation affects the reconstructed charged estimations. The nonlinearity is shown in Figure 4.3.

The Readout System Simulation (RoSS) simulates the response of the readout systems in the experiment.[5] The simulation is according to measurements of the probability distribution function of single PE from the readout photocathode.[5,26] Each PE striking time of the PMT can be calculated by the Geant4 simulation, and RoSS transfers it into a waveform digitized by the FADCs.[5] Following qualities, gain, baselines, noise etc., each channel is tuned in a predicted experimental condition.

4.5   Pulse and Vertex Reconstruction

A signal time and charge in the PMT can be reconstructed by the pulse reconstruction.[74] The pulse reconstruction is the first step of data reconstruction after RoSS. We apply 1 Hz trigger rate to provide the all channels' information of baseline, and its mean baseline and the rms are calibrated from the 256 ns readout window.[75] The PMT's pedestal is estimated by the integration of the mean baseline in the 256 ns window. After the pedestal is subtracted, the integrated charge (q) is equal to a total count of each waveform. According to the width of PE signal, we set the integral window of the charge integration, 112 ns, to improve the resolution.[75] A dynamic window algorithm is used to find the maximum of integration in the integral window, and the integration is a pulse in the reading window.[75] The start time is calculated at the time when the pulse time reaches to 20% of the maximum.[5] This time can be calibrated by the light inject calibration system.[5,76]

Vertex reconstruction is applied to the energy reconstruction in Double Chooz. A time and charge likelihood algorithm are used to compute the vertex reconstruction. We can assume that each event in the detector is a point source defined as a X function:[5]

$$\mathbf{X} = X(x_0, y_0, z_0, t_0, \Phi). \tag{4.9}$$

In Eq. 4.9, (x_0, y_0, z_0, t_0) indicate the position of event and time, and Φ (photons/sr) is the

flux per unit solid angle. The prediction of the amount of charges detected at i-th PMT is:[5]

$$\mu_i = \Phi \epsilon_i \Omega_i A_i,$$
$$t_i^{(pred)} = t_0 + \frac{r_i}{c_n}. \tag{4.10}$$

In Eq. 4.10, Ω_i is a solid angle observed from the PMT to the event vertex, and r_i is the distance of event to the PMT. ϵ_i and c_n indicate the PMT's quantum efficiency and effective seed of light in the scintillator respectively, and A_i is the transmission amplitude. The likelihood function for each event is defined as:.[5]

$$L(X) = \prod_{q_i=0} f_q(0; \mu_i) \prod_{q_i>0} f_q(q_i; \mu_i) f_t(t_i; ti^{pred}, \mu_i). \tag{4.11}$$

f_q is a probability of charge, q, and the expected charge is μ_i. f_t is the probability of the light arriving the PMT at time t_i, and the predicted arrival time is t_i^{pred}. The best reasonable vertex is the X_{min}, which is located at the maximum of likelihood $L(X)$ or the minimum of $-lnL(X)$. Eq. 4.10 and 4.11 are derived by the Monte Carlo simulation and the positional calibration with the radioactive source, ^{137}Cs, ^{60}Co and ^{68}Ge.[5]

4.6 Light Noise

The accidental flashes from the PMT bases are called a light noise background. This background is from the PMT base, and it is reflected many times by other PMTs' surface. The physical signal can be distinguished from this background by the characteristic of distribution in the detector. The rejection cuts are 1) a Q_{max}/Q_{tot} value and 2) the rms of the start time (t_{start}) of the fist pulse on a PMT.[77] The value ,Q_{tot}, is the total charge collected from a trigger, and Q_{max} is the maximum charge recorded by a PMT. The selection cut is a official cut in the neutrino study. The physical signals are valid for the cuts: 1) $Q_{max}/Q_{tot} < 0.09$ and 2) $rms < 40$ ns. The schemes of light noise and physical events can be seen in Figure 4.8.

(a) The light-noise scheme of prompt signals.

(b) The light-noise scheme of delayed signals.
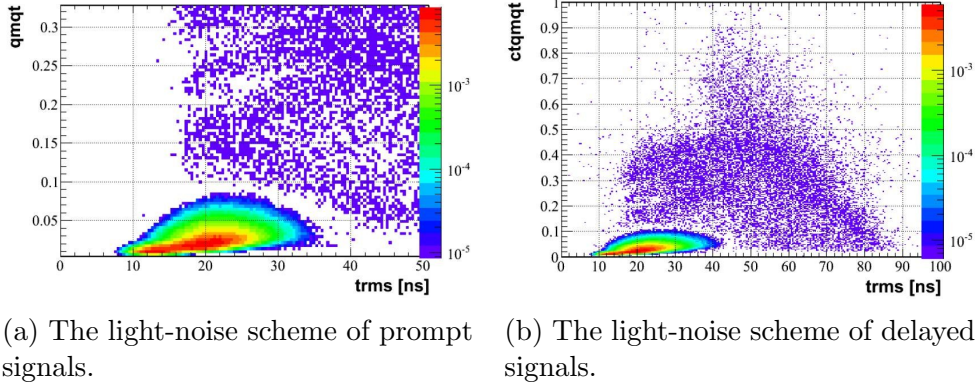
Figure 4.8: The light-noise distributions of prompt and delayed signals respectively, and the physical events are valid for the selection: $Q_{max}/Q_{tot} < 0.09$ and $rms < 40$ ns. These two plots are taken from EU++ Analysis Cluster, "EU++ results for second comparison stage", Double Chooz Document 3199.[77]

4.7 Calibration System

The calibration of Double Chooz uses a light injection system, source deployments, and cosmic rays. The light injection system is used to determine all PMT gains in the detector, time offsets of PMTs, and the PMT stability of their gains and offsets.[76] Source deployments and cosmic rays are used to estimate the detection efficiency of the IBD and the energy scale for gammas, positrons, and neutrons. The light injection system has point-like sources fed by multi-wavelength LED-fiber system (LI). The system injects a known amount of light via optical fibres into the ID and the IV. The LEDs include blue and UV ranges, 285, 425, 470, 365, and 475 nm.[5] The rate, the pulse width, and the light intensity are remotely controlled.

Five radioactive sources, ^{252}Cf, ^{137}Cs, ^{68}Ge, and ^{60}Co, sealed in miniature capsules are used in the source deployment calibration in the NT and the GC.[5] The visible energy is measured from 2.223 MeV gammas from the neutron captures on hydrogen, 1.173 MeV and 1.333 MeV gammas from ^{60}Co, the IBD threshold, a 2×0.511 MeV annihilation from ^{68}Ge, and 0.662 MeV gammas from ^{137}Cs.[5] The sources are deployed into the NT by a motorized pulley-and-weight system from a glove box at the top of the detector chimney.[5] The position resolution is 1 mm, and the lowest position is 1 cm above the bottom of the NT.[5] A rigid

hermetic looped tube with a motor-driven wire (GT) in the GC leads sources from the chimney, attaches to the wall of the NC, reaches the buffer, and leads back to the top of the chimney (see Figure 4.9[78]). The positioning accuracy is $1 \sim 2$ mm in the GT along the

Target volume
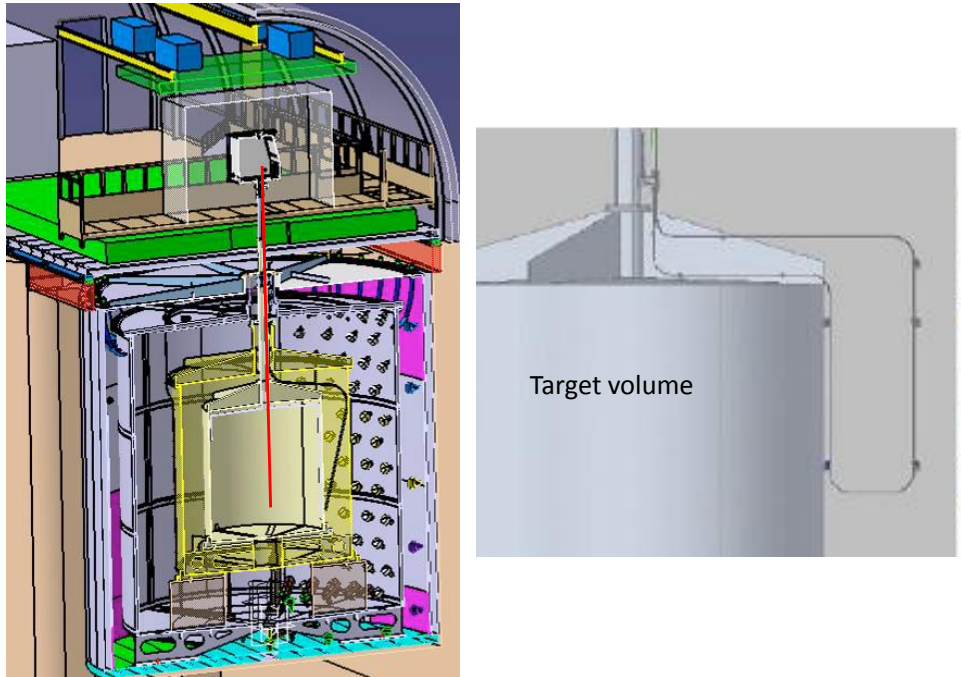
Figure 4.9: Two diagrams show the source deployments in the NT (right): along a z axis indicating a red line from the chimney, and in the GT (left): the gray tube along the NT wall to the buffer.

loop region and the region attached to the NT wall. The radioactivities of the two systems' hardware and the positions can be modeled in the Monte Carlo simulation.

The identified spallation neutrons from cosmic rays are captured by Gd and H in the NT and only captured by H outside the NT. The H-capture peak (2.223MeV) from spallation neutron is used to provide the spatial correction of calibration map in Chapter 4.3. The Gd-capture and H-capture peaks from spallation neutron in the NT and the GC are used to determine the stability of the energy reconstruction (see Figure 4.4 and Figure 4.5).

Chapter 5

Double Chooz Neutron Detection Study with Cf-252

This chapter describes the study of properties of events in which neutrons from ^{252}Cf decay capture on nuclei in the detector. A direct measurement is presented of three quantities which determine the neutron detection efficiency: the Gd-capture fraction, the neutron capture time, and energy containment. The ^{252}Cf neutron capture signals are compared to the IBD neutron capture signals to complete the understanding of neutron detection efficiency.

5.1 Cf-252 Properties

^{252}Cf decay is the sum of 96.9% alpha decay and 3.1% spontaneous fission.[79] Each ^{252}Cf spontaneous fission emits around 3.7 neutrons and 8 gammas.[80] The activity ^{252}Cf, was around 50 Bq in the calibration runs.[5] The spontaneous fission from ^{252}Cf produced a neutron rate, 5.7 events per second (see Eq 5.1), in the calibration runs.

$$5.7 \text{ (neutrons/s)} \simeq 50 \text{ (Bq)} \times 3.1\% \times 3.7 \text{ (neutrons)} \tag{5.1}$$

The average energy of the neutron spectrum is 2.1 MeV, and the average energy of each gamma is 0.87 MeV.[80] The comparisons of the time difference (dT) between the prompt and the delayed signals from ^{252}Cf, and the IBD dT distribution shows a good agreement between the data and the Monte Carol simulation, as shown in Figure 5.1a and 5.1b. Figure 5.2a
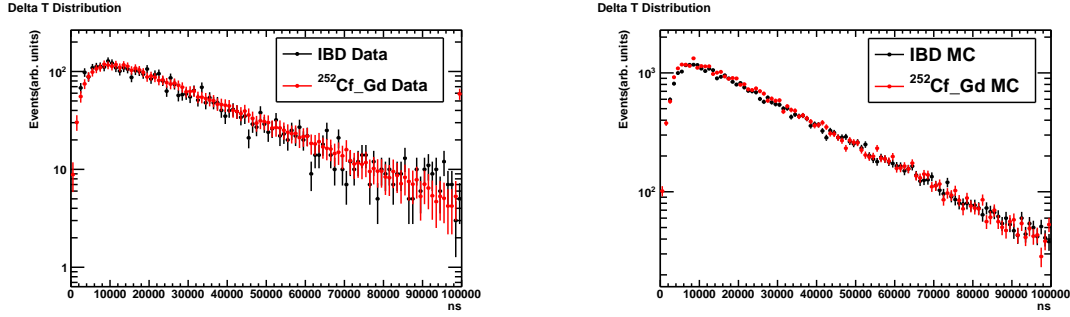
(a) A data comparison of dT between ^{252}Cf and IBD.

(b) A MC comparison of dT between ^{252}Cf and IBD.

Figure 5.1: (a) This is a dT comparison between the data from the ^{252}Cf signals and the IBD signals. (b) This is a dT comparison between the Monte Carlo simulations from the ^{252}Cf signals and the IBD signals.
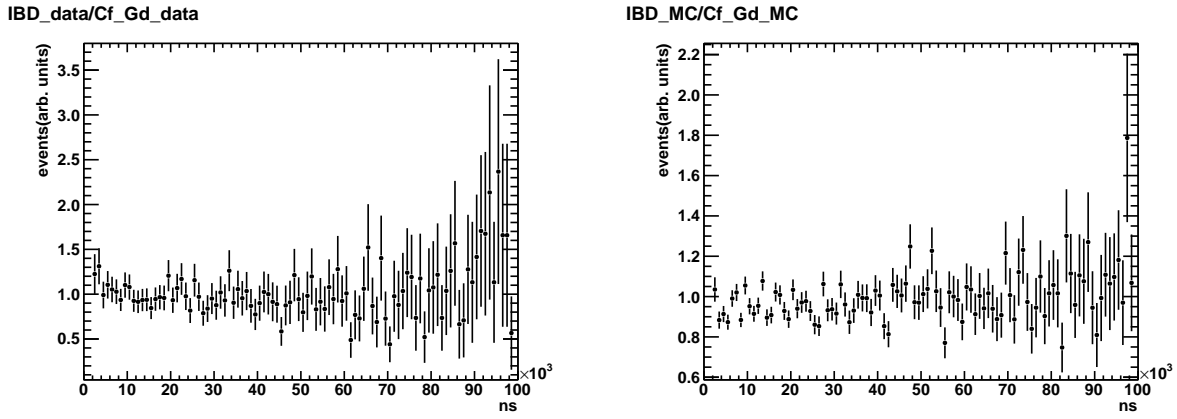
(a) dT ratio of IBD to ^{252}Cf data.

(b) dT ratio of IBD to ^{252}Cf simulation.

Figure 5.2: (a) The data ratio of the IBD signals to the ^{252}Cf signals from Figure 5.1a. (b) The Monte Carlo simulation ratio of the IBD signals to the ^{252}Cf signals from Figure 5.1b.

and 5.2b represent the signal ratio of the IBD to ^{252}Cf. The ^{252}Cf calibration data are used to check the bias between the data and the Monte Carlo simulation, which would increase the systematic uncertainty for the neutron selection criteria of $\overline{\nu_e}$ signals.

5.1.1 Cf-252 Multiplicity

Neutron capture multiplicity is the number of the neutron captures on Gd and H per fission from ^{252}Cf. The experimental and predicted multiplicities of the ^{252}Cf source are shown in

Figure 5.3. The average multiplicity is 3.662 ± 0.008 from the Double Chooz measurement. We can define the efficiency of neutron capture multiplicity as

Multiplicity of total neutron capture (H+Gd)
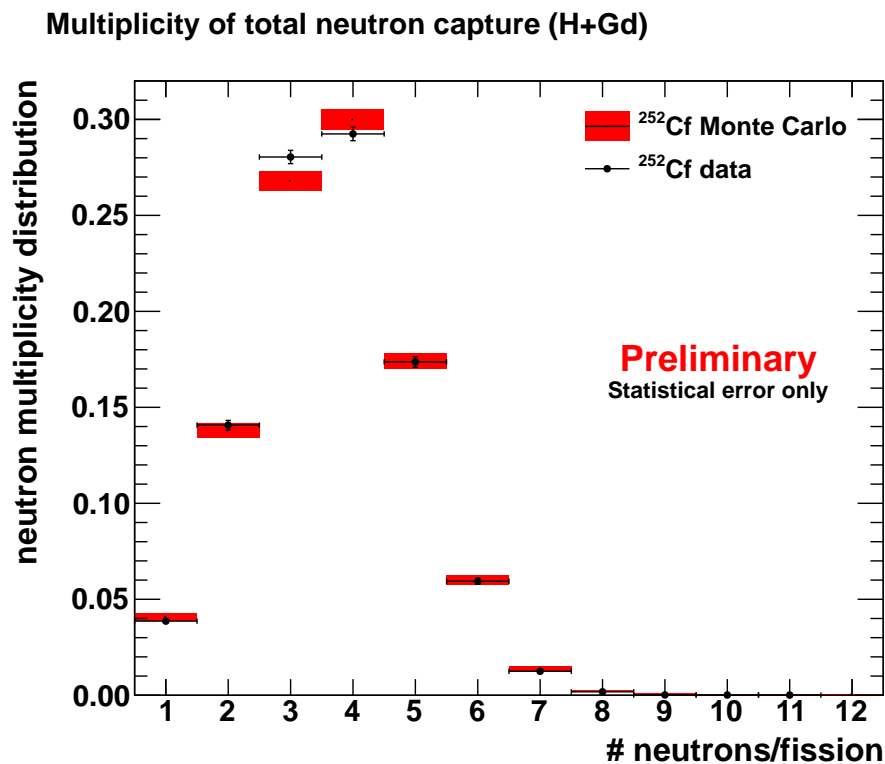
Figure 5.3: The multiplicities of the neutron captures from the measurement and the prediction in the Double Chooz experiment. The black dots are the data, and the black lines with red shadow are the Monte Carlo prediction respectively. The average multiplicity of the data is 3.662 ± 0.008, and the average multiplicity of the Monte Carlo prediction is 3.696 ± 0.013.

$$\varepsilon_m = \frac{N_{n,det}}{N_n}. \tag{5.2}$$

In Eq. 5.2, N_n is the numbers of neutrons, which are emitted from ^{252}Cf, and $N_{n,det}$ is the number of neutron candidates detected from the calibration runs. From Monte Carlo simulation, the average ε_m is equal to $97.99 \pm 0.37\%$, in the NT (see Figure 5.4a). The ε_m along ρ direction in the NT and GC can be seen in Figure 5.4b. Most neutrons in the NT are captured by Gd (about 86% see Chapter 5.2.1). In the GC, neutrons are all captured by H except spill-in phenomenon (see Chapter 5.1.2) near the target boundary, ρ close to
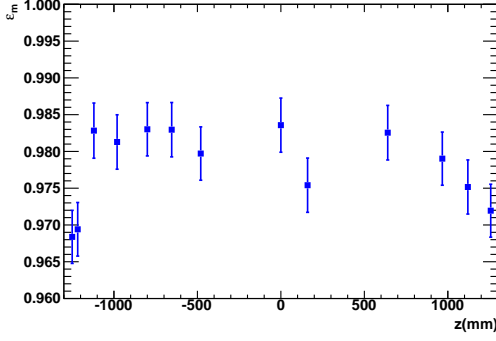
(a) ε_m of ^{252}Cf in the NT.
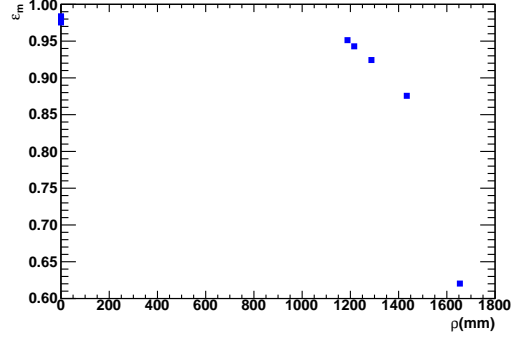
(b) ε_m of ^{252}Cf along the ρ axis.

Figure 5.4: The ε_m results from ^{252}Cf Monte Carlo simulations: (a) along the z axis in the NT, and (b) along ρ axis from the NT to the GC wall. The average ε_m in the NT is equal to $97.99 \pm 0.37\%$. ε_m decreases with ρ direction in the GC because the neutron capture on Gd happens easier than the neutron capture on H in the detector.

1150 mm. From Figure 5.4b, the ε_m in the NT is higher than the ε_m in the GC because the neutron capture by Gd easier happens than the neutron capture on H in the detector.

ε_m is not used in the neutron detection efficiency analysis because the current analysis strategies can not remove the accidental background in the prompt energy range around 0.7 to 3 MeV in measurements. Most accidental events are from the coincidental pairs, which have one prompt and one delayed signals. The coincidental pairs are mixed into the candidates, and they are difficult to distinguish with the real events (multiplicity $= 1$). The phenomenon can easily be observed by the prompt spectrum at each multiplicity. Figure 5.5 is the ^{252}Cf data from the NT center at each multiplicity. The peak is shown around 0.7 to 3 MeV the multiplicity equal to 1 in Figure 5.5a. Comparing with the prompt spectra at other multiplicities, this peak deviates from the expectation. From Figure 5.5b, the prompt spectrum of simulation at the multiplicity equal to one does not show a similar shape as the shape of data at the multiplicity equal 1 shows in Figure 5.5a. Comparing with Figure 5.5b, the peak shown at the multiplicity equal to one is considered to be the background, which cannot be distinguished from the neutron capture selection.

In Figure 5.5a, the background around 0.7 to 3 MeV at the multiplicity equal to one

39
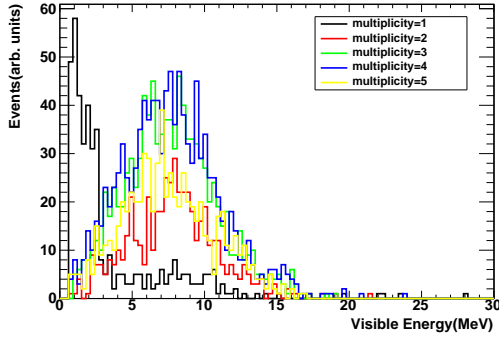
(a) Prompt spectra of ^{252}Cf data.
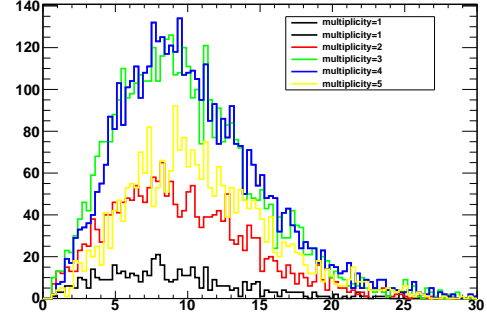
(b) Prompt spectra of ^{252}Cf simulation.

Figure 5.5: Prompt spectra of different multiplicities from the ^{252}Cf data (a) and Monte Carlo simulation (b).

can be removed by more strict light noise cuts; however, this analysis is not included in the recently study. We apply a higher prompt energy (7-30 MeV) cut to remove the background without considering the multiplicity in the efficiency.

5.1.2 Neutron-Capture Spill-In/Out Phenomena

The spill-in/out phenomena happen near the boundary like the wall of the NT. For the spill-in case, the neutrons are produced in the GC and then captured in the NT. The neutron can be captured by H or Gd in the NT; however, the most probable case is that the neutron is captured by Gd. For the spill-out case, the neutrons are produced in the NT and then captured in the GC. The illustration is shown in Figure 5.6. Using to the calibration system, we can investigate the spill-in/out problem in the NT and the GC with the ^{252}Cf source. The spill-in/out efficiency can be estimated with the different applied positions of ^{252}Cf. A detailed discussion follows in the next section.

5.1.3 Neutron-Capture Time in Double Chooz Liquid Scintillators

The neutron-capture time of the Double Chooz liquid scintillator can be estimated by the ^{252}Cf source as well. The capture time can be described by a mathematical function as
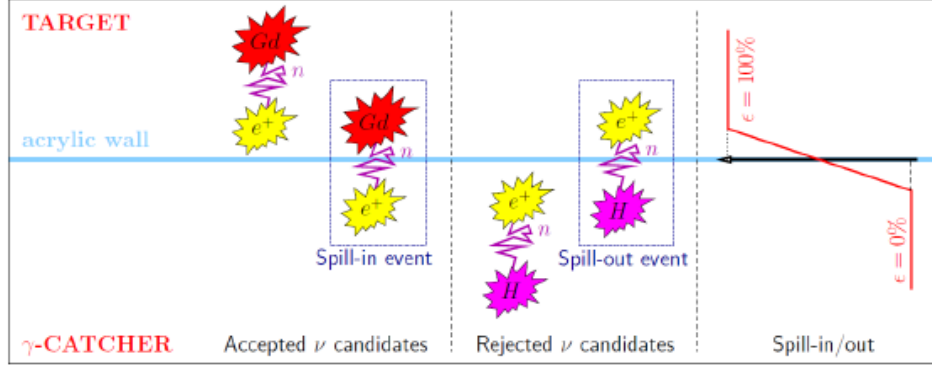
Figure 5.6: An illustration indicates the spill-in/out phenomena. A blue line indicates the NT wall. The neutron is produced in the NT and then captured in the GC (spill-out). The neutron is produced in the GC and captured in the NT (spill-in). The spill-in/out happens near 3-4 cm range of the boundary chemical composition. This plot is from T. Mueller, "Spill-in/out studies", Double Chooz Document 2864.[81]

follows

$$\Delta T(t) = (A - Be^{-\frac{Ct}{n_\tau}})(De^{-\frac{Et}{Gd_\tau}} + Fe^{-\frac{It}{H_\tau}}), \tag{5.3}$$

where A, B, C, D, E, F, and I are constants. Neutron thermalization time can be indicated by n_τ. Gd_τ and H_τ are defined the Gd-capture time and the H-capture time. The neutron capture time is dominated by the geometric position in the detector. According to the deployed position of the ^{252}Cf source, three regions in the detector can be discussed in this section. The first region is near the center of the NT, which is along the z axis at $|z| < 800$ mm. The second region is the boundary near the wall of the NT, and the last region is in the center of the GC. Four illustrations of the dT distribution fitted by Eq. 5.3 are shown in Figure 5.7 (the center of the NT), 5.8 (the boundary of the NT), 5.9 (the boundary of the

41

GC), and 5.10 (the center of the GC). In Figure 5.7 to 5.9, the neutron thermalization is
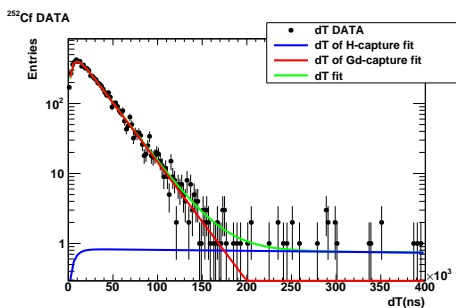
Figure 5.7: dT distribution at the center of the NT (z = 0 mm). The data are black dots. The best fit (green line) is contributed by the neutron captures on Gd (red line) and the neutron captures on H (blue line).
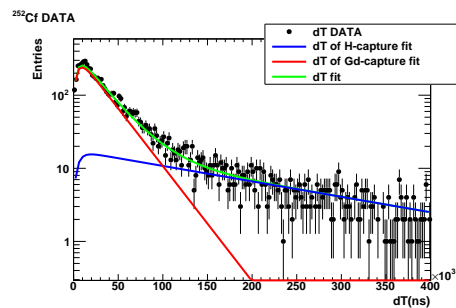
Figure 5.8: dT distribution at the boundary of the NT (z = 1257 mm). The data are black dots. The best fit (green line) is contributed by the neutron captures on Gd (red line) and the neutron captures on H (blue line).
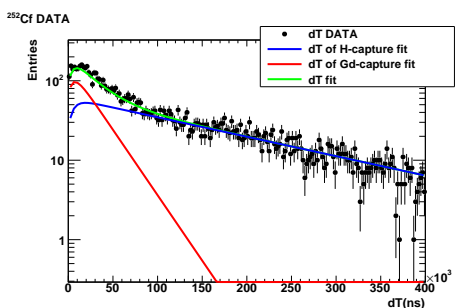
Figure 5.9: dT distribution in the GC near the NT wall (ρ = 1188 mm). The data are black dots. The best fit (green line) is contributed by the neutron captures on Gd (red line) and the neutron captures on H (blue line).
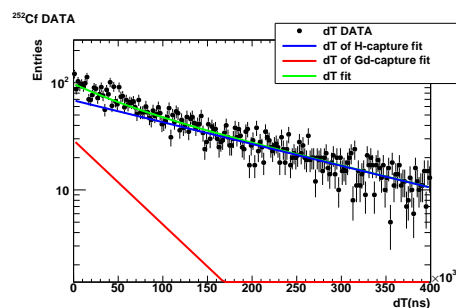
Figure 5.10: dT distribution in center of the GC (ρ = 1287.2 mm). The data are black dots. The fitting result (green line) is contributed by the neutron captures on Gd (red line) and the neutron captures on H (blue line).

around 30 μs. The Gd-capture time can be derived from the best fit (the red line), and the H-capture time can be derived from the best fit (the blue line). In the NT center region, Figure 5.7, the neutron captures on Gd dominate the plot, and the neutron-capture time is around 25 μs. Actually, the neutron- capture time increases with the position closing to the NT wall due to the contribution of the neutron captures on H. In Figure 5.8 and Figure 5.9, the neutron-capture time is around 170 μs due to the increasing contribution of

the neutron captures on H. The spill-in phenomenon can be observed in Figure 5.9 and 5.10 because the neutron captures on Gd are in the GC. The neutron captures on Gd reduce with the increasing distance between the NT wall to the ^{252}Cf source. The cross-sections of the isotopes of Gd have larger values than H in the liquid when the neutron kinetic energy is smaller than 1 MeV (see Figure 5.11). Gd is capable of capturing more neutrons when neutrons have not reached the thermalization (Figure 5.11). Therefore, the thermalization process is more obvious in the NT than in the GC. The range of the neutron thermalization is squeezed with the increasing distance between the NT wall and the ^{252}Cf position in the GC as well.
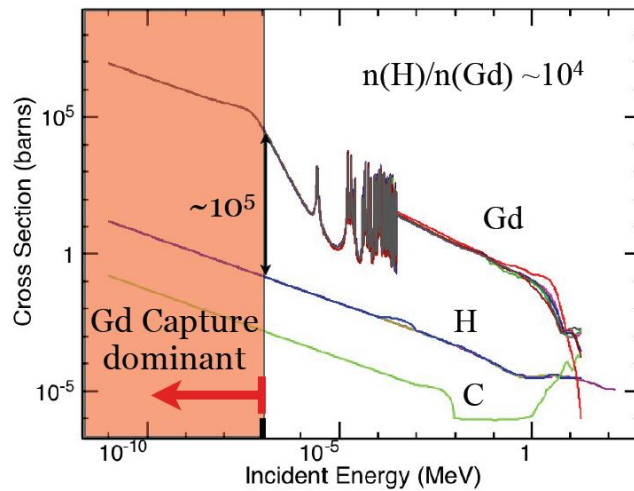
Figure 5.11: Gd isotopes, H, and C cross-sections as the functions of the neutron kinetic energy from A. Hourlier et al., "Neutron Thermalization", Double Chooz Document 4154.[82] The larger Gd cross-section indicates that more neutrons are captured by Gd when neutrons have not reached the thermalization. The Gd-capture is dominant in the Gd-loaded NT due to the larger cross-section.

The Gd-capture time and the neutron thermalization time in the NT are shown in Figure 5.12. The H-capture time in the GC shows in Figure 5.13. The Gd-capture average time is $25.88 \pm 0.12 \ \mu s$ in the NT, and the difference between the data and the Monte Carlo simulation is $5.91 \pm 0.46\%$. The H-capture average time is $197.57 \pm 1.62 \ \mu s$ in the GC,

and the difference between the data and the Monte Carlo simulation is 9.04 ± 0.85%. The average neutron-thermalization time is equal to 5.97 ± 0.13 μs, and the difference between the data and the Monte Carlo simulation is 8.13 ± 2.10%. The large difference of the Gd-capture time can be expected from the difference of the neutron thermalization time of the Monte Carlo neutron thermalization model. This discrepancy can be improved by the time correlation model from A. Hourlier et al.[83] In this study, the time correlation mode is not applied.
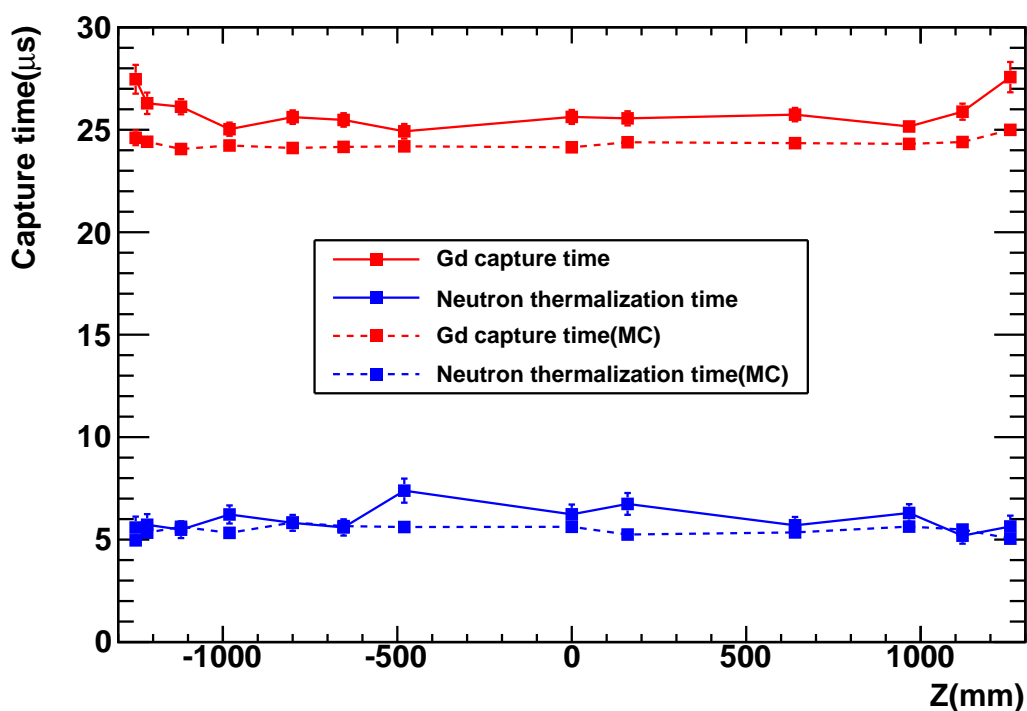
Figure 5.12: The Gd-capture time and the neutron thermalization as the functions of the z axis position in the NT. The dot with a solid line indicates the data, and the dot with a dashed line indicates the Monte Carlo prediction. The average difference of the Gd-capture time is 5.91 ± 0.46% between the data and the Monte Carlo prediction. According to Figure 5.7 and 5.8, the contribution from H is increasing with the z axis, the Gd-capture time raises up near the top and the bottom of the NT. The thermalization time is about $4 - 7\mu s$.
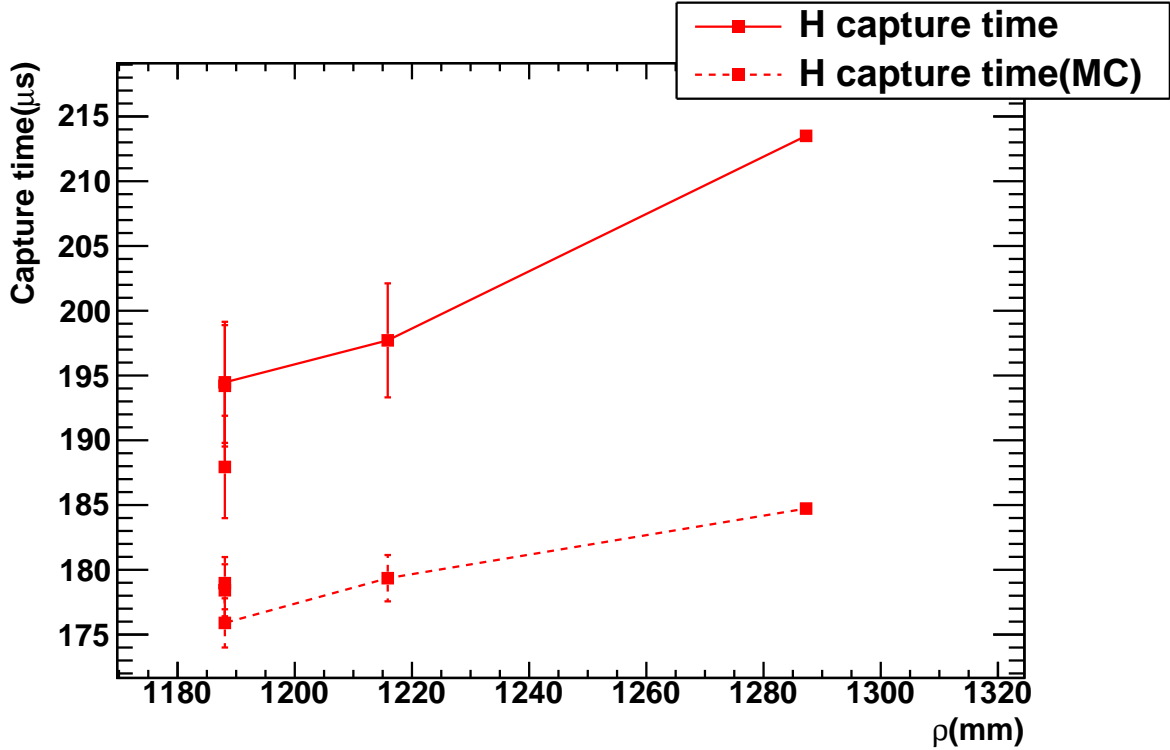
Figure 5.13: H-capture time as a function of the $\rho = \sqrt{x^2 + y^2}$ in the GC. The dot with a solid line indicates the data, and the dot with a dashed line indicates the results from the Monte Carlo prediction.

5.1.4 Cf-252 Neutron Candidate Selection

The neutron candidate selection of ^{252}Cf is similar to the antineutrino candidate's selection.[5] The selection consists of: 1) the energy of the delayed signal from the neutron captures is from 0.7 to 25 MeV, and 2) the trigger is valid for the more strict light noise cuts: $Q_{max}/Q_{tot} < 0.055$ and rms ($t_{start} < 40$ ns). The prompt and delayed spectra are shown in Figure 5.14. In order to select the pure neutron signals, a pre-selection has been applied before the selections: there is no valid trigger before the prompt signal (0.7-30 MeV) in 1 ms. The accidental background can be mixed in the prompt signals. The more strict prompt energy cut (7-30 MeV see Chapter 5.1.1) is used to remove the background.
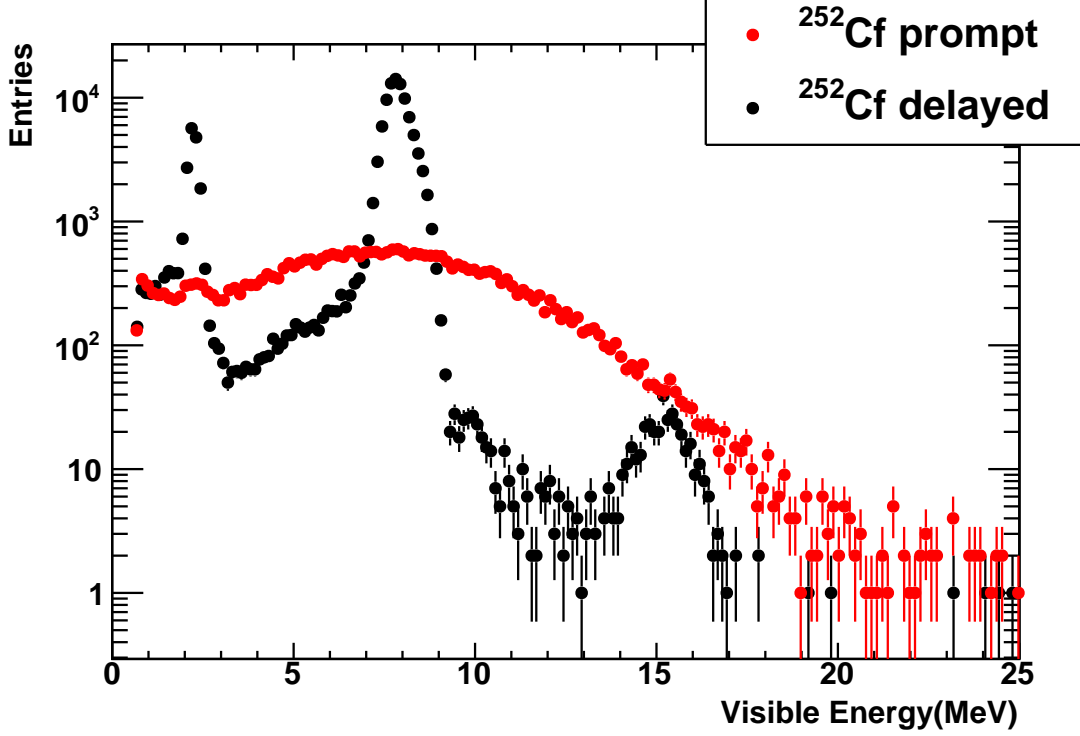
Figure 5.14: This plot shows the spectra of the prompt and delayed signals from ^{252}Cf data.

5.2 Three Factors in the Neutron Detection Efficiency

The neutron detection efficiency in the Double Chooz experiment is the product of factors: 1) the ratio of neutrons captured by Gd (the Gd-capture fraction), 2) the fraction of those neutron captures within the IBD sekectuib time interval, $2\mu s > \Delta T > 100\mu s$, and 3) the fraction of those neutron captures within the IBD energy range, 6 to 12 MeV. A total neutron detection efficiency, $\varepsilon_{neutron}$ from the ^{252}Cf study can be written as Eq. 5.4

$$\varepsilon_{neutron} = \varepsilon_{Gd} \times \varepsilon_{\Delta T} \times \varepsilon_{\Delta E}. \tag{5.4}$$

In Eq. 5.4, ε_{Gd} is an efficiency from the Gd-capture fraction, $\varepsilon_{\Delta T}$ is an efficiency from the IBD desired time interval of the neutron captures, and $\varepsilon_{\Delta E}$ is an efficiency from the energy range, 6-12 MeV.

46

5.2.1 Gd-Capture Fraction

We only consider the Gd-capture and H-capture contributions in Double Chooz neutron detection efficiency. The Gd-capture fraction can be defined as Eq. 5.5.

$$\varepsilon_{Gd} = \frac{N_{Gd}}{N_{Gd} + N_H}. \tag{5.5}$$

N_{Gd} is the total number of the neutron captures on Gd, and N_H is the total number of the neutron captures on H. The whole delayed spectrum from the neutron capture is shown in Figure 5.15 In order to consider the background in the neutron detection efficiency, we have
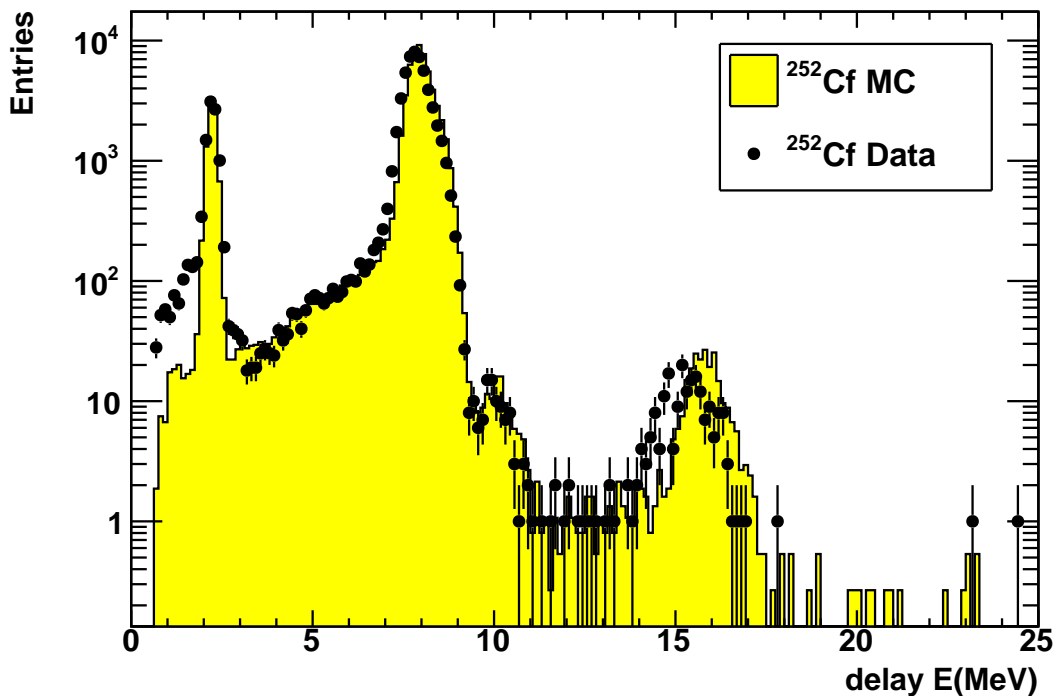
Figure 5.15: The neutron-capture spectrum of ^{252}Cf from 0.7 to 25 Mev. Black dots and solid yellow shaded histogram are the data and the Monte Carlo prediction respectively. The neutron captures on H are around 2.2 MeV, and the neutron captures on Gd are around 8 MeV. A shoulder peak around 10MeV is the signal captured by Gd+H, and a peak around 15 MeV is the signal captured by Gd+Gd. The data and the prediction do not match each other very well due to the energy scale calibration in Chapter 4.3.

fitted the Gd-capture and H-capture areas, rather than simply counting the event numbers

in the energy interval 6 to 12 MeV for the Gd-capture signals and 1 to 3 MeV for the H-capture signals. For doing the spectral fit, we should understand the components of the gamma spectrum generated by the radioactive neutron captures. Two energy regions are contained in the gamma spectrum: 1) the photopeak is the deposited energy of neutron captures, and 2) the continuous spectrum is deposited by Compton scattering.[84] The width of characteristic photopeak is related to the scintillator and the photodetection system, and it is inversely proportional to the detector's resolution.[84] The Compton continue spectrum, which is a small tail in front of the characteristic photopeak is not discriminated from the characteristic photopeak easily in the Double Chooz detector. The two components in the photopeak are separated by a best fit. The discriminated photopeaks are described by several Gaussian distributions, and the Compton continuum spectrum is modeled by a mixed function of an exponential function timing a complementary error function. The width of the Gaussian distribution is from the statistical and electronic noise.[84] The whole gamma spectrum can be described by Eq. 5.6

$$F(x) = Gaussian(x, \sigma, \mu) + B \times e^{Cx} Ercf(\frac{x - D}{E})$$
$$Gaussian(x, \sigma, \mu) = \frac{Area}{\sqrt{2\pi}} e^{-\frac{(x-\mu)^2}{2\sigma^2}}.$$

$$(5.6)$$

Where B, C, D and E are constants in Eq. 5.6. The characteristic photopeaks of two isotopes of ^{155}Gd and ^{157}Gd of the neutron captures are around 8.536 MeV and 7.937 MeV. The described function for the Gd-capture spectrum is presented by Eq. 5.7.

$$F(x) = Gaussian_{155Gd}(x, \sigma, \mu) + Gaussian_{157Gd}(x, \sigma, \mu) + B \times e^{Cx} Ercf(\frac{x - D}{E})$$
$$+ Gaussian_{Gd+Gd}(x, \sigma, \mu).$$

$$(5.7)$$

In Eq. 5.7, the contribution from the Compton scattering is described by only one error function due to the relatively small area of the ^{157}Gd photopeak area and the energy scale calibration range. An additional Gaussian distribution is added into Eq. 5.7 because of the Gd+H-capture signal. The accidental events dominate the capture spectrum below 1 Mev so an exponential decay function is added into Eq. 5.6. The Compton continuum spectrum of

the H-capture spectrum is insignificant compared to the accidental background. The whole spectrum of neutron captures with the best fit are represented by Figure 5.16. Eq. 5.5 can

^{252}Cf Data Delayed Signal
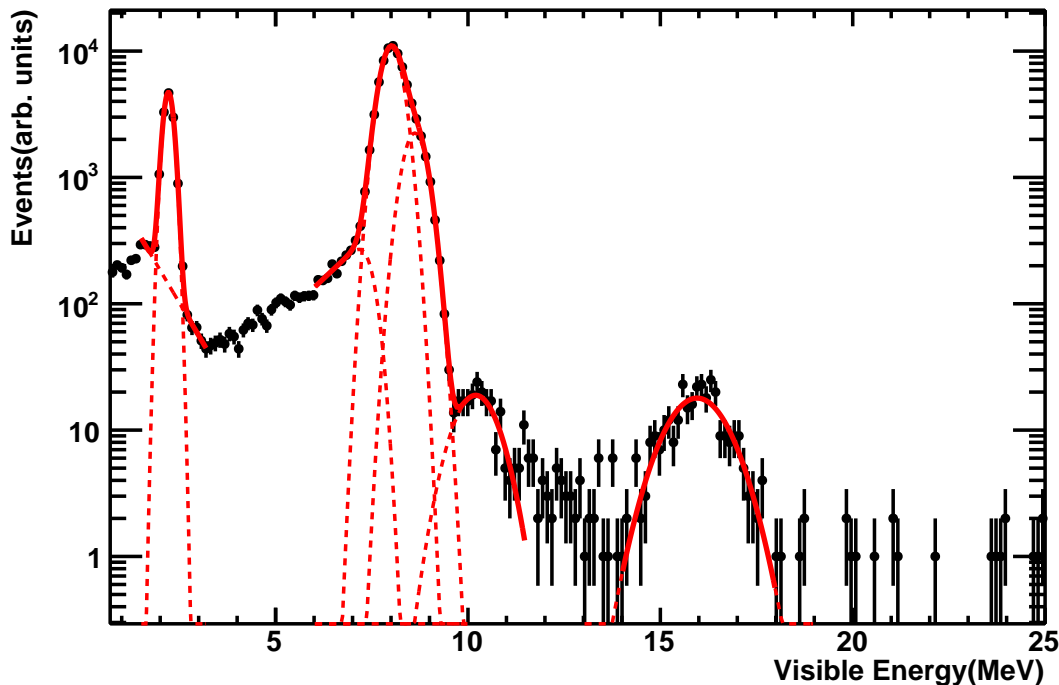
Figure 5.16: The delayed signals from the neutron captures are represented. Black dots and a red curve are the data and the best fit respectively. The H-capture signals are described by an exponential decay and a Gaussian function. The Gd-capture spectrum and the shoulder peak around 10 MeV are described by three Gaussian functions and a error multiplied exponential function. The Gaussian distribution around 15 MeV is the signals captured by Gd+Gd. This plot collected total 2.7 hour run ($|z| <$640 mm) and has 22248 events.

be rewritten replacing event number (N) with the areas of the neutron captures from the best fit as follows:

$$\varepsilon_{Gd} = \frac{Area_{Gd}}{Area_{Gd} + Area_H}. \tag{5.8}$$

In Eq. 5.8, the $Area_H$ is a Gaussian distributions of the neutron captures on H, and the $Area_{Gd}$ is from the area of two Gaussian distributions from the neutron captures on Gd. The Compton continuum spectrum of the Gd-capture spectrum adds another 0.6%. The Gd-capture fraction is stable in the center region of the NT; however, the boundary effect can

49

decrease the Gd-capture fraction when the ^{252}Cf source is closer to the NT wall. The fraction as a function of position along the z axis in the NT is shown in Figure 5.1b. According to a stable Gd-fraction range from Figure 5.16, the average ε_{Gd} fraction is 0.860 ± 0.005. This result is from a spectrum assembled from about 2 hours running time at -640 mm $< z < 640$ mm. The scale factor between the data and the Monte Carlo simulation is $\frac{Data}{MC} = 0.985(\pm 0.3\%)$. The Gd-capture fraction and the relative difference between the data and the Monte Carlo prediction ($\frac{|Gd(H)_{data} - Gd(H)_{MC}|}{Gd(H)_{data}}$) for the NT along the z axis is shown in Figure 5.17 and 5.18 respectively. In the Figure 5.17, the Monte Carlo simulation did
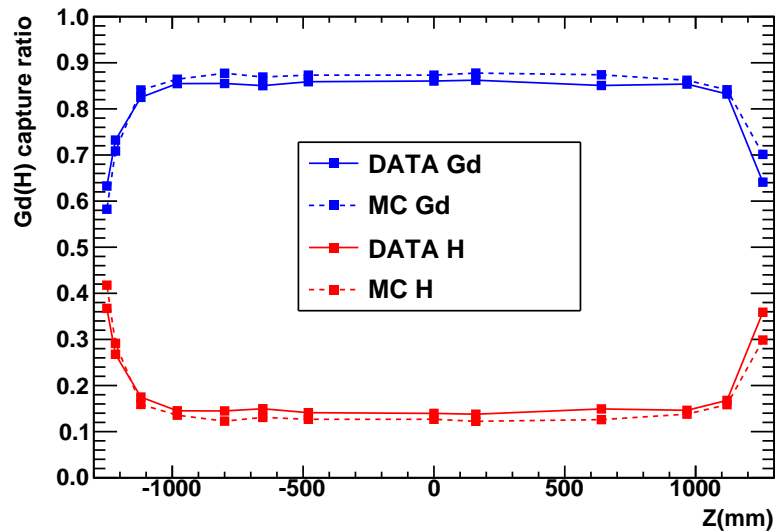
Figure 5.17: The Gd-capture fraction of the data and the Monte Carlo prediction from ^{252}Cf along the z axis in the NT. A blue dot with a solid line and a blue dot with a dashed line are Gd-capture fraction of the data and the Monte Carlo simulation respectively. A red dot with a solid line and a red dot with a dashed line are H fraction ($\frac{Area_H}{Area_{Gd} + Area_H}$) of the data and the Monte Carlo simulation respectively. The Gd-capture fractions have stable values around z from -800 mm to 800 mm; however, the reducing Gd-capture fraction at z > 1000 mm and z < -1000 mm (The NT's height is the z from 1150 mm to -1150 mm.). A boundary effect starts at z > 1000 mm and z < -1000 mm, and the values of the Gd-capture fraction and the H fraction are close to each other near the bottom and the chimney of the NT

a good job at the Gd-capture fractions; however, the increasing differences appear in the boundary region, which is close to the bottom and the chimney of the NT. The higher

50
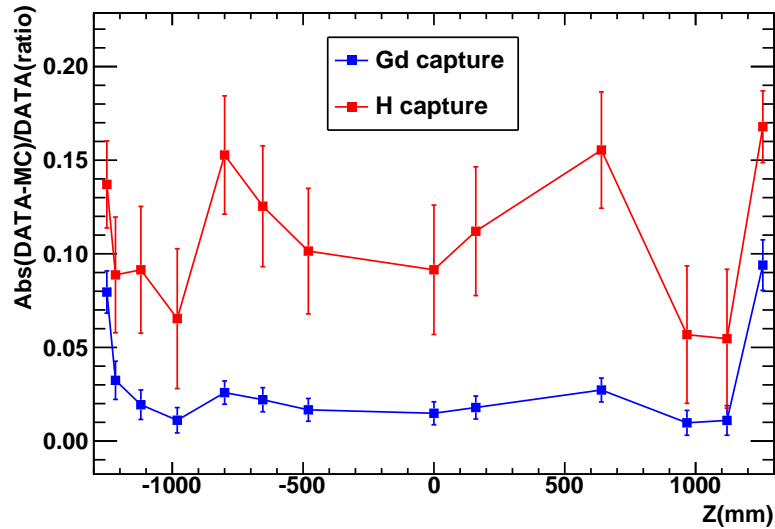
Figure 5.18: The relative difference of the Gd-capture fraction between the data and the Monte Carlo simulation along the z axis. The red dots are the relative differences of the neutron captures on H, and the blue dots are the relative differences of the neutron captures on Gd. The Monte Carlo prediction has a small difference from data for the neutron captures on Gd but a significant difference ($\sim$10 %) for the neutron captures on H.

difference on the H fractions could be due to the lower number of the H-capture event. These differences will be included into the next sections, the dT-efficiency and the energy efficiency.

5.2.2   dT Efficiency

The quantity dT is defined as the time difference between the prompt and the delayed triggers from the neutron captures at 6-12 MeV. The official dT selection is 2 μs < dT < 100 μs. The low dT cute, the excluding events dT < 2.0 μs, has been proposed in the analysis because a strong contamination of light noise is below 2.5 μs shown in Figure 5.19.[77] N(0 μs < dT < 200 μs) is defined as a number of neutron captures in 0 μs < dT< 200 μs. N(0 μs < dT < 200 μs) is a good approximation for Gd captures due to the short neutron capture time. The definition of the dT efficiency, ε_T is

$$\varepsilon_T = \frac{N(2\mu s < dT < 100\mu s)}{N(0\mu s < dT < 200\mu s)}. \tag{5.9}$$
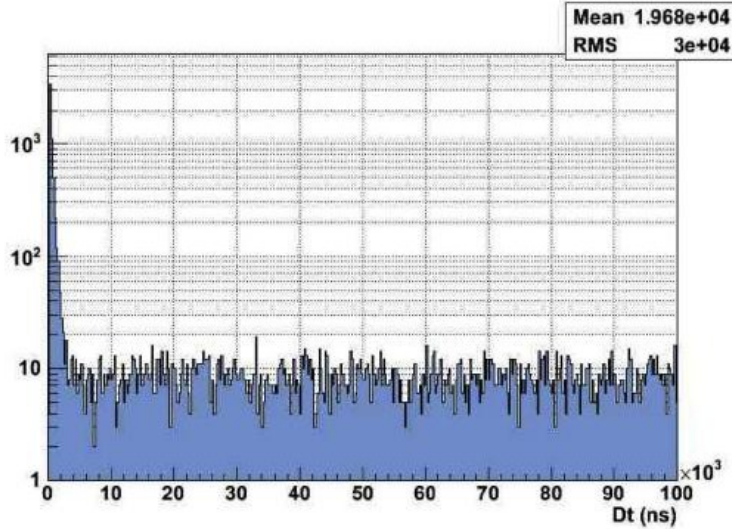
Figure 5.19: dT distribution of the light noise sample. This plot is from Double Chooz EU++ Cluster, "EU++ results for second comparison stage", Double Chooz Document 3199.[77]

Figure 5.20 shows the dT (prompt-delayed) distribution of the neutron captures from the ^{252}Cf source deployed at several positions around the target center. The data and Monte Carlo waveforms are consistent according to Figure 5.20. The dT efficiencies along the z axis of the NT are shown in Figure 5.21, and the relative differences as a function of z axis of the NT between the data and the Monte Carlo prediction can be seen in Figure 5.22.

The detailed discrepancy along the z axis of the NT can be observed in Figure 5.21 and 5.22. In Figure 5.21, the boundary effect, which decreases the dT efficiencies, is similar to Figure 5.17. It can be observed in Figure 5.22 that the larger differences are located at the boundary. The average dT efficiency of the NT can be integrated along the z axis from Figure 5.21 The average efficiencies for data and Monte Carlo prediction are 0.9646 ± 0.0023 and 0.9691 ± 0.0010 respectively. The average relative difference between data and Monte
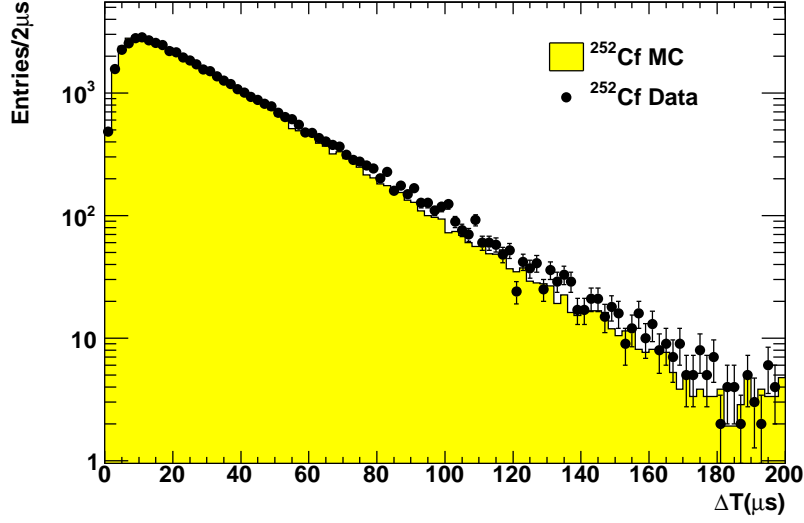
Figure 5.20: The dT distributions of the data and the Monte Carlo prediction at the delayed energy interval, 6-12 MeV, show by black dots (data) and yellow shadow (Monte Carlo) histogram respectively. The neutron thermalization time can be observed at $\Delta T < 20\mu s$.

Carlo prediction is $0.47 \pm 0.26\%$. Additionally, the dT efficiency must take into account the GC contribution as a function of $\rho = \sqrt{x^2 + y^2}$, as shown in Figure 5.23. The final dT efficiency is determined by an extrapolation from the Z-axis system to the GT system weighted by the Gd-capture fractions from the Monte Carlo prediction. We construct a $f(\rho)$ function to describe the data and the Monte Carlo prediction.

The systematic error is defined by the integrated differences of the data and the Monte Carlo prediction in the cylindrical coordinates. According to Figure 5.23, the function can be defined as Eq. 5.10 to describe the data and the Monte Carlo simulation.

$$f(x) = A - B \times \tanh(\frac{z - C}{D}). \tag{5.10}$$

In Eq. 5.10, A, B, C, and D are constants. The difference of the two integrations (the data and the Monte Carlo curves) from Eq. 5.10 is 0.13 % ($\rho = 0$ to 1150 mm). The final dT efficiency systematic error of the data is equal to the combined error from the differences of the extrapolation from Z-axis to the guide tube and the error of averaged dT efficiency along the Z-axis, $0.4 \sim 0.5\%$.

Figure 5.21: dT efficiency as a function of position along the z axis of the NT. Red dots indicate the Monte Carlo prediction, and blue dots indicate the data. The boundary effect is seen near the top and bottom of the NT where efficiency is reduced. The averaged efficiencies integrated along the z axis in the NT are 0.9646 ± 0.0023 from the data and 0.9691 ± 0.0010 from the Monte Carlo simulation.

5.2.3 Energy Containment Efficiency

N(6-12 MeV) is defined as a number of neutron captures within energy range, 6-12 MeV. The energy containment efficiency is defined as Eq. 5.11.

$$\varepsilon_{\Delta E} = \frac{N(6 - 12 MeV)}{N(4 - 12 MeV)}. \tag{5.11}$$

The energy containment efficiencies of the data and the Monte Carlo prediction are shown in Figure 5.15. Only in the energy scale calibration range ($<$ 12 MeV), the Monte Carlo simulation agrees with the data. The background events concentrate in the range in 0.7 to 3 MeV, as mentioned in the Gd-capture fraction section; however, the energy containment efficiency does not include this range. Figure 5.24 shows the energy containment efficiencies along the z axis of the NT, and the relative differences of the efficiencies between the data and the Monte Carlo predictions as the functions of the z axis of the NT is shown in Figure 5.25.

The efficiency decrease near the top and the bottom of the NT is similar to Figure 5.17
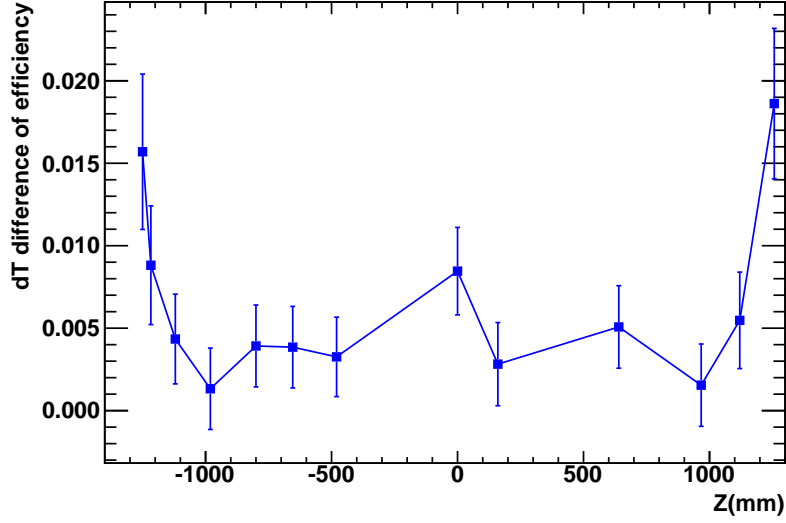
Figure 5.22: Differences of dT efficiency between the data and the Monte Carlo predictions as a function of position along the z axis of the NT. The higher differences is around the boundary of the NT. The average difference is equal to 0.47 ± 0.26 %.

and 5.21. The average efficiency can be obtained by integration along the z axis with the result 0.9643 ± 0.0022 for the data and 0.9697 ± 0.0009 for the Monte Carlo prediction. We use the extrapolation in section 7.3.2 to weight the efficiencies by the Gd-capture fractions of the Monte Carlo prediction from the z axis in the NT to the GC. The energy containment efficiency from the NT to the GC is shown in Figure 5.26. The final systematics error of the energy containment is equal to the combined error from the difference of the extrapolation from the Z-axis system to the GT system and the error of averaged energy containment efficiency along the z axis, 0.6~0.7%.

5.2.4 Neutron Detection Efficiency Systematics from Cf-252

According to the previous three sections, we can summarize the systematic uncertainties, which are estimated with the ^{252}Cf neutron analysis. The final results of the neutron detection systematic uncertainties are shown in Table 5.1. The total systematics uncertainty estimated by ^{252}Cf is 0.91%. The efficiency and the uncertainty were put into the detection efficiency uncertainty of the neutrino oscillation analysis. The total Monte Carlo scale
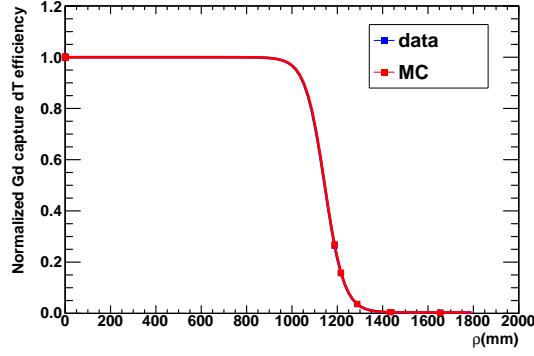
Figure 5.23: The extrapolation from the NT center (z = 0) to the GT is considered in the dT efficiencies of the data (blue) and the Monte Carl predictions (red). The differences of the area integrations between the data and the Monte Carlo prediction are 0.13%(interval [0, 1150] mm) and 0.2%(interval [0, 1435] mm).

Table 5.1: Summary of neutron efciency systematics uncertainties from ^{252}Cf

Parameter	Systematics uncertainty	Monte Carlo scale factor
Gd-fraction correction and systematics	0.3 %	0.985
dT-efficiency systematics	0.5 %	1
E-containment-efficiency systematics	0.7 %	1
total systematics	0.91%	0.985

factor is 0.985 contributed by Gd-fraction mainly (see Chapter 5.2.1). The Monte Carlo scale factor is used to scale the Monte Carlo predictions of IBD and background. The scaled predicted spectra is use to compare with the IBD data by rate or spectral shape in the final oscillation analysis. The high discrepancy between data and Monte Carlo prediction is observed near the top and the bottom of the NT from Figure 5.18 for Gd-capture fraction[1], 5.22, and 5.25. The acrylic walls reflect light to affect the time correlation of the signals. Reflection produced from acrylic walls affects the detected event numbers as well. Due to these complex optical properties, which cannot easily be modeled in the recent Model Carlo simulation exactly near the boundary of the NT wall. Therefore, the Monte Carlo prediction is inefficiency near the top and bottom of the NT wall. In order to make a

---

[1]For H-capture fraction, the low statistics of data causes the relative differences with high errors. Therefore, the high discrepancy near the bottom and top of the NT cannot show in the H-capture fraction.
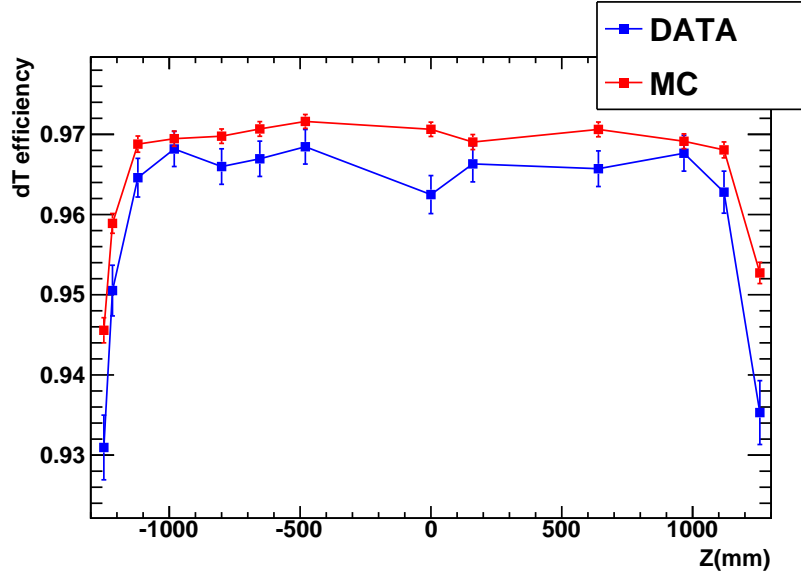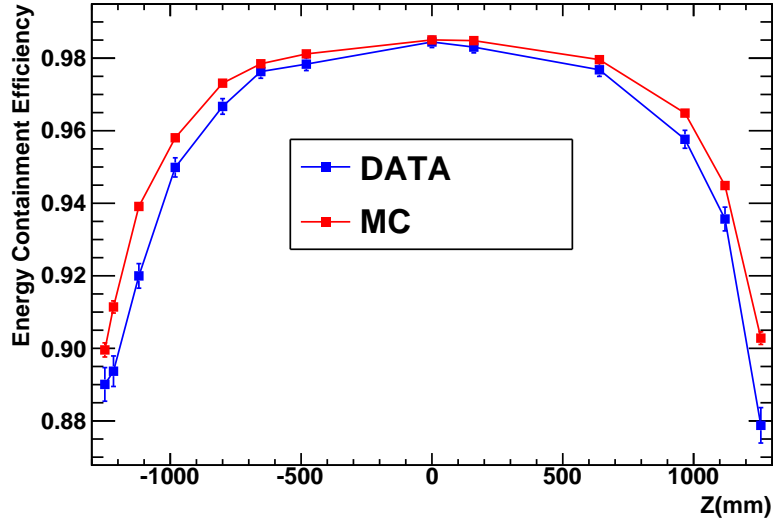
Figure 5.24: The energy containment efficiency as a function of position along the z axis in the NT. Red dots indiate the Monte Carlo prediction, and blue dots indiate the data. The energy containment efficiencies near the top and the bottom of the NT show the decreased efficiencies. The average efficiencies along the z axis in the NT are 0.9643 ± 0.0022 for the data and 0.9697 ± 0.0009 for the Monte Carlo prediction.

complete efficiency of the whole ID, we estimate the efficiency from the extrapolation from the NT to the GC and the bias of the z axis in the NT. This study considers the Monte Carlo uncertainty, scale factors and the boundary effect in the liquid detector comprehensively.

5.3 Gd-Capture Fraction and Spill-In/ Out from Cf-252

Building upon the previous section, the weight by the Gd-capture fraction in the extrapolation from the NT to the GC is introduced in this section. From the extrapolation study, we only consider the data points in the stable Gd-capture fraction stability range in the NT $|z| = 0 - 640$ mm (Figure 5.17). The same analysis of Figure 5.17 can be applied to whole NT data along z axis and the GT system data in the GC. The normalized Gd-capture fractions as a function of positions along ρ in the GC, and as a function of position along the z in the NT are shown in Figure 5.27a and 5.27b respectively. The weight values are from
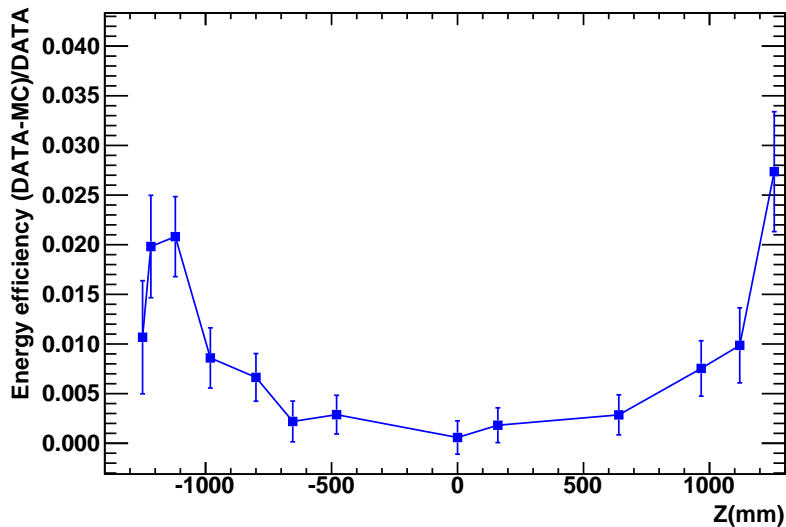
Figure 5.25: The relative difference between the data and the Monte Carl prediction as the functions of the z axis in the NT. The average relative difference is $0.58 \pm 0.25\%$.

the Gd-capture fractions normalized by the average Gd-capture fraction, $|z| < 640$ mm, in the NT. Due to the calibration equipment orientation, the data from the GT system are represented with the ρ direction, and the data from the NT are represented with the z axis.

The spill-in/out phenomena can be demonstrated by the Monte Carlo prediction easily. Several million neutrons have been generated in the NT including the chimney and in the GC. Building upon Chapter 5.1.2, the spill-in/out phenomena can be determined by the initial vertex of neutron origin and position of neutron captures in the Monte Carlo prediction. The neutron detection efficiency of Monte Carlo prediction is shown in Figure 5.28. The neutron efficiencies are not all equal to one in the NT because of the spill-out phenomenon. The efficiency drops about 57% on the acrylic wall of the NT. For the GC, the efficiencies are not all equal to zero, and they increase near the NT wall because of the spill-in phenomenon.

In the Monte Carlo prediction, the neutron origin and capture positions can be easily identified; however, experimentally it is impossible to find out the real neutron origin. In

58
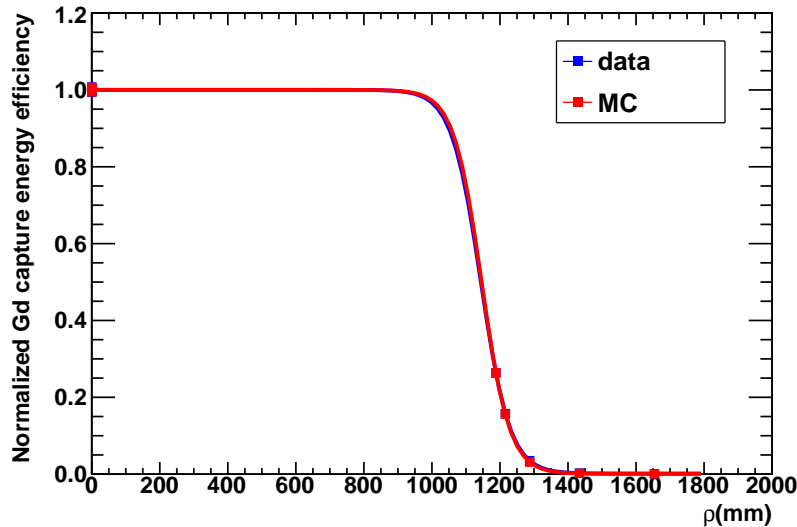
Figure 5.26: The extrapolation of the energy containment efficiency from the NT center (z = 0) to the GC are plotted for the data (blue) and the Monte Carlo prediction (red). The difference of the two area integrations between the data and the Monte Carlo curves is 0.4% (0-1150 mm) and 0.31% (0-1435 mm).

order to make a perfect theoretical demonstration closely, we can generate neutrons uniformly in the NT and the GC, and we can provide the detection efficiency as a function of the distance between the neutron to the wall. Unfortunately, this plan is limited by the calibration equipment orientation. The approximate estimation should be modified according to the conditions of two source deployments (z-axis and GT systems) in the detector. For the data measured in the NT, we describe the position along the z axis (see Figure 5.27b). For the data measured in the GC, we describe the position along the ρ axis and ignore the z axis (see Figure 5.27a). We only can judge the spill-in/out phenomena by the Gd-capture fractions because the neutron captures on H can happen both in the NT and the GC. The neutron captures on Gd only happen in the NT. According to the deployed positions of ^{252}Cf, assuming that it is equal to the positions of the neutron captures on Gd, the spill-in/out ratio can be estimated by the efficiencies of the Gd-capture fractions. We assume that the Gd-capture efficiency is 100% at center of the NT; then, we can weight the Gd-capture fractions by the center Gd-capture fraction similar to the extrapolation study.
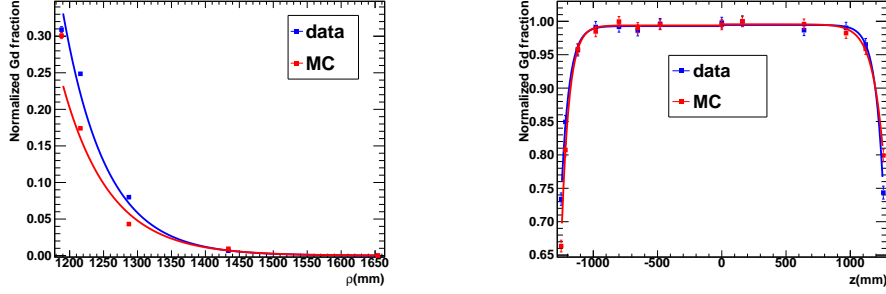
(a) Normalized Gd-capture fraction in the guide tube.

(b) Normalized Gd-capture fraction in the NT.

Figure 5.27: (a) Normalized Gd-capture fractions in the GT system. Blue dots indicate the data, and red dots indicate the Monte Carlo predictions. Each Gd-capture fraction is normalized by the average Gd-capture fraction ($|z| < 640$ mm) in the NT. (b) Normalized Gd-capture fractions in the NT. Blue dots indicate the data, and red dots indicate the Monte Carlo predictions. Each Gd-capture fraction is normalized by the average Gd-capture fraction ($|z| < 640$ mm) in the NT.

The efficiency of Gd-capture fraction in the whole NT can be estimated by the integration along the z axis in Figure 5.27b. If there is no spill-out phenomena, the total efficiency of Gd-capture fraction is equal to 100%× Z (the hight of the NT). The spill-out study can be evaluated roughly by the missed area equal to $100\% \times Z$ subtracting the area under the curves in Figure 5.27b. The formula is defined as Eq. 5.12.

$$f(z) = \int_{z_0}^{z} (1 - e^{B+Cz}) dz.$$ (5.12)

In Eq. 5.12, B and C are constants. The intervals of Eq. 5.12 are [0 mm, 1257mm], $z_0 = 0$ to the top of the NT, and [-1250 mm, 0], the bottom of NT to $z_0 = 0$. We do not consider the chimney effect in this study. Since the Gd-capture efficiencies should be zero in the GC without the spill-in, the spill-in can be evaluated roughly by the area of the curve of Gd-capture fraction in Figure 5.27a. The formula is defined as Eq. 5.13.

$$f(\rho) = \int_{\rho_0}^{\rho} e^{D+E\rho} d\rho$$ (5.13)

In Eq. 5.13, D and E are constants. The interval of Eq. 5.13 is [1158 mm, 1708 mm], the NT radius + the vessel thickness to the GC radius. The ratios of the spill-in/out are shown
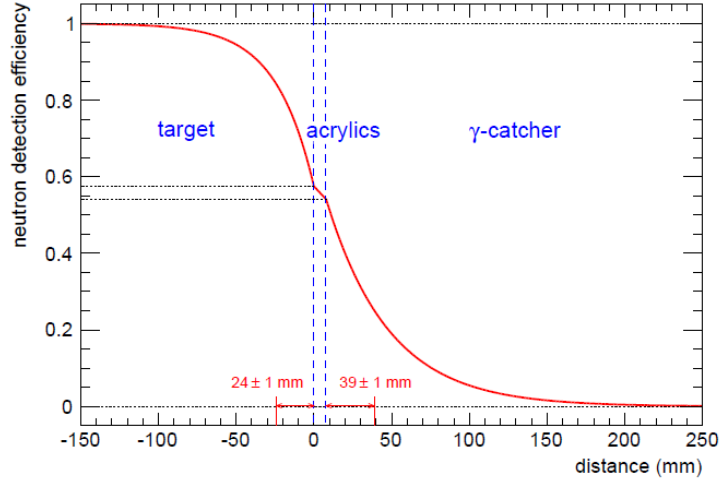
Figure 5.28: The neutron detection efficiency as a function of the distance between the neutron source and the acrylic wall. This plot is from Th. A. Mueller, " spill-in/out studies and other interesting stuff about neutron physics", Double Chooz Document 3031.[85] This plot illustrates the spill-in/out phenomena observed from the neutron detection efficiencies as a function of the distance between the neutron source and acrylic wall.

Table 5.2: Summary of spill-in/out from ^{252}Cf

in/out	spill-out	spill-in
data	$1.26918 \pm 0.0852652\%$	$4.02867 \pm 0.864312\%$
MC	$1.4452 \pm 0.183363\%$	$4.42249 \pm 0.573181\%$
differency	$13.86 \pm 15.96\%$	$9.77 \pm 25.82\%$

in Table 5.2. The spill-out ratio, $1.44 \pm 0.18\%$, from the Monte Carlo prediction consists with the Double Chooz second publication result (from the Monte Carlo prediction), $1.35 \pm 0.04\%$(stat)[5]. This study gives a strong proof to support the correction of the Monte Carlo mode in the Double Chooz experiment. The improvement can increase with more measurements in the NT and in the GC to reduce the statistic error of the experimental spill-in/out ratio.

61

5.4 Gd-Capture Fraction Estimated by Inverse Beta Decay (IBD)

5.4.1 Vertex Cut

Using ^{252}Cf to estimate the neutron detection efficiency for IBD still has some worries because the neutrons from ^{252}Cf have higher energy than the real IBD neutron distribution. However, it is hard to evaluate all efficiencies by the IBD events due to the low observed rate, 30 events/day; we can try to evaluate the Gd-capture fraction of IBD events skillfully. The Gd-capture fraction result can test whether the result from ^{252}Cf agrees with the IBD's result. In the previous section, we consider the ^{252}Cf applied positions in the range -640 mm $< z <$ 640 mm. For the IBD case, the vertex of the neutrino should be limited in the NT, and the produced neutrons must be captured in the NT too. However, the spatial resolution is around 32 cm[5] in the NT, the vertex reconstruction of the prompt and the delayed signals should be checked by the true information of the Monte Carlo simulation again. In the IBD process, the true vertexes contain the initial vertexes of the primary particles, and the scintillation light vertexes. Since the positrons are produced instantly in the IBD reaction, the neutrino's vertex is close to the positron's vertex. Figure 5.29 shows the positron correlation between the vertex reconstruction and the true vertex from the truth information of the Monte Carlo simulation. Figure 5.29 shows a very good agreement between the positron vertex reconstruction and the true information because of the small sigma values of the two dimensional Gaussian distributions. The vertex reconstruction is calculated from the gamma rays produced from the positron annihilations in the detector. The annihilation should happen immediately after the positrons produced. We can easily assume the positron vertex reconstruction as the neutrino vertex. The correction between the vertex reconstruction of the neutron captures on H and on Gd and the true vertex are shown in Figure 5.30 and 5.31. The two dimensional plots of the neutron captures have wilder σ distributions because the neutrons can propagate the longer distance than the positron did in the detector. However, the H-capture case has a wilder distribution than
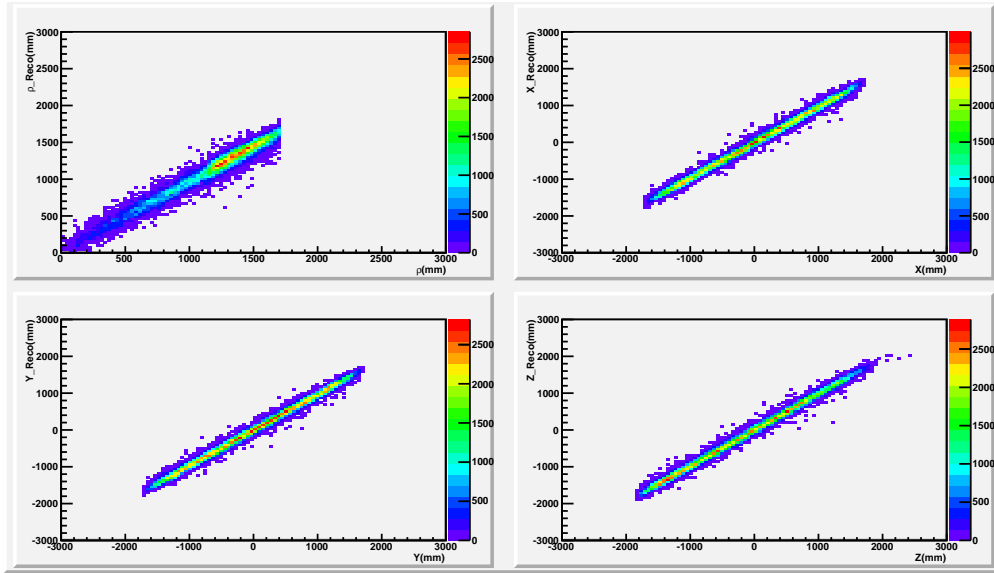
Figure 5.29: The correlation between the positron vertex reconstruction and the true vertex from the Monte Carlo information. Four plots show the vertex reconstruction as the functions of ρ, X, Y, and Z of the truth positron vertex from the Monte Carlo prediction. A small sigma of a two dimensional Gaussian distribution indicates that the vertex reconstruction agrees with truth vertex very well in the positron case.

the Gd case's distribution. This result could an effect caused by the energy and vertex reconstruction.

On the other hand, the Gd-capture fraction can also be calculated by the initial deposited energy from a particle true information since we have the Monte Carlo true information. An illustration is shown in Figure 5.32 from the ^{252}Cf Monte Carlo prediction. In Figure 5.32, a red curve indicates the initial deposited energy spectrum, and the energy reconstruction is a black curve. The Gd-capture fraction can easily be counted by the event numbers in Figure 5.32. The theoretical initial deposited energy ranges are defined: Gd-capture, 7.5-9 MeV, and H-capture, 2-2.4 MeV. The Gd-capture fraction from the ^{252}Cf Monte Carlo initial deposited energy is equal to 0.885 ± 0.002 and the Monte Carlo scale factor is 0.97 ± 0.006 from the Monte Carlo initial deposited energy.

The Gd-capture fraction provided from the neutrino events is shown by the initial deposited energy from the Monte Carlo prediction. Several million neutrinos are generated in
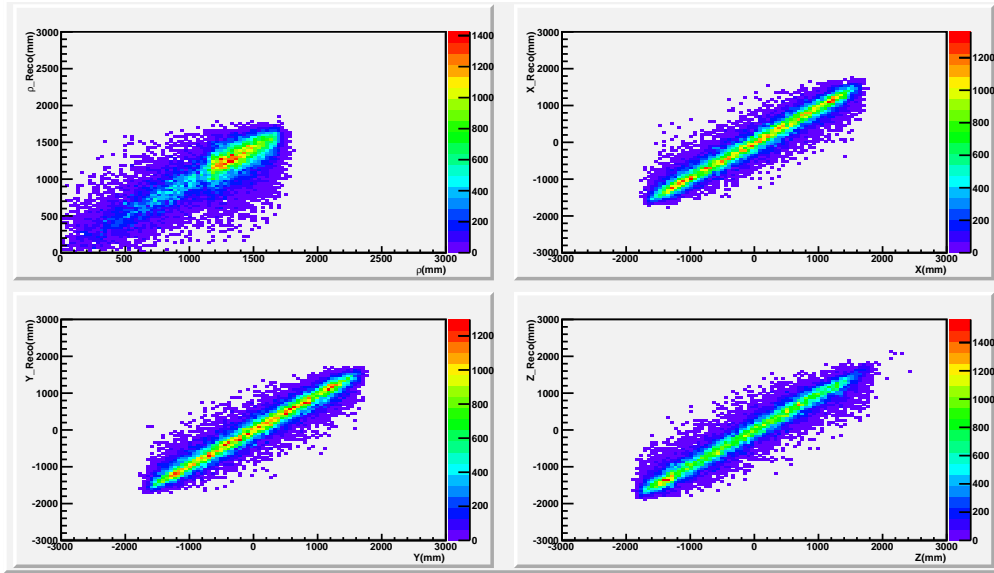
Figure 5.30: The correlation between the vertex reconstruction of the neutron capture on H and the true vertex from the Monte Carlo information. Four plots show the vertex reconstruction as the functions of ρ, X, Y and Z of the truth positron vertex from the Monte Carlo prediction.

the NT and the GC uniformly. According to the cylindrical symmetry of the detector, we consider two vertex cuts to define a smaller cylinder inside the NT. The prompt vertex reconstruction of neutrino candidates should be in this smaller cylinder. The vertex selection is applied at the ρ direction and the z direction. The small cylinder volume is limited to the vertex selection by the value, *Reco-vertex*: 1) $|z| <$ *Reco-vertex* mm, and 2) $\rho <$ *Reco-vertex* mm. Figure 5.33 from the Monte Carlo prediction shows the Gd-capture fraction from the neutrino events according to the initial deposited energy as a function of *Reco-vertex*. A stable Gd-capture fraction, 0.88, exists in *Reco-vertex* < 900 mm. Reducing Gd-capture fractions shows that the spill-in/out effect affects the Gd-capture fraction at *Reco-vertex* $\sim$ 900 mm. Before the spill in/out happens, *Reco-vertex* < 900 mm, we are confident that the candidates of the IBD are all in the NT. The Gd-capture fraction is contributed by the neutron captures in the NT. The stable Gd-capture fraction (from the initial deposited energy of the Monte Carlo prediction), 0.886 ± 0.003, at *Reco-vertex* < 900 mm is very close to the result of ^{252}Cf, 0.885 ± 0.002 (from the initial energy of the Monte Carlo prediction).

64
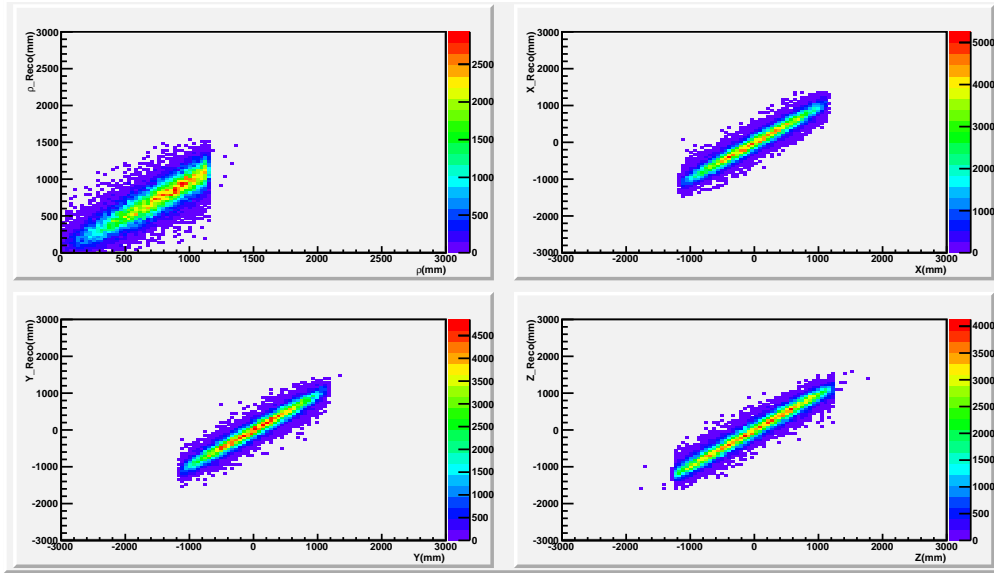
Figure 5.31: The correlation between the vertex reconstruction of the neutron capture on Gd, and the true vertex from the Monte Carlo information. Four plots show the vertex reconstruction as the functions of ρ, X, Y and Z of the truth positron vertex from the Monte Carlo prediction.

5.4.2 Prompt Energy Cut

Then we apply the prompt vertex selection on the neutrino data. For the data preparation, the Gd-capture fraction selection of the IBD candidate obeys the selection of the normal IBD candidate.[5] The prompt selection consist of two cuts: 1) energy from 0.5 Mev to 12.2MeV, and 2) the light noise cuts ($Q_{max}/Q_{tot} < 0.09$ and rms ($t_{start} < 40$ ns)). In order to get a whole spectrum, the delayed signal from neutron captures are expended from 0.7 to 12 MeV and valid for more strict light noise cuts ($Q_{max}/Q_{tot} < 0.055$ and rms ($t_{start} < 40$ ns)).[86] The multiplicity should be valid under the rules: no valid trigger in 100 μs before the prompt signal and 400 μs after the delayed signal.[86] The delayed and prompt spectra from the IBD candidates are shown in Figure 5.34. The background can be mixed in prompt signals in the IBD spectrum below 3 MeV. An additional prompt energy cut can be applied to the prompt signals to reduce the background in the delayed spectrum. Figure 5.35 shows the delayed spectrum with the three prompt energy cuts applied. Figure 5.36a shows the Gd-capture fraction results with different prompt energy cut applied. Most background
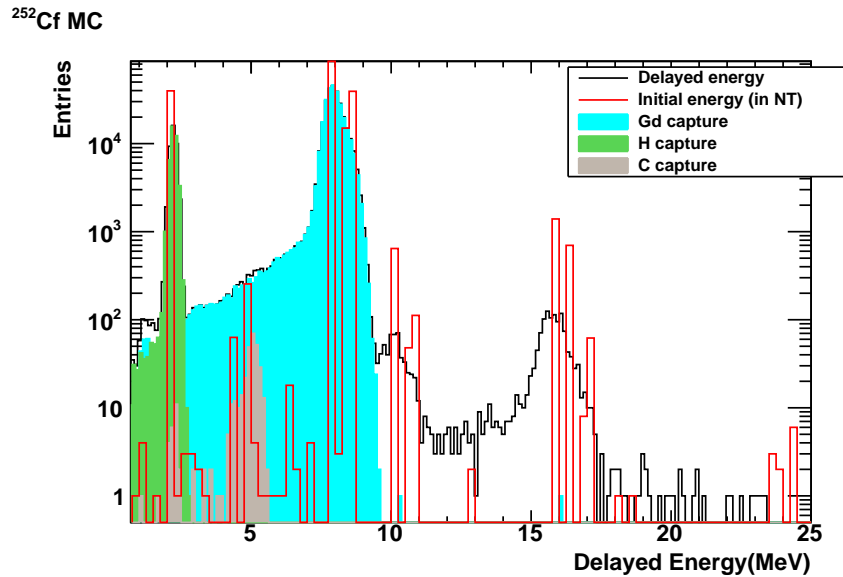
Figure 5.32: A ^{252}Cf delayed spectra contains the energy reconstruction of the Gd-capture contribution, the H-capture contribution, the carbon-capture contribution, the whole spectrum, and the initial deposited energy. A red curve indicates the initial deposited energy from the delayed signals, and a black curve is the whole spectrum from the energy reconstruction, which usually is observed from the experimental spectrum. This plot shows the regions of captures on Gd , H and carbon. The initial deposited energy of neutron captures can be defined by the theoretical capture energies: Gd-capture 7.5-9 MeV, H-capture 2-2.4 MeV, and carbon-capture 4.2-5.2 MeV.

IBD initial energy
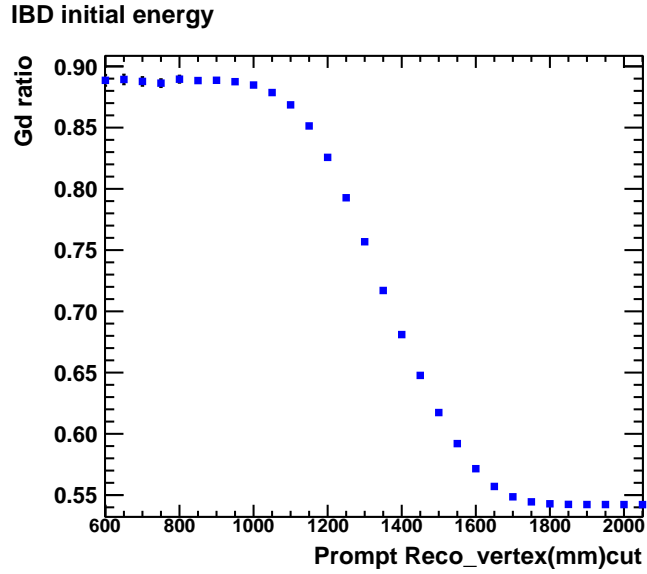
Figure 5.33: The Gd-capture fraction (with the initial deposited energy of the Monte Carlo prediction) from the neutrino events as a function of *Reco-vertex* along the ρ and z directions. The prompt vertex reconstruction is applied to select the neutrino event in the NT. The Gd-capture fraction values are stable around 0.88 in *Reco-vertex* $<$ 900 mm. (The NT wall is near 1150 mm.) When the neutrino's vertex is close to the NT wall, *Reco-vertex* $\sim$ 1000 mm -1200 mm, the spill-in/out effect starts to scale the Gd-capture fraction. When the neutrino's vertex is larger than the NT wall, *Reco-vertex* $>$ 1150 mm, the amount of the neutron captures on H increases. The amount of the neutron captures on Gd stay a certain constant to cause the reducing Gd-capture fraction with the increasing *Reco-vertex* (*Reco-vertex* $>$ 1150 mm).
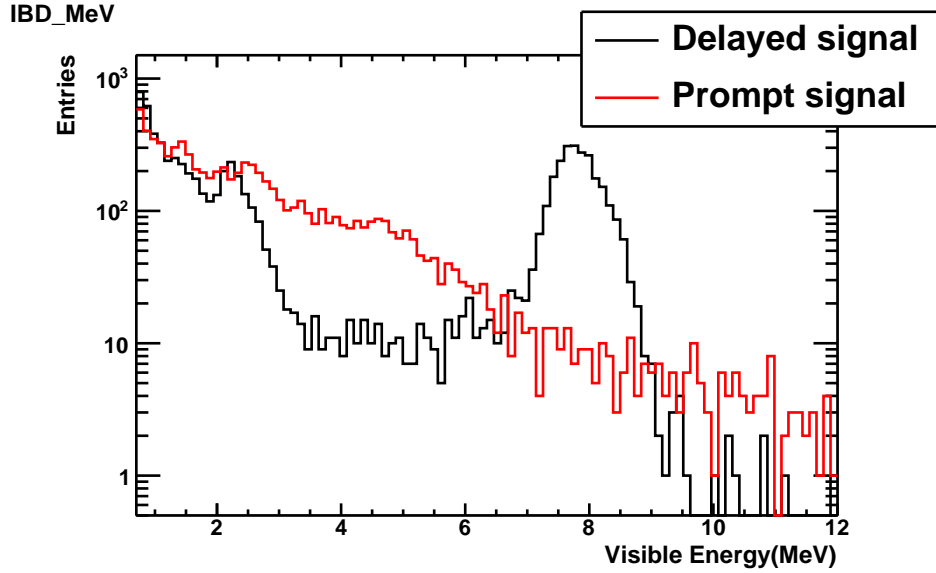
Figure 5.34: $\overline{\nu_e}$ whole delayed and prompt spectra. The red curve indicates the prompt signals, which contain a lot of background at the energy smaller than 3 MeV. The black curve indicates the delayed signals.
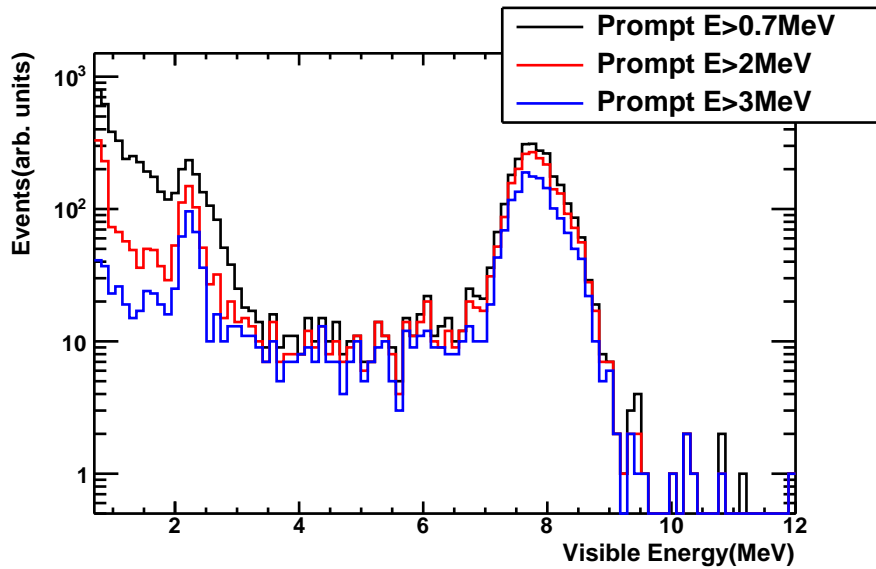
Figure 5.35: Three delayed spectra applied the prompt energy cuts: > 0.7 MeV, > 2 MeV, and > 3 MeV are shown. A black curve is the IBD delayed spectrum with the prompt energy larger than 0.7 MeV, a red curve is the delayed spectrum with the prompt energy larger than 2 MeV, and a blue curve is the delayed spectrum with the prompt energy larger than 3 MeV. The background events around 0.7 to 3 MeV are reduced with the increasing prompt energy.
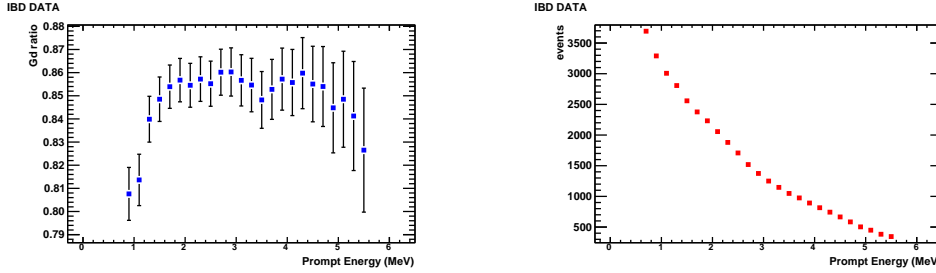
(a) IBD Gd-capture fraction as a function of the prompt energy cut.

(b) IBD statistics as a function of the prompt energy cut.

Figure 5.36: (a) The IBD Gd-capture fraction as a function of the prompt energy cut. (b) The IBD statistics as a function of the prompt energy cut.

events are located around 0.7-3 MeV in the IBD delayed and prompt spectra in Figure 5.34. From the ^{252}Cf Gd-capture fraction study, the additional prompt energy cut can avoid the background events efficiently. Figure 5.35 is a robust proof that the prompt energy cut can avoid the background in the IBD spectrum, too.

Unlike the ^{252}Cf source, the IBD reaction has a low daily rate. Applying a high prompt energy cut on the qualified candidates, the measurement will collect a very low statistics. Following the strategy of the vertex reconstruction, we choose a certain prompt energy at the range: 1) the Gd-capture fraction is stable, and 2) this range has at least 1000 events. If the event number is lower than 1000, the Gd-capture spectrum will be hard to fit by two Gaussian distributions. Figure 5.36a and 5.36b provide the information of the Gd-capture fraction as a function of the prompt energy cut and the statistics as a function of the prompt energy cut.

From Figure 5.36b, the prompt energy may be selected at the energy larger than 3 MeV in order to avoid the background. From Figure 5.36a, there is a stable range between 1.5 to 2.5 Mev. We can assume the prompt energy cut at > 2 MeV. We abandon the > 3 MeV cut because the Gd-capture spectrum has a low statistics from 6 to 12 MeV, and the Gd-capture fraction has a bias in this region. Although, a lot of background events have been avoided near > 3 MeV prompt energy cut. The best fit is shown in Figure 5.37, and the Gd-capture fraction is equal to 0.86 ± 0.009 based on a sample of 4050 IBD candidates.
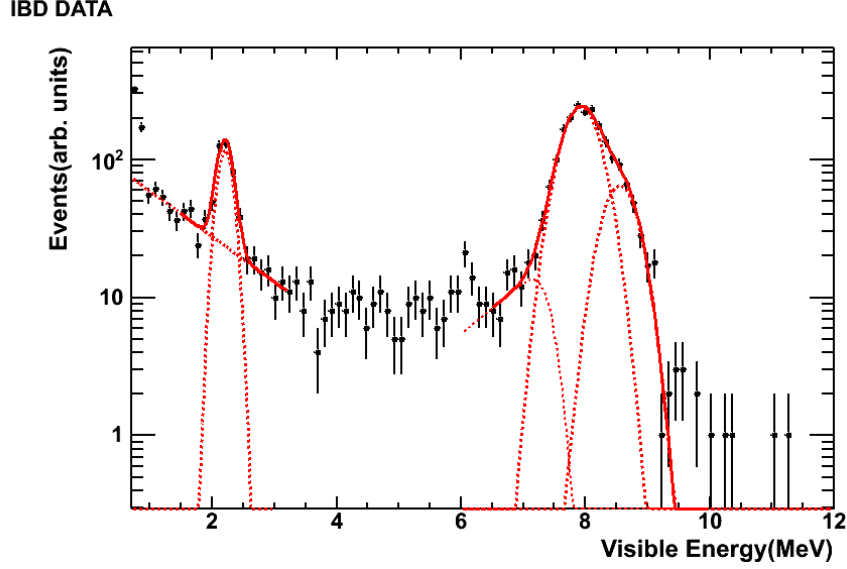
Figure 5.37: An experimental IBD delayed spectrum on the prompt signal > 2 MeV and *Reco-vertex* < 900 mm. The black dots are the data, and red curve is the best fits. The neutron captures on H are described by an exponential decay and a Gaussian function. The Gd-capture spectrum and the shoulder peak around 10 MeV are described by three Gaussian and one multiplied exponential functions. This plot is based on a sample of 4050 IBD candidates.

The Gd-capture fraction from the IBD Monte Carlo simulation is equal to 0.88 ± 0.003 based on a sample of 12051 IBD candidates.

5.4.3   Summary of Gd-Capture Fraction from IBD

The final results of the IBD Gd-capture fractions are almost equal to the results from the ^{252}Cf source. The error of Gd-fraction from the IBD data is larger than the ^{252}Cf's error due to the small sample size of IBD candidates. The Monte Carlo prediction provides the same Gd-capture fraction with the fraction of initial energy case for the IBD candidates. In the ^{252}Cf and the IBD studies, the Gd-capture fractions from the initial deposited energy is a little bit higher than from the Monte Carlo energy reconstruction (IBD: 0.885 ± 0.002, ^{252}Cf: 0.886 ± 0.003.) We applied the best fit on the energy reconstruction to find the Gd-capture fraction, and we counted the event numbers on the initial deposited energy to find the Gd-capture fraction. The summary of Gd-capture fraction is shown in Table 5.3.

70

Table 5.3: Summary of Gd-capture fractions from IBD and ^{252}Cf from the Double Chooz 1st publication[1].

source	IBD	^{252}Cf
data	0.860 ± 0.009	0.860 ± 0.005
MC	0.880 ± 0.003	0.880 ± 0.006
difference	$2.33 \pm 1.15\%$	$2.33 \pm 1.01\%$

In Table 5.3, the ^{252}Cf and the IBD analyses are from the Double Chooz first publication[1], which did not include the mapping energy scale and the time stability calibration. From the Table 5.3, the Gd-capture fractions from the IBD result and the ^{252}Cf result are consistent each other. There is no large discrepancy in these two methods (IBD and ^{252}Cf). For the higher statistical error from the IBD candidates, we can wait one more year, obtaining more live time, to improve the Gd-capture fraction from the IBD data. The difference of Gd-capture fraction between ^{252}Cf and IBD results is lower than 0.1%. Before we have enough IBD candidates (> 10000 candidates), we can estimate the systematic neutron detection efficiency by ^{252}Cf.

Chapter 6

Double Chooz Detector Seasonal Stability

The Double Chooz experiment has collected data since April 13, 2011, and the official running days are 334 days from April 13, 2011 to March 11, 2012 in the second publication[5]. In this one-year period, the detector stability is an important issue to affect the final $\sin^2 2\theta_{13}$ result. This chapter addresses several factors related to the stability of the Double Chooz far detector. The factors indicate the stable response of the detector over time, which is a fundamental assumption made in the evaluation of the systematic error in the $\sin^2 2\theta_{13}$ analysis. The temperature of the liquid scintillator is introduced in the first part. The variation of the liquid temperature with the seasonal change, and the stream of the daily IBD rate will be discussed, too. No correlation between the liquid temperature and the daily IBD rate is shown in the first part. In the second part, we have applied the detector to investigate the change of muon rate with the atmosphere temperature variation. This work shows that the far detector is in a reliable status in the last year, and it observes the correction between the daily muon rate and the atmosphere temperature. In the third part, these considerable factors in the $\sin^2 2\theta_{13}$ analysis is discussed and adds into the final analysis.

6.1 Double Chooz Physical Environment Monitoring System

A purpose of the Double Chooz experiment is searching for a non-vanishing mixing angle θ_{13} with two identical liquid detectors. The Double Chooz physical environment monitoring system records the condition of the experiment's environment which can impact the experiment's goals. The monitoring system includes the liquid temperatures, the magnetic fields of PMTs, the radon concentration, the humidity of the laboratory, and the photo-tube high voltages. This system scans all channels automatically, stores data in a common database, and warns shifters of unusual situations.[87]

Most functions in this system can be accomplished by 1-Wire ® from Dallas Semiconductor.[88] We use a single master bus for the multi-function controls and operations. Additionally, the master supports multiple devices on a single line. A server is a 10-inch laptop to run the master bus and to read every certain time period. The system is programmed in C++. Every device has a unique unalterable factory-laser ID, which can be identified easily by programming. The data can be accessed by an online data acquisition system from a common database, and the control system can give a feedback to the shifters.[87] Figure 6.1 is a schematic cartoon of the physical environment monitoring system.

6.1.1 Sensors Read by 1-Wire Devices

The sensors with 1-Wire devices are connected the bus with a high-speed 12 Mbps Universal Serial Bus (USB) interface, DS9490.[89] A single wire is sufficient for operating and functioning all devices on a loop; however, we still support 5 V to the IC power supply pins in order to speed up the readout during the data conversion time.[90] Each sensor assembly uses a standard "RJ11" 6P6C modular connector to hook on a switch box. Each switch box has 6 branches of RJ11 sockets providing 5 V for the IC power supply pins of the 1-Wire chip and 12 V for Buffer vessel monitors (BMONs). Six branches are from three MicroLAN couplers[91], DS2409. Each DS2409 can support two branches, main and auxiliary 1-Wire
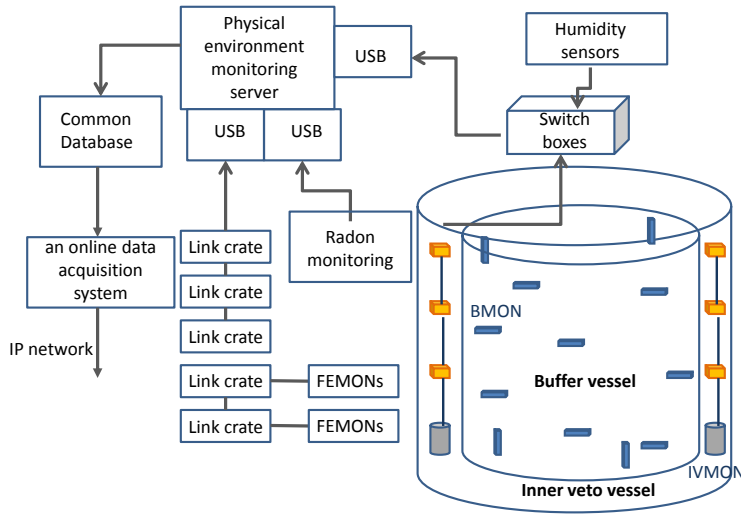
Figure 6.1: Physical environment monitoring system schematic cartoon.

outputs, and each branch can be programmed to open drains and to control outputs by the master bus. (see Figure 6.2.) A communication speed of DS2409 is 16.3k bits per second. In order to avoid static damages, we put a ESD protection diode before each 1-Wire output of DS2409.
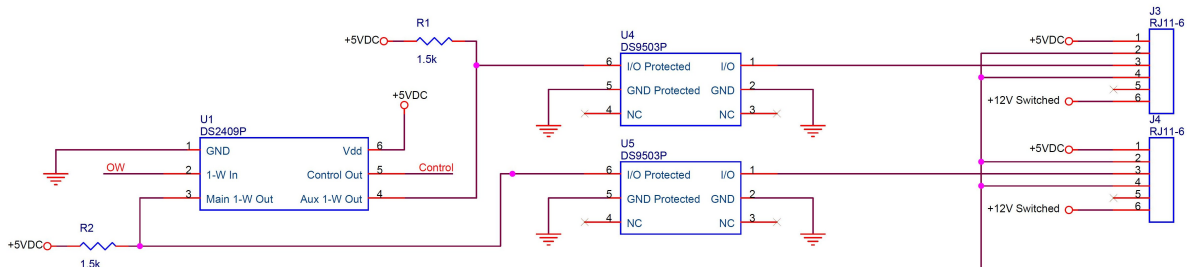
Figure 6.2: Schematic layout of the partial switch box. This schematic layout is made by the EDL at Kansas State University.

Sensors are Sunk in the Liquid

Main sensors can be divided two types. The first type of sensors are sunk into the liquid: 1) BMON and 2) Inner veto vessel monitor (IVMON). In order to be waterproof, the monitors are epoxy-potted on the acrylic base plates, and the sensors are put in the buffer and the IV

74

liquids. Each BMON mounts a three-axis magnetometer, HMC2003,[92] and a thermometer. The magnetometer is a three-axis magneto-resistive sensor assembly, and it is operated by a 12 V power supply. Its measurable range is ± 2 gauss, and the sensitivity is 40 microgauss. An ADC chip from Dallas Semiconductor accesses the output voltage of 2.5 V+B×(1V/gauss). Here, B is a constant. In order to reach a high resolution, the control program sends a 0 or 1 signal to a NPN amplifier, which can set/reset a current strap called SR$_+$/ and SR$_-$ pins. (see Figure 6.3) A set/reset action can flip the magnetization of the permalloy film inside the magnetometer and also the output voltages.[93] The thermometer,
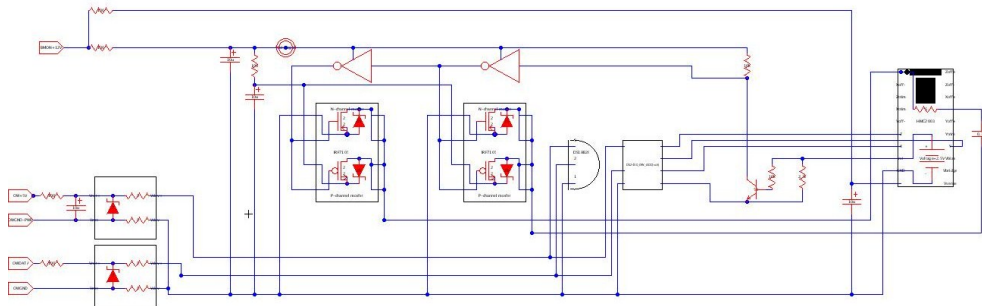
Figure 6.3: Schematic layout of the BMON.

DS18B20[90], is a digital thermometer, which can operate from -55 °C to 124 °C, and its accurate is ± 0.5 °C. There are 12 BMONs distributed uniformly in the buffer vessel. They collect data of the magnetic field near PMTs and liquid temperature in the buffer vessel. There are total 20 IVMONs distributed in several places: inside the IV vessel, on the IV vessel lid, on the bottom of a liquid expansion tank, and inside the pit pipe. There are 5 strings installed in the experimental hall, and each string consists of four IVMONs. The prototypes of the BMON and the IVMON are shown in Figure 6.4 and 6.5. The magnetic field in the buffer vessel has maintained a stable status since 2009. However, there were some unusual cases, which can be observed in the magnetic field history. In 2010, due to a broken PMT, the IV lid was opened on April sixth, and then the lid was closed back on May 21. Figure 6.6 shows one example of magnetic field as a function of the elapsed time from
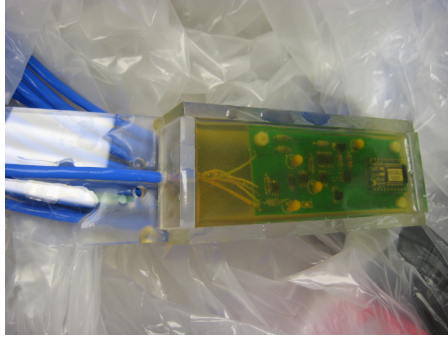
Figure 6.4: A prototype of the BMON is sealed in an acrylic box with epoxy.
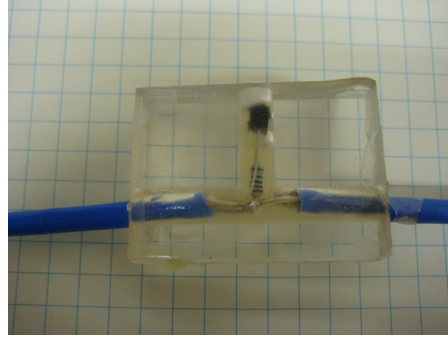
Figure 6.5: A prototype of the IVMON is sealed in an acrylic box with epoxy.

the BMON no.1, which is mounted on the buffer vessel lid. When the lid was opened, the BMON no.1 indicated an obvious change from April to May 2010. After the lid closed, the magnetic field became smaller in two directions. The explanation of this phenomenon is that the stainless vessel reduces a certain amount of the environmental magnetic field. The buffer liquid temperature has been waving slightly around 14 ± 1 °C with the seasonal variations after the detector installation. The mean lifetime, τ (see Eq. 6.1)[1], of the epoxy-potted assembly is equal to 23.81 ± 0.24 minutes. The temperatures read from these sensors are recorded every ten minutes. The most interesting period was during the filling liquid process, which started from October 2010. During this time, the reading temperature from the BMONs suddenly dropped in stages as a function of time, as shown in Figure 6.7. The colder liquid from the outside of the laboratory was injected into the warmer detector; therefore, the temperature of the detector decreased in the filling process. The liquid thermalization can be easily seen by the exponential functions in Figure 6.8. One can easily derive the thermal mean lifetime of the liquid in the detector from the best fit of the exponential function. The thermal mean lifetime at the bottom of the buffer vessel is around 8 days in Figure 6.8.

---

[1]

$$T(t) = T(0)e^{\frac{-t}{\tau}}. \tag{6.1}$$

The temperature, T, is a function of the t, time.
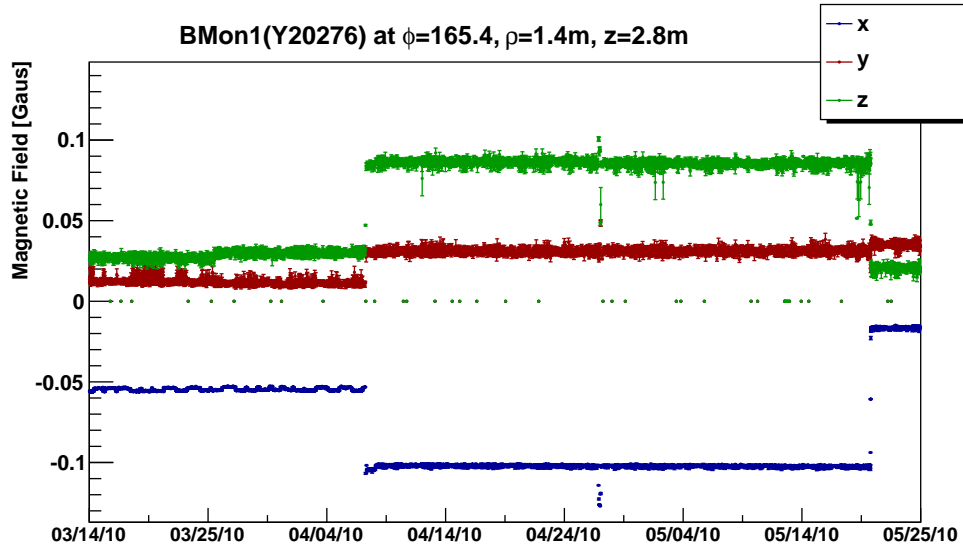
Figure 6.6: BMON no. 1 mounted on the buffer vessel lid is closest to the IV vessel lid. Three directions, x (blue), y (green), and z (red), in the detector are shown. The magnetic fields along x and y directions observed a strong change when the IV lid was opened. However, the z direction did not return back to the original stable value after the lid was closed.

Sensors are in Air

The second type of sensors are distributed in the laboratory hall to monitor the environmental conditions of the laboratory, the electronics control room, electronics split control boxes, and the high voltages of the front-end electronics boards. The most numerous sensors are 82 front-end electronics monitors (FEMON) to watch the high voltages of the front-end electronics (FEE) boards, which are located at the electronics control room. Each board has 4 channels, two from the VCC channels (IC power-supply pins: +5 V and -5 V) and two from the NIM (Nuclear Instrumentation Module)[94] channels (+6 V and -6 V), which are from four non-inverting amplifier circuits.[95] (see Figure 6.9) Additionally, each channel has its allowable value, which can give a feedback when voltages are too high or too low. Each crate has one thermometer in a RJ-11 modular phone jack box and 7 or 8 FEMONs The voltage and temperature are updated every 10 second. The humidity and temperature are important factors to cause damage on the electronics boards so a multi-function sensor, iButton[96], measuring the temperature and humidity is installed in the electronics control
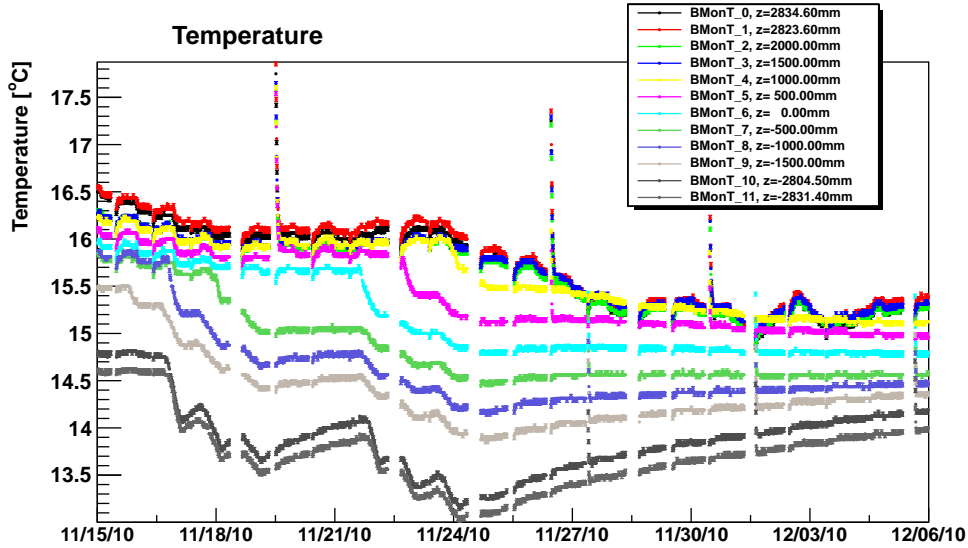
Figure 6.7: This plot shows the variation of liquid temperature in the filling process for the Double Chooz far detector. Cooler liquid from the outside of the laboratory decreased the temperature of the detector (the step functions), and subsequently thermal equilibriums processed at the interruptions of the filling process (the exponential functions). After Nov. 24, the liquid in the buffer vessel had been in the thermal equilibrium. Some BMONs (z > 1500 mm) above the liquid level did not show the exponential function feature at that time.

room, the laboratory hall, and electronics split control boxes. Figure 6.10 and 6.11 are prototypes of the FMON and the iButton. The RJ-11 modular phone jack box connect the 1-wire devices data and the ground wires (see Figure 6.13) back to the USB interface. The data from the sensors are written to the database each 10 seconds, and the shifters check an online interface panel shown in Figure 6.12.

6.1.2   Radioactivity

To ensure that the ambitious sensitivity goal of the Double Chooz experiments is attained, a great care must be taken to keep the background trigger rate below few events per second. A careful material selection is required. The background issue of the environment monitoring system is from radioactive isotopes of all sensor assemblies and cables in the liquid. The amount of isotopes in the sensor is listed in Table 6.1, which is from LBNL Berkeley Low Background Facility (Nathaniel Bowden and Allan R. Smith). The trigger rate from the
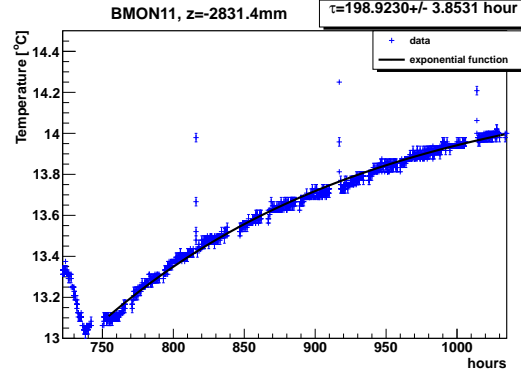
Figure 6.8: This plot is from one of the BMONs located at the bottom of the buffer vessel from Nov. 24 to Dec. 7 2010. This period was a over 12-day interruption of the filling process, and the buffer vessel was 67% full at least. The mean lifetime is $\tau = 198.92$ hours from the best fit of the exponential function.
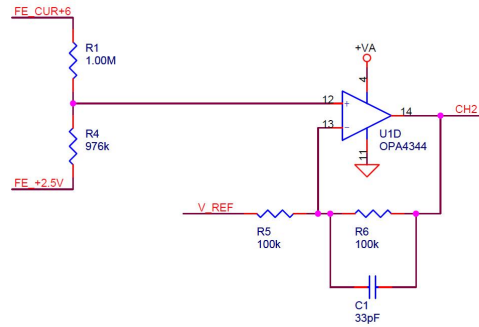
Figure 6.9: A schematic layout of the partial FEMON. This schematic layout is made by the EDL in Kansas State University.

isotopes can be simulated by the Monte Carlo prediction based on Geant4. The orientation of the BMONs is simulated with two different ways: 1) the sensors forward to the buffer vessel wall (see Figure 6.14a and 6.14b), and 2) the sensors pointing away from the wall.

The orientation of the sensors pointing away from the wall provides a smaller trigger rate than the rate from the orientation of the sensors pointing to the wall, and the rate result of the sensors pointing away from the wall is shown in Table 6.2. Assuming all cables are distributed uniformly in the detector, and we can propose a 0.5-mm thick painting model to simulate the trigger rate from the Monte Carlo prediction. The painting model result is

79
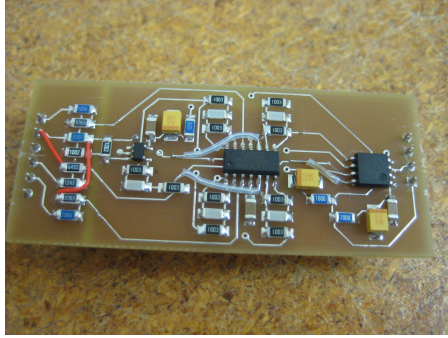
Figure 6.10: One of the FEMON prototypes.

Figure 6.11: Two of the iButton sensors mounted on a connector.
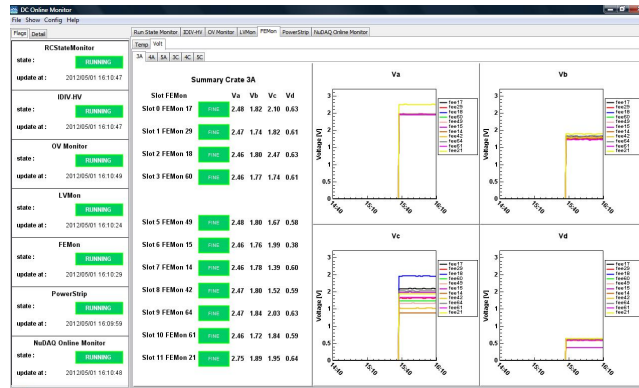
Figure 6.12: This is a control panel of the data acquisition and control system.[87] This page shows the FEMON voltage plots, and a shifter can notice the warning from the FEMONs.

shown in Table 6.3. According to the simulation results ,the total accidental trigger rate from the cables and sensors is smaller than 0.1 Hz. Comparing to the nature background from the muon and the PMT isotopes, the radioactivity of the physical environmental system is not a main issue. We have not included this simulation into the final $\sin^2 2\theta_{13}$ analysis.

Table 6.1: Isotopes of one BMON and 1-m cable.

isotope	ppm(sensors)	ppm(cables)
^{238}U	0.085(6)	<0.007
^{232}Th	0.40(2)	<0.015
^{40}K	<20	27(3)
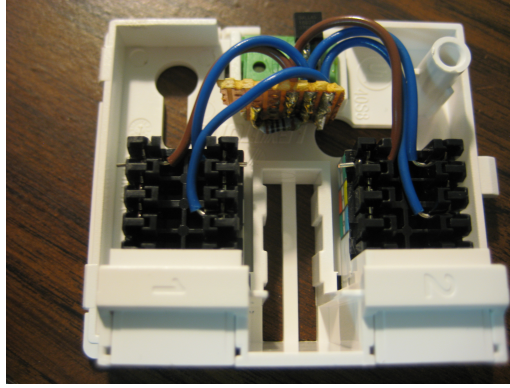
Figure 6.13: This is a RJ-11 modular phone jack box. It can converge FEMON 1-Wire data and ground lines back to a USB port. There is a thermometer in the box to monitor the NIM crate temperature.

Table 6.2: The simulation of trigger rates from BMONs.[2]

isotope	E>0.5MeV(Hz)	E>0.7MeV(Hz)	E>0.9MeV(Hz)
^{238}U	0.0068 ± 0.00011	0.0048 ± 0.00009	0.0035 ± 0.00008
^{232}Th	0.011 ± 0.00017	0.0075 ± 0.00014	0.056 ± 0.00012
^{40}K	0.0044 ± 0.00021	0.0036 ± 0.00020	0.0027 ± 0.00017

6.2 Temperature Variation and Expected Effect on IBD Candidates

The temperature in the 334-data running days changed about 0.8 ºC. (see Figure 6.15) The temperature deviation changes the density and the volume of the liquid scintillator. The proton number in the NT is changed by the density of the liquid scintillator. The waving liquid volume is inverse with the probability of the neutron capture on Gd. Figure 6.15 shows the GC temperature, the ratio of the liquid volume, and the ratio of proton in the

Table 6.3: The simulation of trigger rates from cables.[2]

isotope	E>0.5MeV(Hz)	E>0.7MeV(Hz)	E>0.9MeV(Hz)
^{238}U	0.00012 ± 0.000016	0.000090 ± 0.000014	0.000084 ± 0.000013
^{232}Th	0.00041 ± 0.000037	0.00033 ± 0.000033	0.00030 ± 0.000031
^{40}K	0.000011 ± 0.0000037	0.0000074 ± 0.0000030	0.0000037 ± 0.0000021

(a) The distribution of BMONs at X-Y intersection of the detector.

(b) The distribution of BMONs at Z intersection of the detector.

Figure 6.14: (a)The places of the BMONs at a x-y intersection view. The sensors are indicated by the blue square, and the yellow part is the acrylic base plate. (b)The locations of the BMONs at the z-intersection view. These two plots are taken from D.Shrestha, "Estimating the neutron background toward the measurement of neutrino mixing angle θ_{13} with the Double Chooz detector".[2]

NT as the functions of the data-takeing day. The systematic uncertainties on the liquid volume and proton number are estimated at $4.69 \times 10^{-6}\%$ and $4.82 \times 10^{-6}\%$ respectively. The number of the proton in the NT varies 0.07% per °C.[97] The liquid volume is defined as:

$$V_T = V_{T_0} \times (1 + (0.0007 \times \Delta T(°C) \times 20\% + 0.0009 \times \Delta T(°C) \times 80\%)) \tag{6.2}$$

V_T is the volume of liquid when the temperature is equal to T. ΔT is the bias of temperature to T_0. The liquid volumes change 0.07% per °C for PXE (20% of the solvent) and 0.09% per °C for dodecane (80% of the solvent).[97] From Eq. 4.2, the proton number in the NT affects the detection number of the electron antineutrino directly. The liquid volume increases or decreases with the temperature variation as well. The volume and proton number also affect the number of neutron capture in the detector. These potential factors included into the final $\sin^2 2\theta_{13}$ analysis will be discuss in Chapter 7.

82
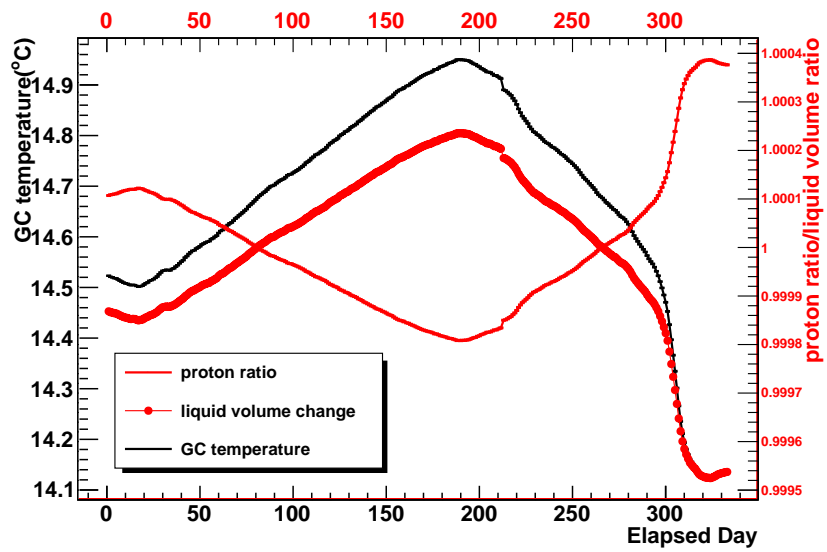
Figure 6.15: The GC temperature, the liquid volume, and proton variation of the NT as the functions of the data-taking day. The systematic uncertainties on the proton number and liquid volume in the NT are estimated at $4.82 \times 10^{-6}\%$ and $4.69 \times 10^{-6}\%$ respectively.

6.3 Seasonal Variations in the Underground Muon Rate Observed by Double Chooz Experiment

High energy muons observed by the underground detectors are produced by meson decays primarily. These mesons are the production of primary hadronic interaction after very high energy cosmic rays hit the stratosphere.[4] Most meson decays are from pion decays, and they happen right after cosmic rays hit the molecules on the top of atmosphere (see Figure 6.16). In summer, pion-nucleus interaction (see Figure 6.16) has a low chance to happen in the
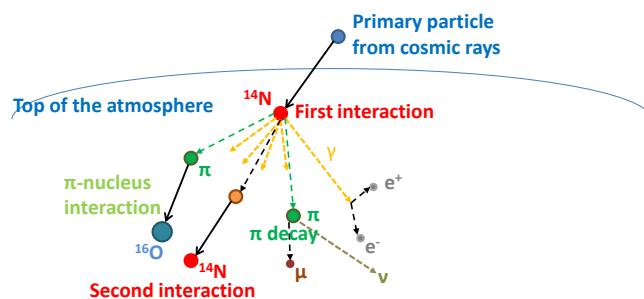
Figure 6.16: It is an illustration to explain meson decays after cosmic rays hit the top of atmosphere.

stratosphere due to the density of the air. Therefore, the underground detectors can observe high muon rates produced by cosmic rays. These pion-nucleus interaction and meson decays happen on top of the stratosphere (height: 50-40 km).

In 1940, M. Forro announced the correlation between the muon intensity and the air temperature above the sea level; people had not known muon particles yet that time.[98] Paul H, et al.[99] indicated that the temperature close to the ground exhibits no significant correlation with the muon rate. In 1997, the MACRO collaboration showed the underground muon rate was related to the effective atmospheric temperature variation with a high statis-

tical measurement.[100] This measurement represented a 'pion only' result, the temperature coefficient is equal to α_T = 0.83 ± 0.13; However, the contribution from kaon was discussed in the MACRO study, too.[100] In 2010, E. W. Grashorn, et al. extended the kaon effect and developed a method, which is used to determine the α_T and the ratio of kaon to pion, K/π ratio, of the local atmosphere.[3] The same year, the MIONS collaboration represented their result, α_T = 0.873 ± 0.009 (stat.) ± 0.01(syst.) and K/π ratio= $0.12^{+0.07}_{-0.05}$.[4] This chapter introduces the method from Grashorn, et al.[3] study first. This method can be simplified and only depends on the π contribution, which is exact the same as the method of MARCO collaboration. The data from Double Chooz experiment are applied by this new method to show the correspondence between the muon rate and a effective temperature, T_{eff}. The K/π ratio of Double Chooz experiment is represented in the final conclusion as well.

6.3.1 Analysis Method of the Relation between Muon Rate and Atmospheric Temperature

Muon Intensity and Muon Threshold Energy

The muon intensity is related to the production of meson. In the stratosphere, there are two kinds of interactions considered: 1) $M \rightarrow \mu + \nu_\mu$ and 2) hadronic interactions. The muon spectrum can be described by Eq. 6.3[3] with the meson intensity, $M(E, X, cos\theta)$.[101] θ is a zenith angle of muon sample, and its definition is shown in Figure 6.17.

$$P_\mu(E, X, cos\theta) = \sum_{mesons} \frac{\varepsilon_M}{X cos\theta(1 - r_M)} \int_{E_\mu}^{E_\mu/r_M} \frac{dEM(E, X, cos\theta)}{E^2}. \qquad (6.3)$$

M can be K or π, and r_M is equal to m_μ^2/m_M^2 (μ mass: m_μ, meson mass: m_M). X, the vertical atmospheric depth when particles travel through the material, is defined as $X = \int_{h'}^{\infty} \rho(h)dh$. (h, the height above the earth)[101] ε is the energy of the meson. The energy spectrum of muons should be integrated by the whole atmosphere in the relevant
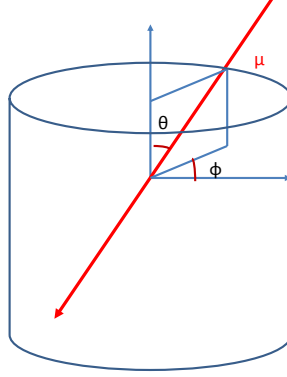
Figure 6.17: The definition of the zenith angle of the muon in the Double Chooz detector.

energy spectra, Eq. 6.4.[3,100]

$$\frac{dI_\mu}{dE_\mu} = \int_0^\infty P_\mu(E, X)dX \simeq C_0 \times E_\mu^{-(\gamma+1)}\left(\frac{A_\pi}{1 + 1.1E_\mu cos\theta/\varepsilon_\pi} + 0.635\frac{A_K}{1 + 1.1E_\mu cos\theta/\varepsilon_K}\right)$$
$$= 0.14E_\mu^{-(\gamma+1)}\left(\frac{1}{1 + 1.1E_\mu cos\theta/\varepsilon_\pi} + \frac{0.054}{1 + 1.1E_\mu cos\theta/\varepsilon_K}\right). \tag{6.4}$$

γ is a spectral index, 1.7. $A_{\pi,K}$ is defined as Eq. 6.5.[101]

$$A_{\pi,K} \equiv \frac{Z_{N\pi,K}(1 - \gamma_{\pi,K}^{\gamma+1})}{(1 - \gamma_{\pi,K})(\gamma + 1)}. \tag{6.5}$$

Z_{NM} is a spectral weight including the cross section moment. The energy of π or K, ε_M, is defined as $\varepsilon_M = \varepsilon_M^0(1+\eta)$. $\eta(X)$ is defined by $(T(X) - T_{eff})/T_{eff}$. T(X) is the atmospheric temperature with the depth of the particle track. The whole muon spectrum can be defined as Eq. 6.6[99]

$$I_\mu(E) = \int_{E_{th}}^\infty dE_\mu \frac{dI_\mu}{dE_\mu}. \tag{6.6}$$

E_{th} is the muon threshold surface energy, which is the minimum required energy to reach the underground detector. The final E_{th} is shown in Eq. 6.7 from Adamson et al.[102]

$$E_{th} = (E_{detected} + \frac{a}{b})e^{bd(\theta,\phi)} - \frac{a}{b}. \tag{6.7}$$

86

Table 6.4: The mean threshold energy for current underground detectors from Eq. 6.7. This table is referred from E. W. Grashorn, et. al studying[3].

Detector	Depth(MWE)	$\langle E_{th} \rangle (GeV)$
MINOS Near	225	51
Baksan	850	234
MINOS Far	2100	730

The parameters, a and b, as the functions of the muon energy are: $a = 0.00195 + 1.09 \times 10^{-4} ln(E)$ GeV cm^2/g, and $b = 1.381 \times 10^{-6} + 3.96 \times 10^{-6} ln(E)$ GeVcm^2/g. The muon threshold energy calculated by Eq. 6.7 in different experiments are shown in Table 6.4.[3]

In the Double Chooz experiment, we cannot reach the muon energy experimentally when muons arrive in the detector. We only know the deposited energy in the detector from the arrival muons. Eq. 6.7 cannot apply to Double Chooz data analysis. From the MACRO study, the muon threshold energy can be derived by the equation of the rock depth, $D = D(\theta, \phi)$, as Eq. 6.8.

$$E_{th} = E_{th}(\theta, \phi) = 0.53 TeV(e^{0.4D(km)} - 1). \tag{6.8}$$

We assume that the energy of the arrival muon in our detector is larger than the theoretical muon threshold energy from Eq. 6.8. This theoretical threshold energy is assumed the minimum energy of arrival muon.

The Correlation between Temperature and Muon Intensity

The correlation of the atmospheric temperature and the muon intensity can be written as:

$$\frac{\Delta I_\mu}{I_\mu^0} = \frac{1}{I_\mu^0}\left(\int_0^\infty dX \alpha^\pi(X)\frac{\Delta T(X)}{T_{eff}} + \int_0^\infty dX \alpha^K(X)\frac{\Delta T(X)}{T_{eff}} \right). \tag{6.9}$$

In the Eq. 6.9, $\Delta T(X)$ is equal to $T(X) - T_{eff}$. If ΔI_μ is equal to 0, we can derive the T_{eff} function as:[3]

$$\int_0^\infty dX T_{eff}\frac{\alpha^\pi(X)}{I_\mu^0} + \int_0^\infty dX T_{eff}\frac{\alpha^K(X)}{I_\mu^0} = \int_0^\infty dX T(X)\frac{\alpha^\pi(X)}{I_\mu^0} + \int_0^\infty dX T(X)\frac{\alpha^K(X)}{I_\mu^0}$$

$$T_{eff} = \frac{\int_0^\infty dX T(X)\alpha^\pi(X) + \int_0^\infty dX T(X)\alpha^K(X)}{\int_0^\infty dX \alpha^\pi(X) + \int_0^\infty dX \alpha^K(X)}. \tag{6.10}$$

We can substitute $\varepsilon_M = \varepsilon_M^0(1 + \eta)$ into Eq. 6.4 and give another equation, Eq. 6.11[3].

$$\frac{\Delta dI_\mu}{dE_\mu} \simeq \frac{E_\mu^{\gamma-1}}{1 - Z_{NN}} \int_0^\infty \frac{dX(1 - X/\Lambda'_M)^2 e^{-X/\Lambda_M} \eta(X) A_M^1}{1 + B_M^1 K(X)(\langle E_\mu cos\theta \rangle/\epsilon_M^0)^2}$$

$$A_K^1 \equiv 0.635 \frac{Z_{N,K}(1 - \gamma_K^{\gamma+1}(1 - \gamma_\pi))}{Z_{N,K}(1 - \gamma_\pi^{\gamma+1}(1 - \gamma_K))},$$

$$A_\pi^1 \equiv 1, \tag{6.11}$$

$$B_M^1 \equiv \frac{(\gamma + 3)(1 - \gamma_M^{\gamma+1})}{(\gamma + 1)(1 - \gamma_M^{\gamma+3})}$$

$$K(X) \equiv \frac{(1 - X/\Lambda'_M)^2}{(1 - e^{-X/\Lambda'_M})\Lambda'_M/X}.$$

The absorption mean free path of the cosmic ray is defined as Λ_M, and the absorption mean free path of the meson is defined as $1/\Lambda'_M \equiv 1/\Lambda_N - 1/\Lambda_M$. From Eq. 6.9 and Eq. 6.11, we can obtain the $\alpha(X)$ shown as:[3]

$$\alpha(X) = W^M(X) E_{th}^{-(\gamma+1)}$$

$$W^M(X) \simeq \frac{(1 - X/\Lambda'_M)^2 e^{-X/\Lambda_M} A_M^1}{\gamma(\gamma + 1) B_M^1 K(X)(\langle E_{th} cos\theta \rangle/\epsilon_M^0)^2}. \tag{6.12}$$

$W^M(X)$ is a weight function. Following Eq. 6.12, the T_{eff} approximation is Eq. 6.13.[3] The integration is replaced by a summation because the atmospheric measurement usually measure at each discrete atmospheric pressure level.

$$T_{eff} \simeq \frac{\sum_{n=0}^N \Delta X_n T(X_n)(W_n^\pi + W_n^K)}{\sum_{n=0}^N \Delta X_n (W_n^\pi + W_n^K)}. \tag{6.13}$$

The linearity between the muon intensity and the muon rate can be written:[100]

$$\frac{\Delta I_\mu}{I_\mu} = \frac{\frac{\Delta N_i/t_i}{\epsilon A_{eff}\Omega}}{\frac{N_i/t_i}{\epsilon A_{eff}\Omega}} = \frac{\frac{\Delta N_i}{t_i}}{\frac{N_i}{t_i}} = \frac{\Delta R_\mu}{R_\mu}. \tag{6.14}$$

N_i is a muon event number in the counting live time, t_i. The tracking muon efficiency is ϵ, and the detector solid angle is defined as Ω. The correlation between the muon rate and the effective temperature, T_{eff}, is described as Eq. 6.15[3]. A temperature coefficient is defined as α_T.

$$\frac{\Delta R_\mu}{R_\mu} = \alpha_T \frac{\Delta T_{eff}}{T_{eff}}.$$

$$\alpha_T = \frac{1}{I_\mu^0} \int_0^\infty dX \alpha^\pi(X) + \int_0^\infty dX \alpha^K(X). \tag{6.15}$$

In Eq. 6.15, the muon rate is proportional to T_{eff}. In the next section, the Double Chooz data and the atmospheric temperature data from NASA (National Aeronautics and Space Administration) and ECMWF (European Centre for Medium-Range Weather Forecasts) demonstrate Eq 6.15 and the theoretical α_T. Then, we can search for the ratio of κ to π in the local atmosphere.

6.3.2 Data Analysis

Atmospheric Temperature

There are two atmospheric temperature data applied to the study. The first data set is retrieved from the NASA website, AIRS Online Visualization and Analysis. The temperature data of NASA is from the Aqua and Aura satellites. The satellite sensors are able to measure the spectra of the microwave and infrared (IR) wavelength bands, which are temperature-dependency.[103] The atmospheric temperature can be reached by analyzing these spectra. The satellite measures the ascending and descending nodes [1] (day and night) daily, and the temperature error is calculated by the standard deviation of two data sets daily.[104] The selected area is close to the Chooz area, latitude (50.041, 50.157), longitude (4.69, 4.901). The mean temperature is given by averaging 2 data points (two nodes) at a certain atmospheric pressure. The average atmospheric temperature as a function of Double Chooz data-taking day at different atmospheric pressures can be seen in Figure 6.18.

The second atmospheric temperature data are retrieved from ERA Interim Website of ECMWF.[105] ECMWF applies the numerical weather prediction of the computer calculation to predict the weather, and the calculations rely on the constantly observed meteorological data around the world.[106] ERA Interim is a global atmospheric reanalysis, and its daily result can be accessed since 1 Jan 1979. The selected area is at latitude (49.50, 51.00), longitude (4.5, 6.0) in this study. Four geographic positions from the selected area and four times, 0000h, 0600h, 1200h and 1800h, a day are involved the temperature data at a certain

---

[1]An orbit of the ascending node: the satellite travels from south to north over the Earth. An orbit of the descending node: The satellite travels from north to south over the Earth.[104]
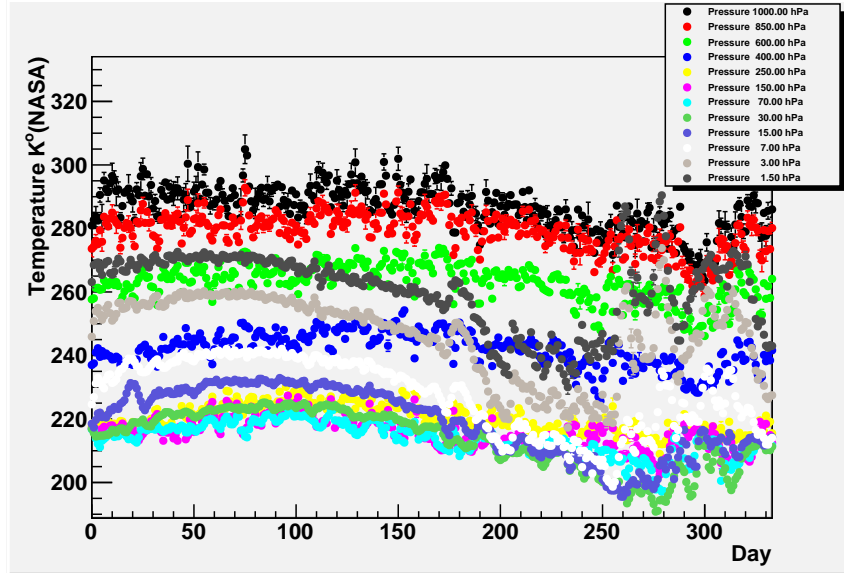
Figure 6.18: A summary plot of the atmospheric temperature retrieved from NASA at differen pressures.

atmospheric pressure. Each mean temperature is deriving by averaging 16 data points (4 times a day and 4 geographic positions) at a certain atmospheric pressure. The average March atmospheric temperature profiles of NASA and ECMWF can be seen in Figure 6.19

NASA collected atmospheric temperatures at 24 discontinuous atmospheric-pressure levels: 1000 ,925 ,850 ,700 ,600 ,500 ,400 ,300 ,250 ,200 ,150 ,100 ,70 ,50 ,30 ,20 ,15 ,10 ,7 ,5 ,3 ,2 ,1.5 and 1 hPa, and two times a day. The ERA Interim model has atmospheric temperatures at 37 discontinuous atmospheric-pressure levels: 1000, 975, 950, 925, 900, 875, 850, 825, 800, 775, 750, 700, 650, 600, 550, 500, 450, 400, 350, 300, 250, 225, 200, 175, 150, 125, 100, 70, 50, 30, 20, 10, 7, 5, 3, 2 and 1 hPa, four times a day.

Experimental Data from Double Chooz

In the Double Chooz experiment, the official data have been collected from April 13 2011 to March 11 2012 (total 334 days).[5] The cosmic muons are tagged by the IV system in this study because the OV data does not included all official runs. The muon selection consists of 2 cuts: 1) high energy muons crossing the ID (the ID deposited energy > 30 MeV)
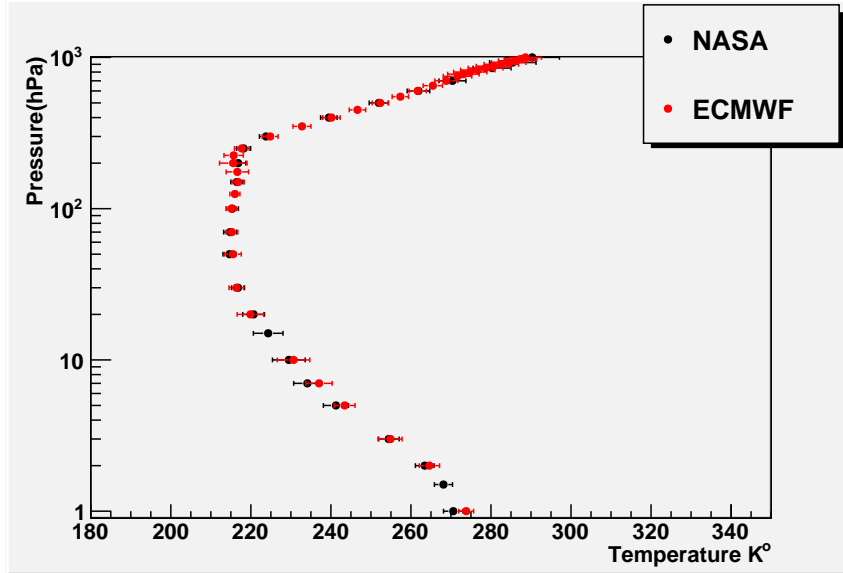
Figure 6.19: The average March atmospheric temperature profiles from NASA and ECMWF. The y axis range is from 1 hPa (near 50 km hight from the sea level close to the top of the stratosphere) to 1000 hPa. 1 hPa is equal to 1.02 g/cm^2.

or 2) tagged by the IV (the IV deposited energy > 5 MeV (10000 DUQ)) in the Double Chooz publication.[5] However, there are many non-muon events included in the selection: for instance, the light noise in the ID. In order to find out the real muons, the muon selection is examined. The spectrum of the muon deposited energy in the IV divides into three zones, which is shown in Figure 6.20: from 5 to 15 MeV, 2) 15 to 25 MeV, and 3) over 25 MeV. The correlation between the muon rates of three groups and effective atmospheric temperature can be seen in Figure 6.21. Figure 6.21 shows the muon rates of three regions and the T_{eff} of NASA and ECMWF as the functions of the data-taking day. The $\Delta R_\mu / < R_\mu >$ at the deposited energy larger than 25 MeV has a high correspondence with the $\Delta T_{eff} / < T_{eff} >$. Most noises, which are not related to the effective temperature, are in the IV deposited energy smaller than 25 MeV.

The expected value, $\langle E_{th} \cos\theta \rangle$, is defined as an approximation, $\langle E_{th} \cos\theta \rangle \simeq \langle E_{th} \rangle \langle \cos\theta \rangle$ in this study. $\langle \cos\theta \rangle$ is determined by the muon track reconstruction in the ID and the IV. A basic procedure superimposes the spherical light wavefront emitting along the muon track, and the waveform consists of a Cherenkov cone in the ID.[107] A diagram of a Cherenkov cone
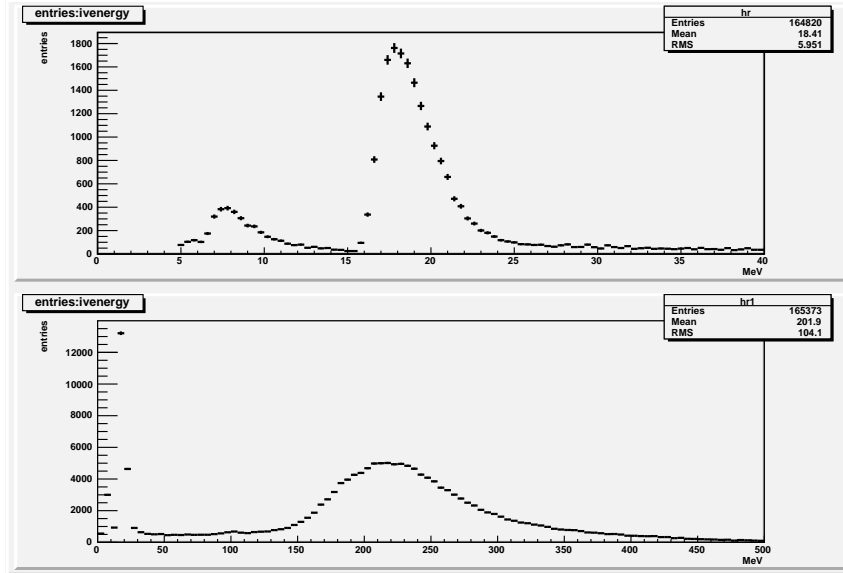
Figure 6.20: Two plots show the muon deposited energy in the IV. The bottom plot zooms the muon distribution in the range, 0 to 40 MeV. Three regions can be observed, 1) the IV deposited energy from 5 to 15 MeV, 2) 15 to 25 MeV, and 3) over 25 MeV.

and the spherical light fronts is presented in Figure 6.22.

The ID muon trajectory is reconstructed by the hit timing information of the wavefront of the Cherenkov cone. The spatial pattern can be observed from the PMT light of the hit time in the ID. In the IV, the volume is not a complete cylinder (see Chapter 4); therefore, the Cherenkov cone cannot be reconstructed. The ideal arrival time of the first photon hitting each PMT is based on a maximum likelihood algorithm in the IV reconstruction. The resolution of the muon track is 350 mm for the ID and 600 mm for the IV.[5] The $\cos\theta$ and ϕ of muon reconstruction can be determined by the entry and the exit of muon event (see Figure 6.23). The preferred directions of muons, $\cos\theta$ and ϕ , are seen in Figure 6.23.

From Figure 6.24, the topographic feature of the surrounding area indicates that the terrain of the Chooz is very uneven, and the steepest slope is near Meuse River. Therefore, the $\cos\theta$ and ϕ distributions show that most muons are not from the top ($\cos\theta = 1$) instead of from one side. The $\cos\theta$ distribution of the observed muon is shown in Figure 6.23a, and $\langle\cos\theta\rangle$ is equal to 0.611 ± 0.290.

From the Eq. 6.8, the threshold muon energy of the Double Chooz far detector (MWE:
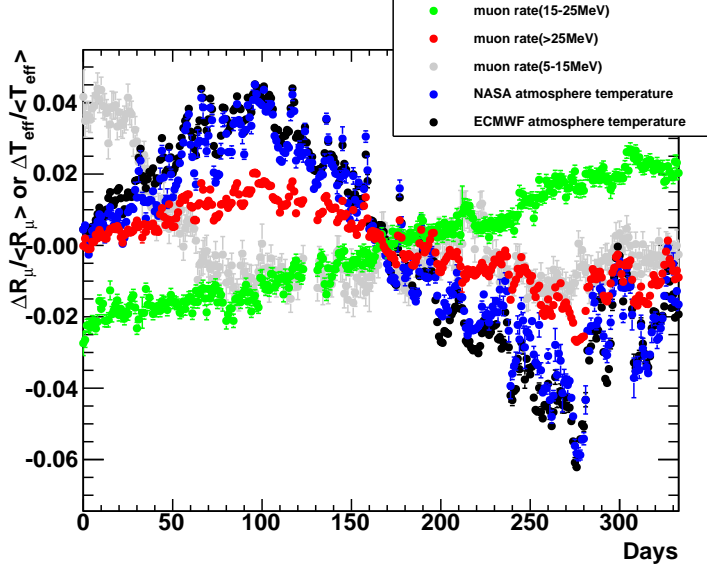
Figure 6.21: The daily muon rates of three groups (IV deposited energy: 1)from 5 to 15 MeV, 2) 15 to 25 MeV, and 3) over 25 MeV.)and the effective temperatures are shown as the functions of the elapsed day. The average muon rates are: 1)39.8918 ± 0.0014 Hz at > 25 MeV(red), 2) 4.8315 ± 0.0005 Hz at 15-22.5 MeV (green), and 3) 1.0826 ± 0.0002 Hz at 5-15 MeV(gray). The blue and black dots are NASA and ECMWF normalized effective temperatures respectively. The $\Delta R_\mu / < R_\mu >$ at >25 MeV, has a high correspondence with the $\Delta T_{eff} / < T_{eff} >$.

300 m) is equal to 0.0676 TeV. The $\langle E_{th} \rangle$ is from the 10^7 samples generated by Eq. 6.4, and the samples satisfying $E_\mu > 0.0676$ TeV are accounted. The $\langle E_{th} \rangle$ is equal to 0.1180 $\pm$ 0.0002 TeV, and $\langle E_{th} \cos \theta \rangle$ is equal to 0.0721 ± 0.0342 TeV. The other parameters in the $W^{\pi,K}$ (see Eq. 6.12) are listed in Table 6.5. The definitions of the parameters in the Table 6.5 are listed below:

$A^1_{\pi(K)}$: a constant defined as Eq. 6.5;

$r_{K/\pi}$: the atmospheric K/π ratio;

$B^1_{\pi(K)}$: a parameter relative atmospheric attenuation of mesons;

Λ_N and $\Lambda_{\pi(K)}$: the attenuation lengths for cosmic ray primaries and pions or kaons;

$\epsilon_{\pi(K)}$: the meson critical energy;

γ: the muons spectral index.

The atmospheric temperatures from NASA and ECMWF are substituted into Eq. 6.13
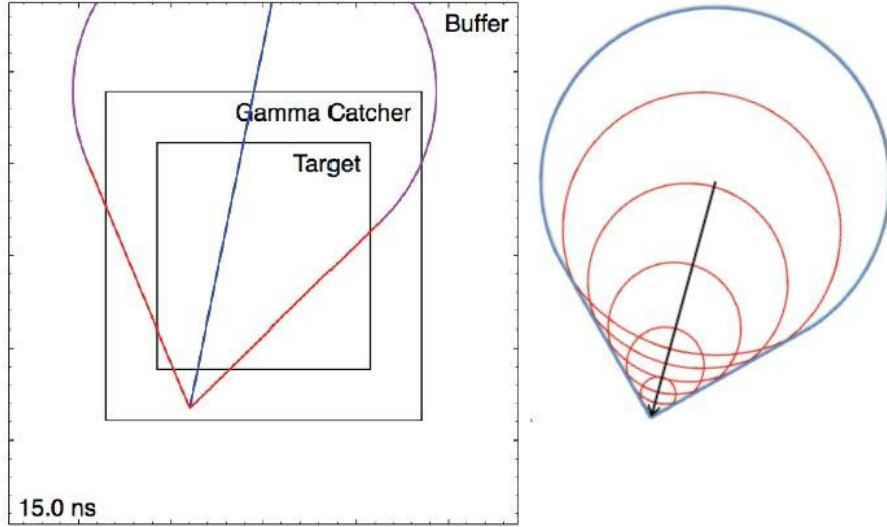
Figure 6.22: The diagram of a Cherenkov cone and spherical light fronts in the Double Chooz ID. (from Michael Wurm, Double Chooz Document 3826[107])

to derive T_{eff}. Eq. 6.15 can be written by the muon rate and T_{eff} as

$$\frac{\Delta R_\mu}{\langle R_\mu \rangle} = \alpha_T \frac{\Delta T_{eff}}{\langle T_{eff} \rangle}.$$ (6.16)

From Figure 6.25, the high correspondence between α_T and IV deposited energy cut shows at IV deposited energy larger than 30 MeV. The mean of the effective temperature from NASA is 218.346 ± 0.406 K, and the mean of the effective temperature from ECMWF is equal to 218.997 ± 0.241 K.

According to Eq. 6.15, the IV selection can be examined by the α_T value as a function of the IV-deposited-energy cut. Figure 6.25 shows α_T and the average-muon rate as the functions of the IV deposited energy cut. The α_T becomes stable when the IV deposited energy is larger than 30 MeV. This phenomenon agrees with that the muon deposited energy > 25 MeV in the IV has a high correspondence with the T_{eff} in Figure 6.20 and Figure 6.21. The deviation of α_T is lower than 0.1% between 30 and 50 MeV (from the top plot in Figure 6.25). In order to avoid the noises, a strict cut, the deposited energy larger than 50 MeV, is applied, and the averaged muon rate, $\langle R_\mu \rangle$, is equal to 39.048 ± 0.001. The α_T increases slightly at the deposited energy > 100 MeV because a large number of valid

94

(a) θ distribution of muons.

(b) ϕ distribution of muons.
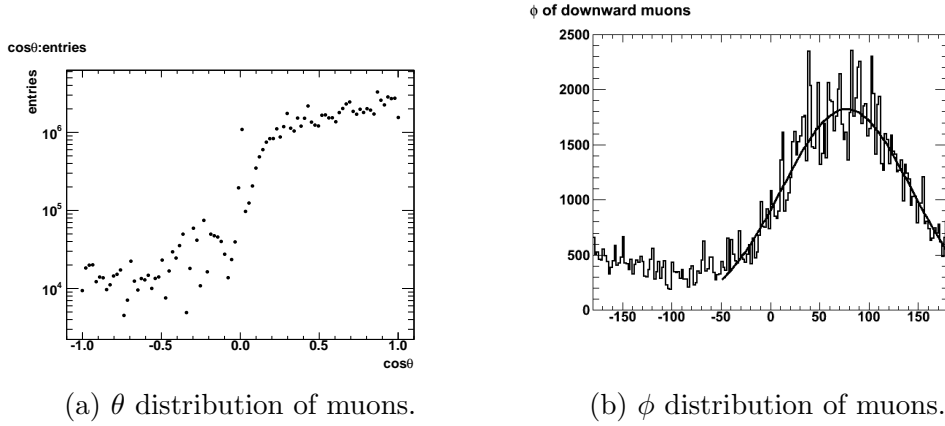
Figure 6.23: (a) The $\cos\theta$ distribution of muon reconstruction. (b) ϕ distributions of muon reconstruction is from E. P. Caden, Studying Neutrino Directionality with the Double Chooz Experiment.[108] The $\langle\cos\theta\rangle$ is equal to 0.611 ± 0.290. Muons have a preferred ϕ around 77°.

Table 6.5: Parameter values in the weight function, W(X). This list is taken from P. Adamson et al.[4] except $\langle E_{th}\cos\theta\rangle$.

Parameter	Value
A_π^1	1[3,110]
A_K^1	$0.38 \times r_{K/\pi}$[3,110]
$r_{K/\pi}$	0.149 ± 0.06[111]
B_π^1	1.460 ± 0.007[3,110]
B_K^1	1.740 ± 0.028[3,110]
Λ_N	$120g/cm^2$[101]
Λ_π	$160g/cm^2$[101]
Λ_K	$180g/cm^2$[101]
$\langle E_{th}\cos\theta\rangle$	$0.0721 \pm 0.0342 TeV$
γ	1.7 ± 0.1[102]
ϵ_π	$0.114 \pm 0.003 TeV$[3,110]
ϵ_K	$0.851 \pm 0.014 TeV$[3,110]
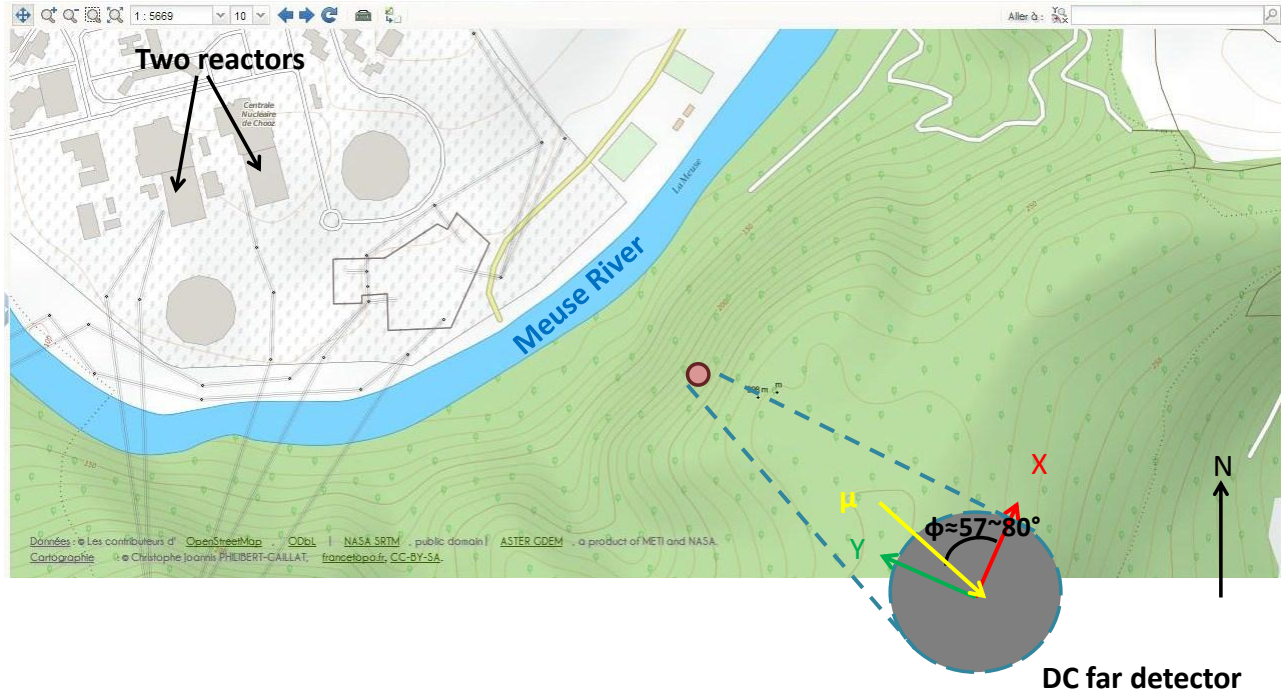
Figure 6.24: The topographic feature near the Chooz[109] and the coordinates of the far detector. The terrain of the Chooz is very uneven, and the steepest slope is near Meuse River. The angle of ϕ from the laboratory to the face of hill is around 57 to 80 degree, and most muons are captured from this direction.

muons are abandoned (see Figure 6.21).

6.3.3 Temperature Coefficient and the Ratio of Kaon and Pion from Data

The correspondence between the $\Delta T_{eff}/\langle T_{eff} \rangle$ and $\Delta R_\mu/\langle R_\mu \rangle$ in Figure 6.21 provides the value of α_T. The value, α_T, in Eq. 6.15 is provided by a linear regression with 323 points of the $\Delta R_\mu/\langle R_\mu \rangle$ as a function of $\Delta T_{eff}/\langle T_{eff} \rangle$. 323 data points are valid for the data quality control, and they are not included in the reactor off off periods. The linear regressions

96
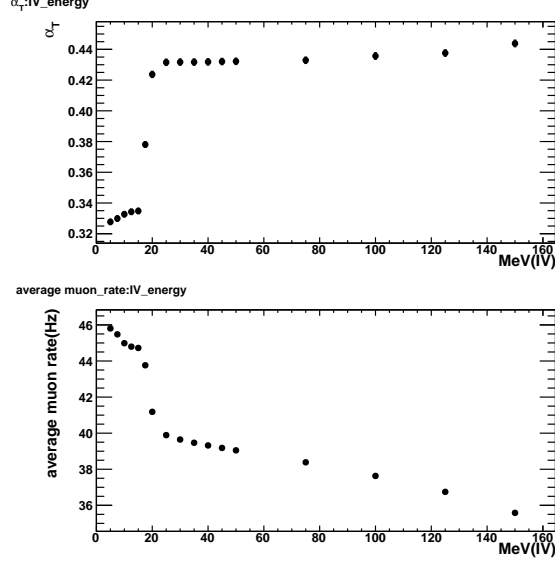
Figure 6.25: The α_T (top) and the muon rate (low) as the functions of the IV deposited energy cut respectively.

of DC:NASA (Double Chooz data vs.NASA data) and DC:ECMWF (Double Chooz vs. ECMWF data) are presented in Figure 6.26a and Figure 6.26b respectively. The α_T is equal to 0.372 ± 0.001)(stat. only) from DC:ECMWF, and the α_T is equal to 0.432 ± 0.002(stat. only) from DC:NASA.

The systematic uncertainties are estimated by including the parameters' error to obtain the deviation of α_T. The list shows the most dominant parameters in Table 6.6. Except $\langle E_{th} \cos\theta \rangle$ and $\langle T_{eff} \rangle$, all parameters and uncertainties are from P. Adamson et al.[4] The large uncertainties are from $\langle E_{th} \cos\theta \rangle$ and $\langle T_{eff} \rangle$. The results from DC:ECMWF and DC:NASA are $\alpha_T = 0.372 \pm 0.001$ (stat.) ± 0.009 (syst.) and $\alpha_T = 0.432 \pm 0.002$ (stat.) ± 0.010 (syst.) respectively.

In Grashorn et al. study[3], the prediction of α_T is:[99]

$$\alpha_T = \frac{1/\varepsilon_K + A_K^1 (D_\pi/D_K)^2/\varepsilon_\pi}{D_\pi(1/\varepsilon_K + A_K^1 (D_\pi/D_K)/\varepsilon_\pi)}$$
$$D_{\pi(K)} = \frac{\gamma \varepsilon_{\pi,K}}{(\gamma + 1)1.1 E_{th} \cos\theta} + 1. \tag{6.17}$$
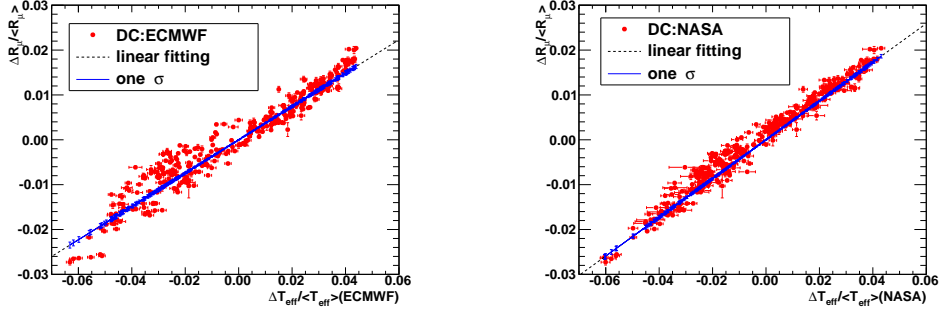
(a) A linear regression of ECMWF data (b) A linear regression of NASA data

Figure 6.26: (a) The $\Delta R_\mu/\langle R_{mu}\rangle$ as a function of $\Delta T_{eff}/\langle T_{eff}\rangle$ from DC:ECMWF is fitted by a linearity (fixed the y intercept at 0). The slop, α_T, is equal to 0.372 ± 0.001, and χ^2 is equal to 3910.68/321. (b) The $\Delta R_\mu/\langle R_{mu}\rangle$ as a function of $\Delta T_{eff}/\langle T_{eff}\rangle$ from DC:NASA is fitted by a linearity (fixed the y intercept at 0). The slop, α_T, is equal to 0.432 ± 0.002, and χ^2 is equal to 1123.09/321.

Table 6.6: Systematic errors of the experimental temperature coefficient.

Parameter	$\Delta\alpha_{T(DC:NASA)}$	$\Delta\alpha_{T(DC:ECMWF)}$
$r_{K/\pi}$	2×10^{-5}	1.4×10^{-5}
B_π^1	6×10^{-5}	5.5×10^{-5}
B_k^1	$< 10^{-6}$	$< 10^{-6}$
$\langle E_{th}cos\theta\rangle$	0.00964	0.009073
γ	0.000247	0.000229
ε_π	0.000624	0.000573
ε_k	10^{-6}	$< 10^{-6}$
$\langle T_{eff}\rangle$	0.000271	0.000292
total	0.010	0.009

α_T from π or K only is defined as[3]

$$(\alpha_T)_{\pi,K} = \frac{1}{D_{\pi(K)}} \qquad (6.18)$$

Eq. 6.18, pion model only, can predict the result from MARCO study[100]. According to the muon intensity as a function of muon energy in Eq. 6.4, The generated 10^7 samples satisfy $E_\mu > E_{th}$, and the $\cos\theta$ is equal to 0.611 from the OV tracking. The predictions of α_T, α_π, and α_K are shown in Figure 6.27, and the data from DC:NASA and DC:ECMWF are included in this plot. The results from other underground experiments in Figure 6.27 are from the Borexino[112]. The systematic uncertainties of the predicted α_T are listed in
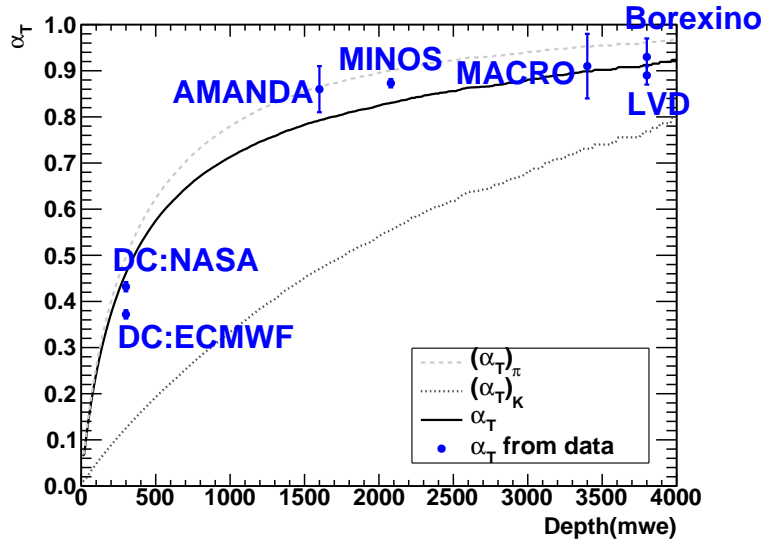
Figure 6.27: The predicted α_T as a function of detector depth. The dashed curve (pion-only model) and the dotted curve (kaon-only model) are given by Eq. 6.18. The black curve is given by Eq. 6.17 including both kaon and pion models. α_T value (blue dot) from DC:NASA is more consistent with the theoretical prediction than DC:ECMWF. The data from other experiments are shown for comparison, and they are from the Borexino[112].

Table 6.7. These uncertainties are estimated by the deviation of the predicted α_T. $\cos\theta$ is not considered in this list, and the uncertainty of $\langle E_{th}\rangle$ is from 10^7 muon generated samples. The value of $\langle\alpha_T\rangle$ from 10^7 generated samples is $\langle\alpha_T\rangle_P = 0.461 \pm 0.014$.

From Adamson et. al study[4] and Table 6.7, The K/π ratio in the atmosphere affects the value of α_T. However, the K/π ratio cannot be determined directly. Finding the

Table 6.7: Systematic errors of the predicted temperature coefficient.

Parameter	$\Delta\alpha_T$
$r_{K/\pi}$	0.012208
$\langle E_{th}\rangle$	0.00124
γ	0.004501
ε_K	0.00024
ε_π	0.005247
total	0.014
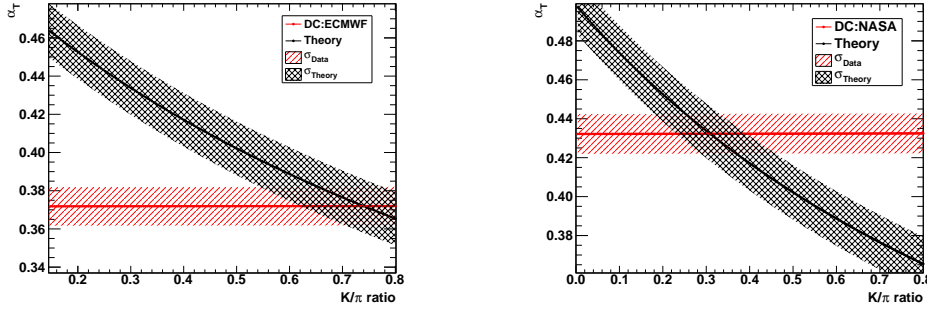
(a) The Double Chooz experimental α_T (from DC:ECMWF) as a function of K/π ratio

(b) The Double Chooz experimental α_T (from DC:NASA) as a function of K/π ratio

Figure 6.28: (a) The α_T from DC:ECMWF as a function of k/π ratio (red dots) with its error is indicated by the hatched region, and the theoretical $alpha_T$ (black dots) with its error is indicated by the cross-hatched region. (b)The α_T from DC: NASA as a function of the k/π ratio (red dots) with its error is indicated by the hatched region, and the theoretical α_T (black dots) with its error is indicated by the cross-hatched region. The statistic and systematic errors of measurement are from Table 6.7, Figure 6.26a, and Figure 6.26b. The theoretical error is from 10^7 generated samples and Table 6.7.

intersection of the theoretical curve and the experimental curve from the Adamson et. al study[4] is applied to search for the k/π ratio of Chooz local atmosphere as well. Figure 6.28a and Figure 6.28b show the experimental and theoretical α_T with 1 σ error as the functions of K/π ratio from the DC:ECMWF and the DC:NASA.

α_T is generated by a Gaussian distribution[113] with the sigma (= error from the previous results). For the experimental comparison, the mean of the Gaussian distribution is the α_T from DC:NASA or DC:ECMWF, For theoretical comparison, the mean of the Gaussian

(a) Minimization of χ_2 test(DC:ECMWF) to find the K/π ratio.

(b) Minimization of χ^2 test(DC:NASA) to find the K/π ratio.
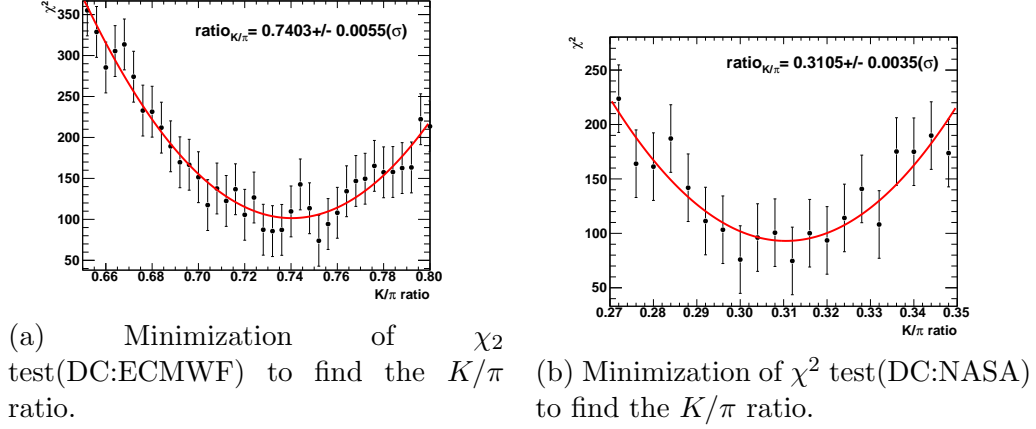
Figure 6.29: (a) The χ^2 value (the comparison between the DC:ECMWF experimental and theoretical histograms) as a function of K/π ration. The minimization of χ^2 at K/π ratio = 0.7403 ± 0.0055 is determined by a Parabola fit (error from $\Delta\chi^2 = 1$). (b)The χ^2 value (the comparison between the DC:NASA experimental and theoretical histograms) as a function of K/π ration. The minimization of χ^2 at K/π ratio = 0.3105 ± 0.0035 is determined by a Parabola fit (error from $\Delta\chi^2 = 1$). The error of each point is equal to 31.04, which is determined by the biggest uncertainty, T_{eff}.

distribution is the $\langle \alpha_T \rangle$ from 10^7 generated samples from Eq.6.17. The histogram of α_T distribution from the theoretical prediction should be re-scaled by the area of the experimental α_T distribution. χ^2 test is use to determine the comparison of two histograms of data and prediction at the certain K/π ratio.[114] The χ^2 test used to analyze the study is a root application[113]. The χ^2 values as a function of K/π ratio from the χ_2 test are represented in Figure 6.29a (from DC:ECMWF) and Figure 6.29b (from DC:NASA). The χ^2 minimization is determined by a Parabola fit, and the error of the K/π ratio is estimated at $\Delta\chi^2 = 1$. The K/π ratio is equal to 0.3101 ± 0.0015 of DC:NASA data, and the K/π ratio is equal to 0.7404 ± 0.0025 of DC:ECMWF data.

The differences of K/π ratio between the prediction and the experiment are 51.9% from DC:NASA, and 79.8% from DC:ECMWF. The χ^2 test considers the discrepancy of the shapes of histograms; therefore, the χ^2 value is over 100 in Figure 6.29a and Figure 6.29b. We can define another χ^2 as

$$\chi^2 = \frac{(\alpha_{exp} - \alpha_{th})^2}{\delta_{exp}^2 + \delta_{th}^2}. \tag{6.19}$$

101
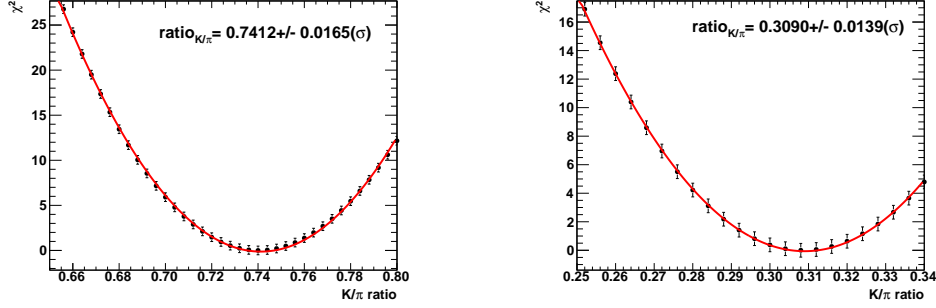
(a) New χ^2 (From DC:ECMWF) mini-mization to find the K/π ratio.

(b) New χ^2 (From DC:NASA) mini-mization to find the K/π ratio.

Figure 6.30: (a) The new χ^2 value (from DC:ECMWF) as function of K/π ration. The minimization of χ^2 at $K/\pi = 0.7412 \pm 0.0165$, is determined by a Parabola fit (error from $\Delta\chi^2 = 1$). (b)The new χ^2 value (from DC:NASA) as function of K/π ration. The minimization of χ^2 at $K/\pi = 0.3090 \pm 0.0139$, is determined by a Parabola fit (error from $\Delta\chi^2 = 1$). The error of each point χ^2 is 0.48, which is determined the largest uncertainty, T_{eff}.

The new χ^2 as a function of K/π ratio is shown in Figure 6.30a and Figure 6.30b. Following the new χ^2 definition, the K/π ratio from DC:NASA is 0.3090 ± 0.0139, and from DC:ECMWF is 0.7412 ± 0.0165.

The K/π ratio does not consistent with the previous experiments' results, K/π ratio $= 0.149 \pm 0.694$,[111] due to the estimation of threshold muon energy. In the Double Chooz experiment, the moun energy is unmeasurable. Instead, we apply the theoretical threshold muon energy to the T_{eff} and the predicted $\langle \alpha_T \rangle_P$. From Eq. 6.17, the $\langle \alpha_T \rangle_P$ is very sensitive to $\langle E_{th} \rangle$. Figure 6.31 shows the $\langle \alpha_T \rangle_P$ from the experiment and the prediction as the functions of $\langle E_{th} \rangle$. (assuming the K/π ratio $= 0.149$).[111] From Figure 6.31, the minimization of E_{th} in the cross-hatched area is smaller than $0.1180 \pm .0002$ TeV from the $\langle E_{th} \rangle$ of muon intensity. We can find the $\langle E_{th} \rangle$ at the cross-hatched region in Figure 6.31 by the minimization of χ^2 as well. The minimization of the χ^2 is at 105.8 ± 0.3 GeV shown in Figure 6.32. The difference between the prediction from the $\langle E_{th} \rangle$ of muon intensity and result from the minimization of χ^2 is 10.33 %.
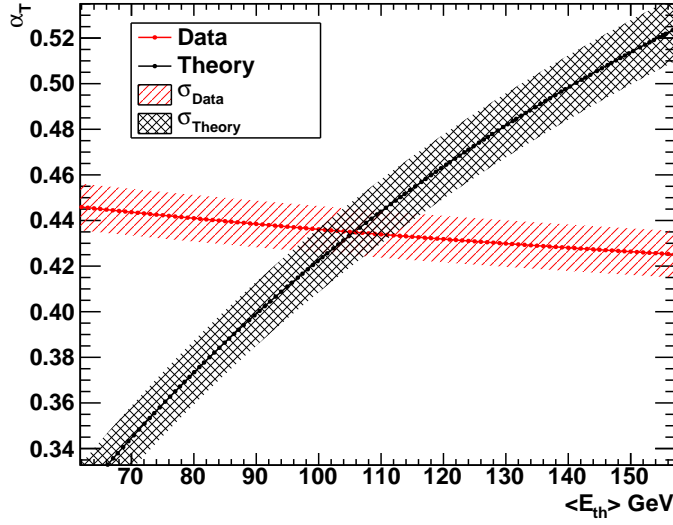
Figure 6.31: The experimental α_T (from DC:NASA) as a function of $\langle E_{th} \rangle$ (red dots) with its error is given by the hatched region, and the theoretical α_T (black dots) with its error is given by the cross-hatched region.

6.3.4 Results of Temperature Coefficient and K/π Ratio

The 334-day data of the valid muons have been collected by the Double Chooz far detector. We compared the daily muon rate with the daily effective temperature with two data sets, DC:NASA and DC:ECMWF. The correlation between the T_{eff} and the muon rate shows: 1) α_T (DC:ECMW) = 0.372 $\pm$ 0.001 (stat.) $\pm$ 0.009 (syst.), and 2) α_T (DC:NASA)= 0.432 $\pm$ 0.002 (stat.) $\pm$ 0.010 (syst.). The theoretical prediction, $\langle \alpha_T \rangle_P$ = 0.461 $\pm$ 0.014, is closer to the result of DC:NASA, and their difference is 6.290%. The small structures of the $\Delta R_\mu / \langle R_\mu \rangle$ curve cannot match the ECMWF T_{eff} curve very well (see Figure 6.21), and this can cause the low α_T from the result of DC:ECMWF. These small structures were from the weather change in short period time. It will be averaged by a long term experiment.

The K/π ratio is equal to 0.3101 $\pm$ 0.0015 from the DC:NASA. The difference is 51.9% away from the previous experiments, K/π = 0.149 $\pm$ 0.06[111]. It can be reasoned that we overestimate the $\langle E_{th} \rangle$ from the theoretical muon intensity. The muon intensity model, Eq. 6.4, cannot describe the muon energy correctly. The topographic feature near Chooz
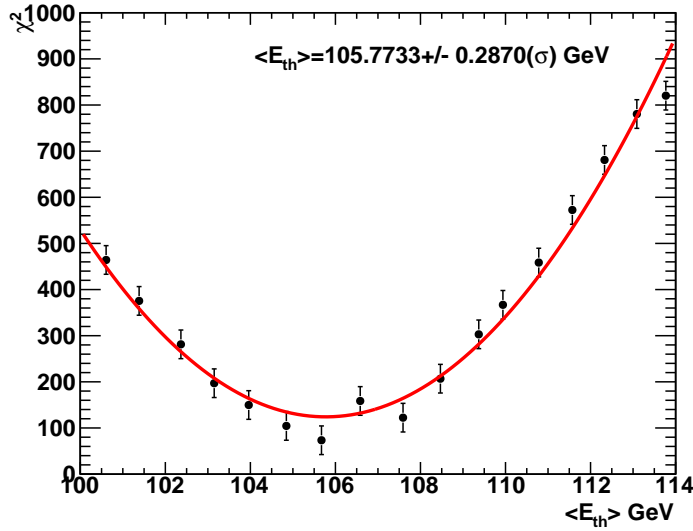
Figure 6.32: The χ^2 (DC:NASA) as a function of $\langle E_{th} \rangle$. The minimization of χ^2 at $< E_{th} >=$ 105.8 ± 0.3 GeV is determined by a Parabola fit (error from $\Delta\chi^2 = 1$).

should be considered into the muon intensity model as well. The simple test provides that the theoretical $\langle E_{th} \rangle$ is equal to 105.8 ± 0.3 GeV when we assume $\gamma_{K/\pi} = 1.49$. It it a 10.33 % difference between the prediction from theoretical muon intensity and the result of the minimization of χ^2. At the depth at 300 MWE, the high the $\langle E_{th} \rangle$ affects the K/π ratio and $\langle \alpha_T \rangle$ seriously. A precise simulation can improve the $\langle E_{th} \rangle$, and it should be included the orientation of the muon, the topographic feature of experimental hall, the OV muon detective efficiency, and the simulation of the surface muon intensity in the Double Chooz far detector in the future.

Chapter 7

Antineutrino Oscillation Analysis

7.1 Antineutrino Candidates

The Double Chooz oscillation analysis includes the $\overline{\nu}_e$ rate and spectral shape.[5] The IBD candidates are valid for the selection. The selection consists of several cuts listed below:[5,86]

1) the triggers valid for $E_{vis} > 0.5$ MeV due to the trigger efficiency[72,86] and for the light noise cuts ($Q_{max}/Q_{tot} < 0.09$ and rms ($t_{start} < 40$ ns));

2) in the 1-ms window after a tagged muon ($E_{vis} > 5$ MeV in the IV or > 30 MeV in the ID);

3) dT, the time difference between the prompt and delayed triggers, in the interval 2 $\mu s < dT < 100$ μs;

4) prompt triggers valid for the energy range, 0.7 MeV $< E_{prompt} < 12.2$ MeV;

5) delayed triggers valid for the energy range, 6.0 MeV $< E_{delayed} < 12.0$ MeV, and the strict light noise cuts, $Q_{max}/Q_{tot} < 0.055$ and rms ($t_{start} < 40$ ns);

6) no trigger after the delayed trigger from 100 μs to 400 μs. (the multiplicity condition);

7) the prompt trigger not equal to the OV signal simultaneously.

There are extra selections, which did not be included in the Double Chooz first publication[5]:

1) showering muons tagged by the deposited energy in ID > 600 MeV and dT with respect to the last showering muon less than 0.5 s. (increasing 9.2% the efficiency of the

veto time)[5];[86]

2) the prompt trigger not an OV trigger coincidentally.[86]

Figure 7.1 shows the dT distribution for IBD candidates, and Figure 7.2 shows a two-dimensional mapping plot of the delayed triggers versus the prompt triggers. Figure 7.3[115]
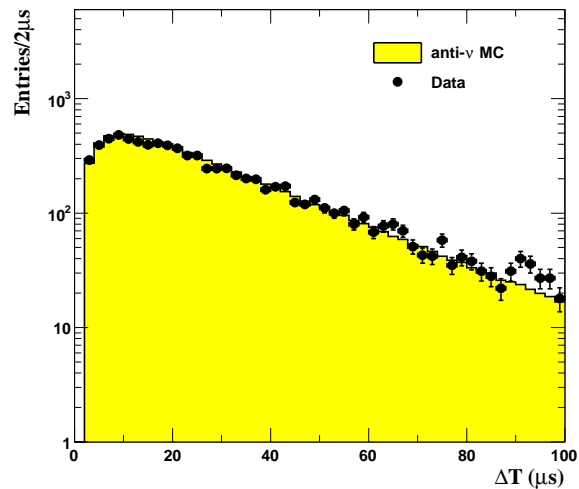
Figure 7.1: The time difference between prompt and delayed triggers for the data (black dot) and the Monte Carlo prediction (yellow fill area). The plot is from the second publication of the Double Chooz Collaboration.[5]

shows the daily $\overline{\nu_e}$ rate as a function of the elapsed day. There are total 8249 candidates (rate = 36.2 ± 0.4 events/day) and the live time is 227.93 days.[116] The Monte Carlo signals are generated by Equation 4.2. The input information of the $\overline{\nu_e}$ production are neutrino energy spectra and the fission products in the reactor.[56] Each IBD-progenitor $\overline{\nu_e}$ is assigned at random vertex, and the reaction opportunity is based on the density of the proton of the detector (the the random weight function of the interaction in the detector).[5] The direction of the positron of the IBD is assigned randomly too. The momentums of the positron and neutron from the IBD obey the energy and momentum conservations. The vertex and energy of the positrons and the neutrons are the input of the Geant4 simulation.[5] The total number of the predicted $\overline{\nu_e}$ from the Monte Carlo simulation is equal to 8439.6.[5]
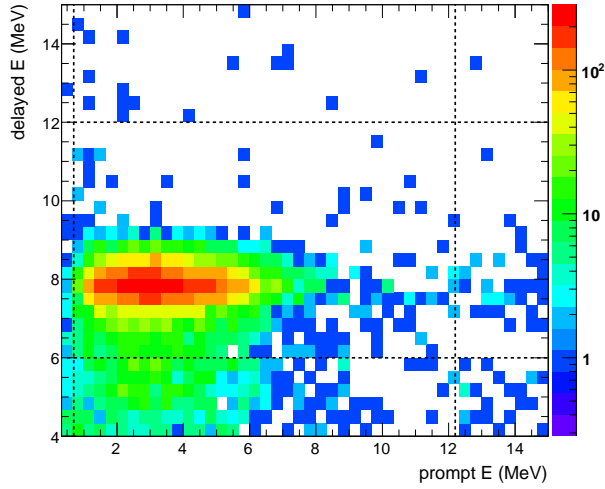
Figure 7.2: Two-dimensional energy mapping for the delayed triggers versus the prompt triggers. The dashed lines are the selection of delayed and prompt triggers: 6 MeV < $E_{delayed}$ < 12 MeV, and 0.7 MeV < E_{prompt} < 12.2 MeV. The plot is from the second publication of the Double Chooz Collaboration.[5]

7.2   Background

The Double Chooz experiment obtains three kinds of backgrounds: the accidental background, the cosmogenic isotopes background, and the fast neutron and stopping muon. This section introduces each background study respectively, and most results are taken from the Double Chooz second publication[5].

The accidental background is from the natural radioactive source mimicking prompt signals and the neutron-like events mainly from Gd-capture events. The background events are selected by the $\overline{\nu_e}$ selection in Chapter 7.1. Nevertheless, we have defined an off-time method to identify the accidental background to avoid the correlation of neutron captures on H and Gd. The time coincidence windows of the off-time method is listed below:[117]

1) the virtual prompt event: 198 off-time windows, $1\ ms+500\ \mu s \times NW$ ($NW = 0 \sim 197$), after the prompt candidate;

2) the delayed candidate: the 2-100 μs window after that virtual prompt.
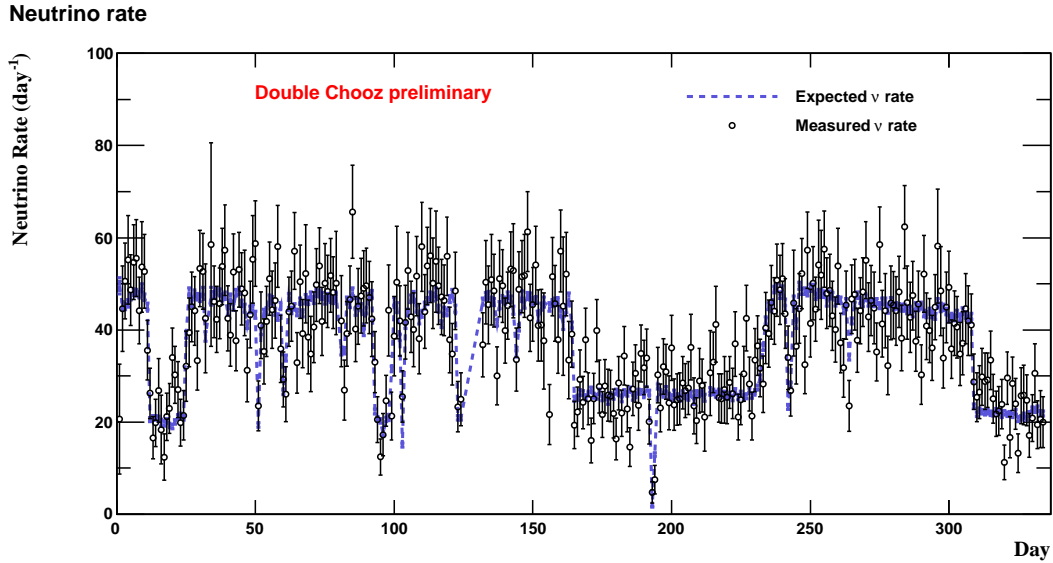
Figure 7.3: The $\overline{\nu_e}$ daily rate of the data (black circle) and Monte Carlo prediction (blue curve) as the functions of the elapsed day. This plot is from P. Novella, "Neutrino Candidates blessed plots for DC2ndPub", Double Chooz Document 4036.[115]

The accidental background rate is 0.261 ± 0.002 events/day.[117] The error is the statistical error, which is from the 30×198 coincidence windows. Figure 7.4 shows the accidental background of prompt signals, and the scaled natural radioactive spectra.

The cosmogenic isotopes background in the IBD search is from the βn-decays of the radioactive isotopes, ^{9}Li and ^{8}He. These radioactive isotopes are the products of the cosmic muon or the interactions of the muon's shower particles with the liquid scintillator, mainly ^{12}C nuclei.[118] Based on the isotope's time, space, and correlation to its parent muons, the IBD selection can discriminate βn-decays from the $\overline{\nu_e}$ signals. However, it is hard for the IBD selection to distinguish each βn-decay existence due to its long lifetime. In the veto system, these signals produce a large loss based on the different isotopes' lifetimes. It is the reason that the muon rate cannot be counted directly. Therefore, the muon rate is estimated by the best fit of the exponential function of the time, $\Delta t_{\mu\nu} \equiv t_\mu - t_\nu$, between the tagged muon and the $\overline{\nu_e}$.

The cosmogenic isotopes background performs three visible energy ranges corresponding with the different volumes. There is a spatial cut to avoid the uncorrelated pair of the
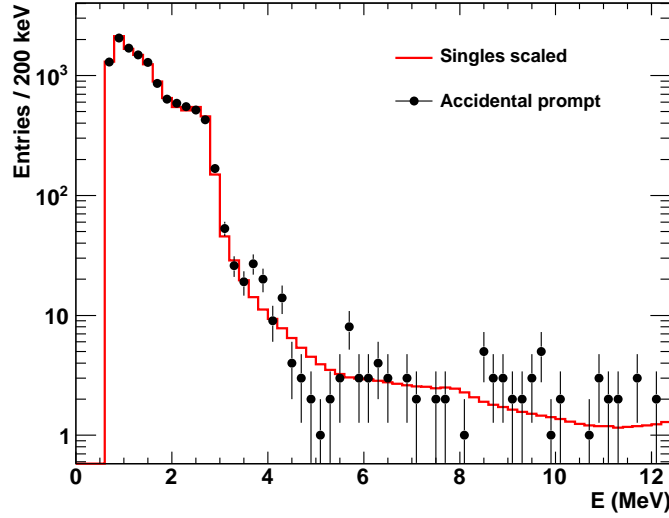
Figure 7.4: This plot shows the accidental background and the natural radioactive-scaled spectrum of the Double Chooz experiment. The plot is from the second publication of the Double Chooz Collaboration.[5]

muon and the IBD events. The distance of spatial cut is defined as $d_{\mu\nu} < 80$ cm. The first energy range is located at $E_\mu^{vis} > 600$ MeV, a high energy range, and this selection is for the showering muons crossing the NT. There is no spatial cut necessarily because of a little dependence with a showering muon at the high energy range. The βn-emitter rate is 0.95 ± 0.11 events/day from the $\Delta t_{\mu\nu}$ exponential fit. The second energy range is locate at $275 < E_\mu^{vis} < 600$ MeV, and the muons cross the NT and the GC. The spatial cut is applied in the analysis. The production rate is 1.08 ± 0.36 (stat.) ± 0.25 (syst.) events/day. The last energy range is located at $E_\mu^{vis} < 275$ MeV, and the muons cross only the buffer volume or the rim of the GC. The spatial cut is applied in this condition, and the rate is smaller 0.3 events/day from a exponential fit. The total βn-decay rate combined three energy ranges is $2.05^{+0.62}_{-0.52}$(stat.) ± 0.26(syst.) events/day. The ratio of the ^{8}He in ^{9}Li sample is provided from the KamLAND result.[119] The systematic uncertainty includes the slope of the uncorrelated background spectrum, the bin width of the spectrum, and the efficiency of the spatial cut.[119] The background from the isotopes related to the showering muons is evaluated by the selection, the valid trigger in 0.5 s window after the tagged muon ($E_{vis} >$

600 MeV). The cosmogenic isotope rate, 0.89 ± 0.10 events/day, is removed from the data.[120] The rate of the remain cosmogenic isotope background is equal to 1.25 ± 0.54 events/day in the IBD data. The sample spectrum can be seen in Figure 7.5.
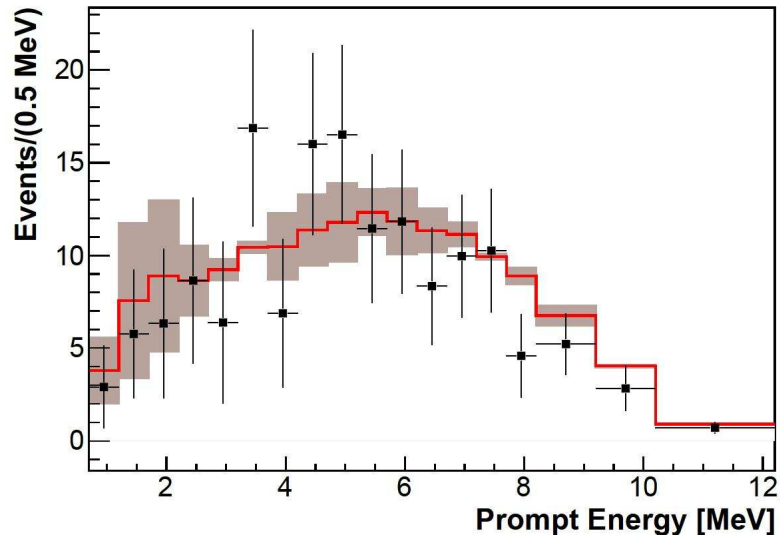
Figure 7.5: The prompt spectrum of the cosmogenic isotope background from ^{8}He and ^{9}Li. The red line is from Monte Carlo prediction, and the black dots are from the data. The plot is from the second publication of the Double Chooz Collaboration.[5]

The correlated background can be usually tracked by its parent muon in a 1-ms veto window. The remain background is produced by the missed muons or the low energy muon deposited in the detector. These events can be observed by the stoping muons (SM) and the fast neutrons (FN). These muons interact the outside part of the detector and produce the FN. They can cross the whole detector and be captured in the ID. The background can mimic the prompt triggers by the recoiling protons, and with the delayed triggers, the Gd-capture signals. The FN selection is base on the official $\overline{\nu_e}$ selection. The additional cuts are listed below:[121]

1) prompt trigger, 0.5 MeV $< E_{vis} < 30$ MeV;

2) dT > 10 ns;

3) the multiplicity of IV PMT ≥ 2;

4) $d_{prompt-delayed} < 150$ cm (remove gamma-gamma events);

5) rejection of the pair of one IV gamma and one neutron event.

Fast neutrons are determined by a low energy IV tagging (IV threshold ~ 1 MeV), which relies on the multiplicity of the IV PMT hit.[121] The hits are from the detection of H-capture signals and proton recoils. The additional cuts can reject the gamma-gamma events, the $\overline{\nu_e}$ events, and the IV gamma/neutron background.

The SM events enter into the ID through the chimney. Then, the SM stops and decays on the top of the ID. The SM tracks can mix with the prompt signals, and the Michel electrons[1] can mix with the delayed signals. However, this prompt-delayed couple signal has a short dT, the 2.2 μs muon lifetime. The SM selection cuts are base on the official neutrino selections. The additional cuts are listed below:

1) muon tagging: $E_{IV} > 5$MeV and $E_{ID} > 60$ MeV;

2) prompt signals: $0.5 < E_{prompt} < 30$ MeV and $Q_{max}/Q_{tot} < 40$;

3) delayed signals: 20 MeV $< E_{delayed} < 60$ MeV;

4) dT > 10 ns.

The SM is determined by a tagged high-energy Michel electron after the muon decay. The light noise at the high energy can be reduced by raising the Q_{max}/Q_{tot} value. The OV tagging is sensitive to the SM because the OV usually can catch muons. In the energy range, $12 < E < 30$ MeV, of the FN and the SM study, the muons are tagged by the OV system. ($74 \pm 12\%$ is FN.) The OV system can avoid $< 0.6\%$ accidental background from the $\overline{\nu_e}$ candidates.

The FN rate from the experiment is 0.30 ± 0.14 events/day included the systematic uncertainty from the dT separation of the FN and the SM, the background subtraction, and the IV tagging efficiency. The SM and FN shape are very close to a linear model. The FM and SM spectra are shown in Figure 7.6, and the total rate is equal to 0.67 ± 0.20

---

[1]The Michel decay is the dominant mode of the muon.[122] The decays are:[122]

$$\mu^- \rightarrow e^- + \overline{\nu_e} + \nu_\mu; \tag{7.1}$$

$$\mu^+ \rightarrow e^+ + \overline{\nu_\mu} + \nu_e; \tag{7.2}$$

events/day.
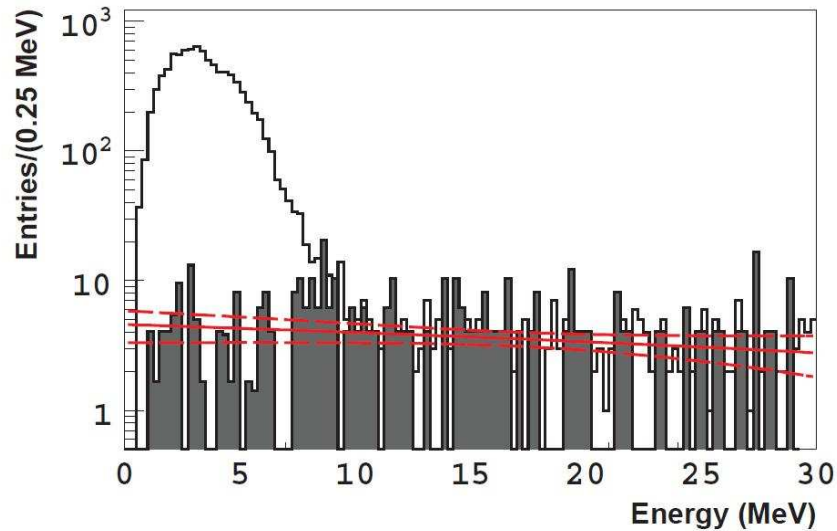
Figure 7.6: This plot shows the spectra of the FN, the SM and the best fit. The gray histogram shows the NF and SM combined spectrum, and the black curve is the prompt spectrum of the IBD events. The best fit is indicated by a solid-red line with one σ (dashed-red line). The plot is taken from the second publication of the Double Chooz Collaboration.[5]

7.3   Neutrino Oscillation Analysis

This section introduces the fundamental method of $\sin^2 2\theta_{13}$ analysis using in the Double Chooz second publication.[5] The uncertainties included in the final analysis are introduced in this section. The potential uncertainties from the seasonal variation are obtained into the $\sin^2 2\theta_{13}$ analysis, and their influences of the result shows in the final part.

The data divides into two periods based on the reactor thermal power from EDF. The first period was in one reactor operating at $< 20\%$ of the nominal thermal power, and the other period was in the duration of both reactors running usually. The analysis is base on the combined analysis of the $\overline{\nu_e}$ spectral shape and its rate. The prompt spectrum divides into 18 unfixed bins between 0.7 and 12.2 MeV. The background study also corresponds with the two periods. The event number of each bin is denoted by N_i (i= 1 to 36), and there are total 36 bins. This method can investigate the ratio of the signal to the background

Table 7.1: Summary of the IBD candidates from the experiment.[5]

	Reactors Both on	One Reactor $P_{th} < 20\%$	Total
Livetime[days]	139.27	88.66	227.93
IBD Candidates	6088	2161	8249
ν Reactor B1	2910.9	774.6	3685.5
ν Reactor B2	3422.4	1331.7	4754.1
Cosmogenic Isotope	174.1	110.8	284.9
Correlated FN(SM)	93.3	59.4	152.7
Accidentals	36.4	23.1	59.5
Total Prediction	6637.1	2299.7	8936.8

in each reactor period. Additionally, the background spectra can be considered in the fit. Table 7.1[5] lists the numbers of the IBD candidate and livetime in two periods. A predicted spectrum of the signal and the background can be described by Eq. 7.3.[5]

$$N_i^{pred} = \Sigma_{R=1,2}^{Reactors} N_i^{\nu,R} + \Sigma_b^{Bkgands.} N_i^b$$

$$N_i^{\nu,R} = P(\overline{\nu}_e \to \overline{\nu}_e) N_i^{exp,R} \tag{7.3}$$

$N_i^{exp,R}$ is defined by Eq. 4.2[5]. The background obtains the accidental, cosmogenic isotope, and related backgrounds. R is the reactor, Chooz B1 or B2. Additionally the experimental background rate should be scaled by the Monte Carlo scale factor in Table 5.1 and livetime of each data-taking period.

A standard χ^2 function is defined as Eq. 7.4 to fit the binned signal and the background spectra. The parameter, $\sin^2 \theta_{13}$, can be estimated by the minimum of the χ^2 performed by Eq. 7.4.[5]

$$\chi^2(\sin^2 2\theta_{13}) = \Sigma_{i,j}^{36}(N_i - N_i^{pred}(\sin^2 2\theta_{13}))(M_{i,j})^{-1}(N_i - N_i^{pred}(\sin^2 2\theta_{13}))^T$$
$$+\frac{(\epsilon_{fast-n} - 1)^2}{\sigma_{fast-n}^2} + \frac{(\epsilon_{9Li} - 1)^2}{\sigma_{9Li}^2} + \frac{(\alpha_E - 1)^2}{\sigma_{\alpha_E}^2} + \frac{(\Delta m_{31}^2 - (\Delta m_{31}^2)_{MINOS})^2}{\sigma_{MINOS}^2}. \tag{7.4}$$

In the Eq. 7.4, $M_{i,j}$ is a covariance matrix consisting of 5 kinds of the uncertainties. The covariance matrix, $M_{i,j}$, is defined as:[5]

$$M_{i,j} = M_{i,j}^{sig.} + M_{i,j}^{det.} + M_{i,j}^{stat.} + M_{i,j}^{eff.} + \Sigma_b^{Bkgnds.} M_{i,j}^b. \tag{7.5}$$

Table 7.2: Summary of IBD event and background uncertainties in the $\sin^2 2\theta_{13}$ analysis. This table is taken from the Double Chooz collaboration.[5]

category	Uncertainty[%]
Reactor Flux	1.67%
Detector Response	0.32%
Statistics	1.06%
Efficiency	0.95%
Cosmogenic Isotope Background	1.38%
Correlated Background μ	0.51%
Accidental Background	0.01%
Total	2.66%

Table 7.3: MC Efficiency Correction

Parameter	Systematics uncertainty	scale factor
Gd-fraction correction and systematics	0.3%	0.985
dT-efficiency systematics	0.5%	1.000
E-containment-efficiency systematics	0.7%	1.000
Spill in/out	0.3%	1.000
Target H number	0.3%	1.000
total systematics	1.0%	0.985

The normalized background, detector response, and signal uncertainties are summarized in Table 7.2[5]. In Table 7.2, the uncertainties from the efficiency and the partial detector response are contributed from the sub-uncertainties listed in Table 7.3.[123] The uncertainties are normalized in the covariance matrixes. $M_{i,j}^{sig.}$ is a signal covariance matrix from the predicted IBD spectrum. The background covariance matrix, $\Sigma_b^{Bkgnds.} M_{i,j}^b$, obtains the ^{9}Li spectral shape uncertainty with the Monte Carlo model and the slope of the experimental nearly-flat FN spectrum. The accidental background uncertainty is in the diagonal term in the covariance due to its high statistics and the off-time window analysis.[5] From the Eq. 7.4, we have added four pull terms to scale some parameters. Additional background pull terms are ε_{fast-n} and $\varepsilon_{^9\text{Li}}$. The energy scale pull term can scale the energy linearly for the IBD events and the background based on α_E with the uncertainty σ_{α_E}. The final pull term is constrained in the MINOS measurement, $\Delta m_{31} = (0.32 \pm 0.12) \times 10^{-3}\text{eV}^2$. The

best fit from Eq. 7.4 is $\sin^2 2\theta_{13} = 0.109 \pm 0.030(\text{stat.}) \pm 0.025(\text{syst.})$[5] when Δm_{31} is equal to $(0.32 \pm 0.12) \times 10^{-3}\text{eV}^2$. The χ^2 is equal to 42.1/35.[5] The best fit and the measured spectra show in Figure 7.7.
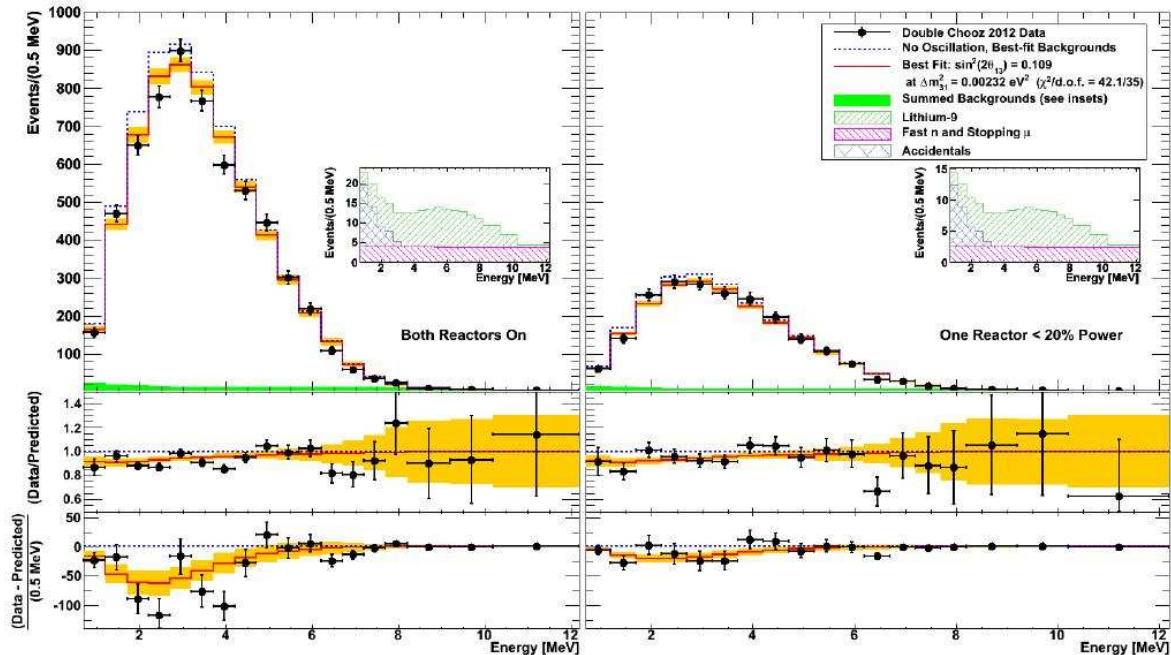
Figure 7.7: The experimental and expected prompt spectra in two integration periods are shown, and the two plots are from the Double Chooz second publication[5]. The plots include the experimental data, the Monte Carlo prediction without neutrino oscillation, the background spectrum, and the best-fit spectrum at $\sin^2 2\theta_{13} = 0.109$ and $\Delta m^2_{13} = 2.32 \times 10^{-3}$ eV^2. The inserted plots are the background spectra from ^{9}Li, FN/SM, and accidental events. In the middle two plots, the ratio of the data (background stacked) to the Monte Carlo prediction without neutrino oscillation (dots). The ratio of data to the best fit is indicated by a red curve. The systematic uncertainties is the orange band in the plots. The difference between the data (background stacked) to the Monte Carlo prediction without neutrino oscillation (dots) and difference between the prediction of the best fit and Monte Carlo prediction without neutrino oscillation (red curve) are performed in the bottom plots.

The confidence interval of $\sin^2 2\theta_{13}$ is based on the frequentist approach developed by Feldman and Cousins[124]. The confidence interval gives the range of the $\sin^2 2\theta_{13}$ in certain level. We consider the possible 21 test points, which are possible $\sin^2 2\theta_{13}$ values (0 to 0.25).[125] 10000 experiments (as well as the number of the Double Chooz IBD candidates) are generated by these test points. The survival IBD events from the generation

115

are based on the Double Chooz experiment design and the data-taking time, and then we add a random fluctuation into the energy bins in the covariance matrix. The χ^2 function in Eq. 7.4 is used to fit the spectrum of each test experiment. The $\Delta\chi^2$ is defined as the difference between the χ^2 of each test point (the $\sin^2 2\theta_{13}$ fixed) and the the best-fit result (the best result of $\sin^2 2\theta_{13}$) from the generations. Two confidence intervals are considered, 90 % and 68 %. The $\Delta\chi^2_{critical}$ is defined as the $\Delta\chi^2$ in the 90% (or 68%) of the $\Delta\chi^2$ distribution. The other parameter, $\Delta\chi^2_{data}$, is the difference between the χ^2 of the best-fit result of the real Double Chooz data and the χ^2 of the test experiment. The $\Delta\chi^2_{critical}$ curves and $\Delta\chi^2_{data}$ curve show in Figure 7.8[125]. The following confidence intervals are list below:

$0.044 < \sin^2 2\theta_{13} < 0.17$ at 90% CL.;[5,125]

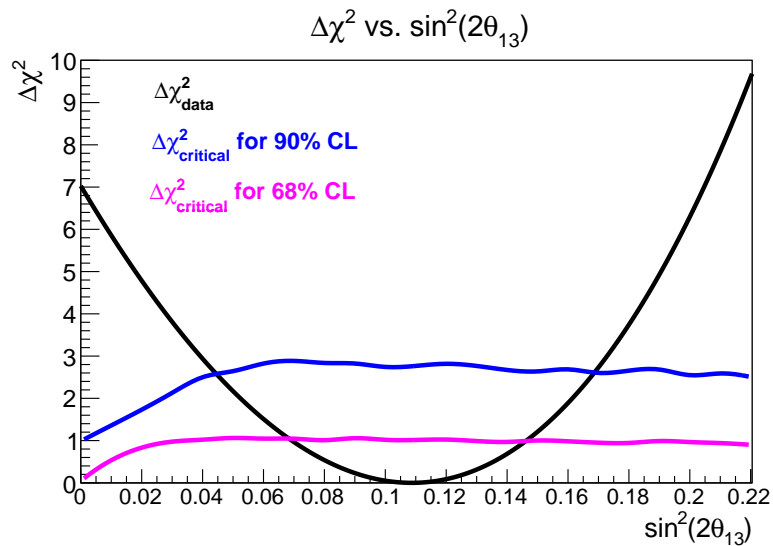$0.068 < \sin^2 2\theta_{13} < 0.15$ at 68% CL.[5,125]

Figure 7.8: This plot is provided from R. Carr et al.[125]. $\sin^2 2\theta_{13}$ confidence intervals in 90% and 68% CL in the Double Chooz publication[5]. The valid ranges are located at $\Delta\chi^2_{critical} > \Delta\chi^2_{data}$ in 68% (magenta) and 90% (blue).

7.4 Search for Seasonal Effect on IBD Candidates

The seasonal variation of the Double Chooz detector is discussed in Chapter 6, and its influence of the Double Chooz detector shows in the bias of the IBD daily rate and the instability of the neutron efficiency measured in different times. The seasonal effect on the IBD candidates, which can changed the result of $\sin^2 2\theta_{13}$ analysis, can be observed in the distribution of the normalized IBD daily rate. The normalized IBD rate is the ratio of the IBD rate from the data to the Monte Carlo prediction. This ratio avoids the change of the reactor thermal power. The liquid temperature of the GC is used to determine the temperature change in the NT because there is no sensors in the NT in order to purify the Gd-capture signals. Figure 7.9a shows the normalized IBD rates of data and Monte Carlo prediction (average over every 20 days) as the functions of the GC temperature. The average IBD rates of the experiment and Monte Carlo prediction are 0.952 ± 0.010 and 1.000 ± 0.001 respectively (see Figure 7.9a). The normalized daily IBD rate and GC liquid temperature are shown in Figure 7.9b. The normalized daily IBD rate can be described by a linearity plus a sine function from the seasonal influence:

$$y = a + b\sin(\frac{2\pi t}{365} + c), \tag{7.6}$$

Building upon the Eq. 7.6, y is the normalized IBD rate at a certain time, t. The average IBD rate, a, is from the best fit of the linearity. The parameter, b, is the intensity of seasonal influence, and the parameter, c, is a phase term of the seasonal variation. The best fit of Eq. 7.6 shows results of the intensity of the sine function, 0.012 ± 0.013, and the average normalized IBD rate, 0.907 ± 0.010. The seasonal influence from the intensity of the best fit is negligible in the normalized IBD rate.

The instability of the neutrino detection efficiency is another potential factor influencing the $\sin^2 2\theta_{13}$ analysis. The relative instability of the energy reconstruction[5] has been included into the $\sin^2 2\theta_{13}$ analysis. We can consider a relative instability uncertainty from the neutron detection efficiency as well. The relative instability in the neutron detection
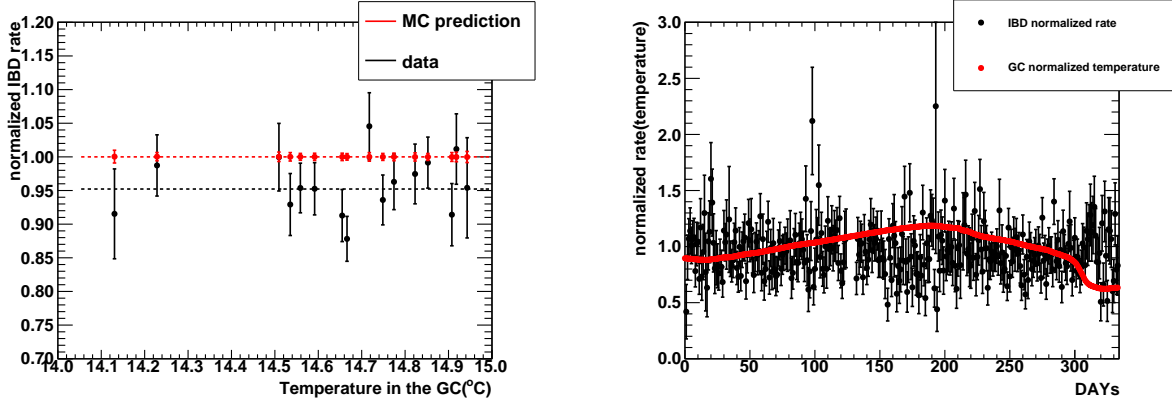
(a) The IBD rate vs. GC temperature   (b) The normalized IBD rate vs. data-taking day.

Figure 7.9: (a) The IBD normalized daily rate of the measurement and Monte Carlo prediction as the functions of the GC liquid temperature. Each point on this plot is averaged over the 20 daily measurements. This plot shows that the liquid temperature is not related to the IBD candidates. The systematic uncertainties on the experiment and Monte Carlo prediction are estimated at 1.1% and 0.1% respectively. (b) The strains of the normalized daily IBD rate and the liquid temperature in 334 elapsed days. The seasonal change can be observed from the GC liquid temperature (red dots).

efficiency can be observed by the deviation as a function of the elapsed days. In the energy reconstruction, we has included the relative instability, 0.61% from Figure 4.5 into the total energy scale systematic error[5]. Building upon the neutron detection efficiency, the relative instability can be contributed by the bias of the three factors of the neutron detection efficiency. The Gd-capture fraction is evaluated by the error of the difference between the first ^{252}Cf calibration in May 2011 and the second calibration in June 2012. The difference is defined as:

$$deviation = (1st - 2st)/1st \tag{7.7}$$

The difference of Gd-capture fraction is $0.04 \pm 0.22\%$ from two calibrations. The instability of the Gd-capture fraction is equal to 0.04%. The instability of dT efficiency is evaluated by the difference of two calibrations, too. The dT difference from calibration runs is 0.10 $\pm$ 0.33 %. In order to consider the IBD influence, we can apply the IBD candidates to the dT efficiency definition from Eq. 5.9. This influence also concerns the possibility change of neutron captures on the Gd in the seasonal variation in Chapter 6.2. Sine the IBD

118

candidates are total 8249 events in 334 data-taking days, we average the dT efficiency over every 40 days to increase the statistics. The relative instability of the dT efficiency from the IBD candidates is shown in Figure 7.10. The systematic uncertainty of Figure 7.10 is
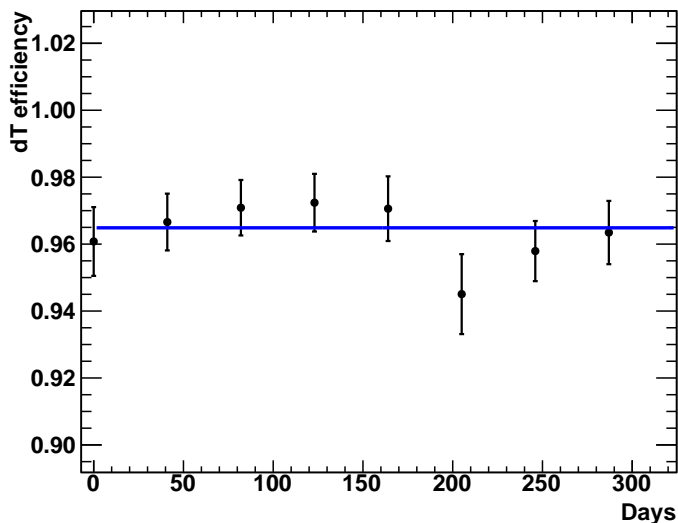
Figure 7.10: The relative instability of the dT efficiency as sampled by the evolution in response of the IBD candidates. The IBD candidates has been subtracted the background, and the observed steps correspond to every 40 days. The mean is 0.96 ± 0.02(blue line).

equal to 0.70%. The final dT systematic uncertainty of the relative instability is 0.16% weighted by the event numbers. (average 40-day IBD candidates: 412 events, and the ^{252}Cf calibration: 3818 events, $0 < \text{dT} < 200 \ \mu s$.) The energy containment efficiency instability has been included into the relative instability of the energy reconstruction already. Building upon Chapter 6.2, the proton number in the NT waves with the seasonal variation, and its uncertainty is equal to 4.69×10^{-6}%. The effect from the uncertainty of the proton number in the NT is negligible in this study. The relative instability systematic uncertainties of neutron detection efficiency and the uncertainty of the proton number due to the seasonal variation are included into the Table 7.3, and the new table are shown in Table 7.4.

In Table 7.4, the scale factor of the Monte Carlo simulation does not be affected by the additional uncertainties. Including additional uncertainty from the neutron detection efficiency, the result of final analysis is equal to $\sin^2 2\theta_{13} = 0.109 \pm 0.030$(stat.) ± 0.025(syst.).

Table 7.4: MC Efficiency Correction plus instability systematic uncertainties.

Parameter	Systematics uncertainty	scale factor
Gd-fraction correction and systematics	0.3%	0.985
dT-efficiency systematics	0.5%	1.000
E-containment-efficiency systematics	0.7%	1.000
Spill in/out	0.3%	1.000
Target H number	0.3%	1.000
Gd-fraction instability	0.004%	1.000
dT instability	0.16%	1.000
Target H number(seasonal variation)	4.69×10^{-6}%	1.000
total systematics	1.0%	0.985

The seasonal variation and the instability of the neutron detection efficiency do not change the final result of $\sin^2 2\theta_{13}$ in the Double Chooz second publication[5]. The detector is in reliable status in the past two years. This uncertainty of the IBD rate and neutron detection efficiency is a directions and an effect for the investigation when the instability is a concern in the future IBD study.

Chapter 8

Summary

In the past two years, our group, Double Chooz collaboration, has published two results of $\sin^2 2\theta_{13}$. The newest result from the Double Chooz experiment is $\sin^2 2\theta_{13} = 0.109 \pm 0.030$(stat.) ± 0.025(syst.). We have corrected the statistical and systematical errors of the $\sin^2 2\theta_{13}$, and we have also improved the CL from 94.6% to 99.9% away from the no-oscillation hypothesis. Our most important contributions are in reducing background and detector systematic uncertainties. This dramatic improvement is due to the precise calibration and specific background studies.

In the calibration issue, the strict light noise rejection and the new energy reconstruction including the detector calibration map, the linear PE calibration, and the stability enhance the energy scale status. It can be reasoned that the Monte Carlo prediction is much closer to the real detector responses. Furthermore, the neutron detection efficiency, the largest uncertainty in the detection efficiency, benefits by the improvements, too. In this study, we have seen successful in estimating the neutron detection efficiency with ^{252}Cf, which is one of the calibration goals. The Gd-capture fraction from the IBD events has confirmed the result from ^{252}Cf, and it can be reasoned that the ^{252}Cf study is trustworthy for the neutron detection efficiency of IBD. The Monte Carlo scale ratio is enhanced mainly also.

In the background study, the efforts should be based on not only the methods of the

data analysis but also the stable detector for the past two years. Specifically, the accuracy of the background relies on a long experimental period of time. This thesis provides several pieces of evidence to prove the stability of the detector. First, the detector's physical quality does not depend on the seasonal variation. The physical property of the detector can be reflected by the IBD rate, and the temperature of the liquid scintillator is affected by the seasonal change directly. There is no correspondence between the IBD rate and the liquid temperature. Second, the measured muon rate has a high correspondence with the local atmospheric temperature, and the ratio of K to π in the local atmosphere can be determined by this measurement. The detector observes the seasonal change of the products from the meson decays in the local atmosphere.

Finally, we add the instability systematic uncertainty from the detection neutron efficiency and the uncertainty from the proton number of the NT due to the temperature variation in the final analysis of the $\sin^2 2\theta_{13}$ result. According to the original three factors in the neutron detection efficiency, the dT and Gd-capture fractions include the new systematic uncertainty of instability, 0.16%, and the dT instability systematic uncertainty has been considered in the IBD instability throughout the entire experiment. The $\sin^2 2\theta_{13}$ result is not affected by the new uncertainty. The new instability systematic uncertainty indicates a direction and an effect when the instability of the detector is a concern of the Double Chooz experiment in the future.

Chapter 9

Contributions

In this dissertation, I describe my research and other related studies accomplished by other collaborators of the Double Chooz collaboration. I am writing to express my contributions in the Double Chooz experiment.

In terms of the neutron detection study with ^{252}Cf and IBD, I did the data analyses to estimate the efficiencies, the uncertainties, and the Monte Carlo scale factor. In terms of the Double Chooz physical environment monitoring system, I made the sensor assemblies covered by epoxy, and the development of the control software. I also did the circuit test, the partial installation, and the sensor calibration. In terms of the seasonal variation of the Double Chooz detector, I did the analyses of the correspondence between the muon rate and the atmospheric effective temperature and the ratio of kaon to pion of the local atmosphere, and I also generated the the muon intensity from the theoretical equation. In terms of the instability systematic uncertainty, I estimated the instability systematic uncertainties from the detection neutron efficiency and the proton number of the NT. I also added this instability systematic uncertainties into the $\sin^2 2\theta_{13}$ analysis to prove that the instability systematic uncertainties from the neutron detection efficiency and the proton number do not affect the $\sin^2 2\theta_{13}$ analysis.

Bibliography

[1] Y. Abe et al., Phys. Rev. Lett. **108**, 131801 (2012).

[2] D.Shrestha, *Estimating the neutron background toward the measurement of neutrino mixing angle* θ_{13} *with the Double Chooz detector*, PhD thesis, Kansas State University-2013, 2013.

[3] E. W. Grashorn et al., Astropart.Phys. **33**, 140 (2010).

[4] P. Adamson et al., Phys. Rev. D **81**, 012001 (2010).

[5] Y. Abe et al., Reactor electron antineutrino disappearance in the double chooz experiment, http://arxiv.org/abs/1207.6632, 2012, (PRD, 86 ,052008).

[6] C. Cowan, F. Reines, F. Harrison, H. Kruse, and A. McGuire, Science **124**, 103 (1956).

[7] F. Reines and C. Cowan, Nature **178**, 446 (1956).

[8] C. S. Wu, E. Ambler, R. W. Hayward, D. D. Hoppes, and R. P. Hudson, Phys. Rev. **105**, 1413 (1957).

[9] R. J. Davis, Phys. Rev. **97**, 766 (1955).

[10] R. J. Davis, Phys. Rev. Lett. **12**, 303 (1964).

[11] M. Goldhaber, L. Grodzins, and A. W. Sunyar, Phys. Rev. **109**, 1015 (1958).

[12] G. Danby et al., Phys. Rev. Lett. **9**, 36 (1962).

[13] D. Collaboration, Phys. Lett. B **504**, 218 (2001).

[14] H. V. Klapdor, *Neutrinos*, Springer-Verlag Berlin Heidelberg, 1988.

[15] B. Pontecorvo, Zh. Eksp. Teor. Fiz **33**, 549 (1957).

[16] V. Gribov and B. Pontecorvo, Phys. Lett. B **28**, 493 (1969).

[17] V. Varger, P. Langacker, and L. P. Leveille, Phys. Rev. Lett. **45**, 692 (1980).

[18] Z. Maki, M. Nakagawa, and S. Sakata, Prog. Theor Phys. **28**, 870 (1962).

[19] M. Apollonio et al., Eur.Phys.J.C **27**, 331 (2003).

[20] H. Minakata, H. Sugiyama, O. Yasuda, K. Inoue, and F. Suekane, Phys. Rev. D **68**, 033017 (2003).

[21] A. J. Franke, *Estimating the neutron background toward the measurement of neutrino mixing angle theta13 with the Double Chooz detector*, PhD thesis, Columbia University-2012, 2012.

[22] C. Bemporad, G. Gratta, and P. Vogel, Rev. Mod. Phys. **74**, 297 (2002).

[23] OHEP, Excerpts from mission need statement for the reactor neutrino detector, http://science.energy.gov/~/media/hep/pdf/files/Project$%$20Status/Reactor-Neutrino-MNS-Short.pdf, 2011, (Office of Science).

[24] F. P. An et al., Phys. Rev. Lett. **108**, 171803 (2012).

[25] J. K. Ahn et al., Phys. Rev. Lett. **108**, 191802 (2012).

[26] F. Ardellier et al., Double chooz, a search for the neutrino mixing angle theta-13, http://arxiv.org/abs/hep-ex/0606025v4, 2006, (hep-ph).

[27] F. Mandl and G. Shaw, *Quantum Field Theory*, volume Revised Edition, John Wiley and Sons, 1993.

[28] S. Bilenky, C. Giunti, and W. Grimus, Prog.Part.Nucl.Phys. **43**, 1 (1999).

[29] R. Bertlmann and H. Pietschmann, Phys. Rev. D **15**, 683 (1977).

[30] J. Ellis, M. K. Gaillard, G. Girardi, and P. Sorba, Ann. Rev. Nucl. Part. Sci. **32**, 443 (1982).

[31] K. Zuber, *Nuetrino Physics*, Institute of Physics Publishing Bristol and Philadelphia, 2004.

[32] B. Kayser, Neutrino phenomenology, facts,and questions, http://vmsstreamer1.fnal.gov/VMS_Site_03/Lectures/NuSS/presentations/090708Kayser.pdf, 2009, (2009 Nuetrino Summer School).

[33] I. Schur, Amer. J. Math. **67**, 472 (1945).

[34] B. Zumino, J. Math. Phys **3**, 1055 (1962).

[35] S. A. Bludman, D. C. Kennedy, and P. G. Langacker, Phys. Rev. D **45**, 18101813 (1992).

[36] S. A. Bludman, D. Kennedy, and P. Langacker, Nuclear Physics B **374**, 373391 (1992).

[37] K. Kanaya, Prog. Theor Phys. **64**, 2279 (1980).

[38] J. Schechter and J. W. F. Valle, Phys. Rev. D **25**, 774 (1982).

[39] B. Kayser, Neutrino mass, mixing, and flavor change, http://arxiv.org/abs/0804.1497, 2008, (hep-ph).

[40] K. Nakamura et al., J. Phys. G: Nucl. Part. Phys. **37**, 075021 (2010).

[41] Y. Ashie et al., Phys. Rev. Lett. **93**, 101801 (2004).

[42] K. Collaboration, Phys. Rev. D **74**, 072003 (2006).

[43] P. Adamson et al., Phys. Rev. Lett. **106**, 181801 (2011).

[44] H. Murayama, Oscillation parameter plots, http://hitoshi.berkeley.edu/neutrino/, 2011, (PDG 2011 Web Update).

126

[45] J. N. Bachall, A. M. Serenell, and S. Basu, Astrophys. J. **621**, L85 (2005).

[46] S. Collaboration, Combined analysis of all three phases of solar neutrino data from the sudbury neutrino observatory, http://arxiv.org/abs/1109.0763, 2011, (hep-ph).

[47] S. Abe et al., Phys. Rev. Lett. **100**, 221803 (2008).

[48] K. Equchi, Phys. Rev. Lett. **90**, 021802 (2003).

[49] B. Aharmim et al., Phys. Rev. C **81**, 055504 (2010).

[50] B. Aharmim et al., Phys. Rev. Lett. **101**, 111301 (2008).

[51] M. Apollonio et al., Phys. Lett. B **466**, 415 (1999).

[52] S. Yamamoto et al., Phys. Rev. Lett. **96**, 181801 (2006).

[53] O. Meplan, *Technical Reports No. LPSC 0912 and No. IPNO-09-01*, Technical Reports, 2009.

[54] MURE, Mcnp utility for reactor evolution: Couples monte-carlo transport with fuel burnup calculations, http://www.oecd-nea.org/tools/abstract/detail/nea-1845, 2009, (NEA-1845 MURE).

[55] R. R. G. Marleau and A. Heber, *Technical Report No. IGE-157*, Technical Reports, 1994.

[56] T. A. Mueller et al., Phys. Rev. C **83**, 054615 (2011).

[57] V. Kopeilik, L. Mikaelyan, and V. Sinev, Phys. At. Nucl. **67**, 1892 (2004).

[58] P. Vogel and J. F. Beacom, Phys. Rev. D **60**, 053003 (1999).

[59] J. Allison et al., IEEE Trans. Ncul.Sci. **53**, 270 (2006).

[60] S. Agostinelli et al., Nucl. Instrum. Meth **A506**, 250 (2003).

[61] J. B. Birks, Proc. Phys. Soc. **A64 874**, 511 (1951).

[62] D. Shrestha and G. Horton-Simth, The "good enough" pmt pointing study, http://neutrino.phys.ksu.edu/~dchooz/private/pmtpointing/, 2007, (KSU).

[63] S. Wagner, Scintillator light yield from low energy electrons, http://www.dchooz.org/DocDB/0009/000925/001/SW-ScintLY.pdf, 2009, (Double Chooz Document).

[64] S. Wagner, Results of the low energy electron quenching measurements, http://www.dchooz.org/DocDB/cgi-bin/private/ShowDocument?docid=1436, 2010, (Double Chooz Document 1436).

[65] S. Wagner, Mc tuning of cerenkov light production, http://www.dchooz.org/DocDB/cgi-bin/private/ShowDocument?docid=4460, 2009, (Double Chooz Document 4460).

[66] A. Technologies, Cary eclipse fluorescence spectrophotometer, http://www.chem.agilent.com/en-US/products-services/Instruments-Systems/Molecular-Spectroscopy/Cary-Eclipse-Fluorescence-Spectrophotometer/Pages/default.aspx, 2012, (Agilent).

[67] T. Classen, Energy scale strategy, http://www.dchooz.org/DocDB/cgi-bin/private/ShowDocument?docid=1234, 2009, (Double Chooz Document 1234).

[68] A. Cabrera, Dc2ndpub energy scale, http://doublechooz.in2p3.fr/Private/Working_Groups/Analysis/DC2ndPub/escale.php, 2012, (Double Chooz Document).

[69] F. Beissel et al., Journal of Instrumentation **8**, T01003 (2013).

[70] A. Cabrera, Nucl. Instrum. Meth. Phys. Res., Sect. A **617**, 473 (2010).

[71] T. Akiri, *Mesure du paramètre de mélange leptonique θ_{13} auprès de l'expérience d'antineutrinos de réacteur Double Chooz*, PhD thesis, Paris-Diderot University-2013, 2010.

[72] D. Trigger, Dc2ndpub: Trigger: Threshold, efficiency, and associated systematics, http://doublechooz.in2p3.fr/Private/Working_Groups/Analysis/DC2ndPub/trigger.php, 2012, (Double Chooz).

[73] M. Ishitsuka et al., Trigger efficiency task force report, http://www.dchooz.org/DocDB/cgi-bin/private/ShowDocument, 2011, (Double Chooz Document 3261).

[74] P. Novella, Recopulse: Software and algorithms for pulse reconstruction, http://www.dchooz.org/DocDB/cgi-bin/private/ShowDocument, 2009, (Double Chooz Document 649).

[75] P. Novella, Recopulse configuration for data reprocessing, http://www.dchooz.org/DocDB/cgi-bin/private/ShowDocument?docid=2997, 2011, (Double Chooz Document 2997).

[76] S. Fernandes, Idli test bench light level measurements, http://www.dchooz.org/DocDB/cgi-bin/private/ShowDocument?docid=1652, 2010, (Double Chooz Document 1652).

[77] D. C. EU++, Eu++ results for second comparison stage, http://www.dchooz.org/DocDB/cgi-bin/private/ShowDocument, 2011, (Double Chooz Document 3199).

[78] H. D. Kerret, First results from the double chooz experiment, http://www.dchooz.org/DocDB/cgi-bin/public/ShowDocument?docid=3393, 2011, (LowNu11).

[79] Wikipedia, Californium, http://en.wikipedia.org/wiki/Californium#cite_note-NNDC2008-9, 2013, (Wikipedia).

[80] R. C. Martin et al., Production, distribution, and applications of californium-252 neutron sources, http://www.osti.gov/bridge/purl.cover.jsp?purl=/15053-AE6cnN/native/15053.pdf, 1999, (IRRMA'99).

[81] T. Mueller, Spill-in/out studies, http://www.dchooz.org/DocDB/cgi-bin/private/ShowDocument?docid=2864, 2011, (Double Chooz Document 2864).

[82] A. Hourlier et al., Neutron thermalization in the neutrino target, http://www.dchooz.org/DocDB/0041/004154/002/NeutronThermalization.pdf, 2012, (Double Chooz Document 4154).

[83] A. Hourlier et al., Neutron capture in the far detector, http://www.dchooz.org/DocDB/cgi-bin/private/ShowDocument?docid=4028, 2012, (Double Chooz Document 4028).

[84] A. Cucoanes, A toy model for the gamma spectrum generated in n-captures on gd, http://www.dchooz.org/DocDB/cgi-bin/private/ShowDocument?docid=3139, 2011, (Double Chooz Document 3139).

[85] T. Mueller, Spill-in/out studies and other interesting stuff about neutron physics, http://www.dchooz.org/DocDB/0030/003031/001/spill-in_ou_studies_th_mueller.pdf, 2011, (Double Chooz Document 3031).

[86] DC2ndPub, Dc2ndpub: Neutrino candidate selection, efficiencies, systematics, http://doublechooz.in2p3.fr/Private/Working_Groups/Analysis/DC2ndPub/neutrinos.php, 2012, (Double Chooz).

[87] T. Konno et al., J.Phys.: Conf. Ser. **331**, 022014 (2011).

[88] M. I. Products, 1-wire devices, http://www.maxim-ic.com/products/1-wire/, 2012.

[89] M. I. Products, Data sheet for ds9490, http://www.maxim-ic.com/datasheet/index.mvp/id/3834/ln/en, 2012.

[90] M. I. Products, Data sheet for ds18b20, http://datasheets.maximintegrated.com/en/ds/DS18B20.pdf, 2008.

[91] M. I. Products, Data sheet for ds2409, http://www.maxim-ic.com/datasheet/index.mvp/id/2909/ln/en, 2012.

[92] HSSEC, Three-axis magnetic sensor hybrid.

[93] HSSEC, Magnetic sensor hybrid application circuit.

[94] Wikipedia, Nuclear instrumentation module, http://en.wikipedia.org/wiki/Nuclear_Instrumentation_Module, 2013, (Wikipedia).

[95] C. Lane, Fe schematic, http://www.dchooz.org/DocDB/cgi-bin/private/ShowDocument?docid=980, 2009, (Double Chooz Document 980).

[96] M. I. Products, Data sheet for ibutton products, http://www.maxim-ic.com/products/ibutton/, 2012.

[97] G. Horton-Smith, Portion of 2007 slow monitoring" presentation relevant to thermal monitoring, http://www.dchooz.org/DocDB/0000/000040/, 2008, (Double Chooz Document 40).

[98] M. Forr, Phys. Rev. **72**, 868 (1942).

[99] P. H. Barrett, L. M. Bollinger, G. Cocconi, Y. Eisenberg, and K. Greisen, Rev. Mod. Phys. **24**, 133 (1952).

[100] M. Ambrosio et al., Astropart.Phys. **7**, 109 (1997).

[101] T. K. Gaisser et al., *Cosmic rays and particle physics*, Cambridge UK Univ. Pr., 1990.

[102] P. Adamson et al., Phys. Rev. D **76**, 052003 (2007).

[103] NASA, Temperature profile, `http://disc.sci.gsfc.nasa.gov/giovanni/additional/users-manual/DICCE_Help#K_profile`, 2012, (NASA).

[104] NASA, Additional information: Ascending and descending nodes, `http://disc.sci.gsfc.nasa.gov/giovanni/additional/users-manual/DICCE_Help#asc_desc`, 2012, (NASA).

[105] ECMWF, Era-interim, `http://www.ecmwf.int/products/data/archive/descriptions/ei/index.html`, 2012, (ECMWF).

[106] Wikipedia, European centre for medium-range weather forecasts, `http://en.wikipedia.org/wiki/European_Centre_for_Medium-Range_Weather_Forecasts`, 2012, (Wikipedia).

[107] M. Wurm, Muon id and tracking summary talk, `http://www.dchooz.org/DocDB/cgi-bin/private/ShowDocument?docid=3826`, 2012, (Double Chooz Document 3826).

[108] E. P. Caden, *Studying Neutrino Directionality with the Double Chooz Experiment*, PhD thesis, Drexel University-2013, 2013.

[109] FranceTopo, Francetopo.fr, `http://francetopo.fr/`, 2013, (FranceTopo).

[110] E. W. Grashorn, *Particle Astrophysics with the* MINOS *Far Detector*, PhD thesis, University of Minnesota FERMILAB-THESIS-2008-06, 2008.

[111] G. D. Barr, S. Robbins, T. K. Gaisser, and T. Stanev, Phys. Rev. D **74**, 094009 (2006).

[112] G. Bellini et al., Journal of Cosmology and Astroparticle Physics **05** (2012).

[113] R. Brun, Random numbers and histograms, `http://root.cern.ch/root/html/TH1.html`, 2012, (ROOT).

[114] N. Gagunashvili, PoS(ACAT) **54**, 0 (2007).

[115] P. Novella, Neutrino candidates blessed plots for dc2ndpub, `http://www.dchooz.org/DocDB/cgi-bin/private/ShowDocument?docid=4036`, 2012, (Double Chooz Document 4036).

[116] P. Novella, Neutrino candidates for dc2ndpub, `http://www.dchooz.org/DocDB/cgi-bin/private/ShowDocument?docid=4018`, 2012, (Double Chooz Document 4018).

[117] D. A. Background, Dc2ndpub: Accidentals selection cuts, rate and spectrum, `http://doublechooz.in2p3.fr/Private/Working_Groups/Analysis/DC2ndPub/accidentals.php`, 2012, (Double Chooz).

[118] K. Zbiri, Nucl.Instrum Meth A **597**, 219 (2008).

[119] D. Li9, Dc2ndpub: Lithium 9, `http://doublechooz.in2p3.fr/Private/Working_Groups/Analysis/DC2ndPub/lithium9.php`, 2012, (Double Chooz).

[120] M. Wurm, Cut parameters for the li-reduced free analyses, `http://www.dchooz.org/DocDB/cgi-bin/private/ShowDocument?docid=3883`, 2012, (Double Chooz Document 3883).

[121] D. C. Background, Dc2ndpub: Correlated background selection cuts, rate and spectrum, `http://doublechooz.in2p3.fr/Private/Working_Groups/Analysis/DC2ndPub/fastneutrons.php`, 2012, (Double Chooz).

[122] Wikipedia, Muon, `http://en.wikipedia.org/wiki/Muon`, 2013, (Wikipedia).

[123] DC2ndPub, Dc2ndpub oscillation fit, `http://doublechooz.in2p3.fr/Private/Working_Groups/Analysis/DC2ndPub/oscillationfit.php`, 2012, (Double Chooz).

[124] G.Feldman and R. Cousins, Phys. Rev. D **57**, 38733889 (1998).

[125] R. Carr, A. Franke, C. Mariani, M. Shaevitz, and M. Toups, Frequentist studies for dc2ndpub, http://www.dchooz.org/DocDB/cgi-bin/private/ShowDocument?docid=4058, 2012, (Double Chooz Document 4058).